Generalization of Mesoscale Lattice Boltzmann Methodology and Converging to Molecular/Continuum Level Phenomena

Submitted in partial fulfillment of the requirements for

the degree of

Doctor of Philosophy

in

Chemical Engineering

Sesha Hari Vemuri

M.S., Chemical Engineering, Carnegie Mellon University
B.S., Chemical Engineering, Vellore Institute of Technology

Carnegie Mellon University
Pittsburgh, PA

May, 2015

Abstract

The description of many technologies relies upon the development of an integrated, multiscale model, which can accurately describe physical phenomena over a broad range of time and length scales. Constructing such a multiscale model requires the establishment of individual models at each relevant scale followed by a holistic integration. In this dissertation, we develop a versatile mesoscale level model based on kinetic theory known as lattice Boltzmann methodology (LBM). The LBM scheme can be hybridized to link information simultaneously from the atomistic/molecular models, as well as the continuum models. This approach is an extension of the two popular models that link information at a broad range of time and length scales: "top (continuum) to bottom (atomistic)" scale used by process system engineers (without specific knowledge of the molecular architecture) or "bottom to top" scale used by scientists which is extremely time consuming for design purposes.

LBM captures the transport phenomena in fluids via the movement and interactions (collisions) of fluid molecules with themselves as well as the surroundings, which is very similar to the treatment of systems in molecular models. This methodology can lead to an efficient hybridization of atomistic/molecular information as well as describing continuum fluid flow as an alternative to CFD and ideally suited for incorporating molecular information

with computational efficiency and is extremely suitable for parallel computation. LBM can be used as an alternative simulation tool for continuum fluid dynamics compared to conventional CFD codes due to such advantages as use of simplistic rectilinear mesh and efficient transient calculations in a complex geometry, as well easily incorporating other physical phenomena. In addition, LBM can easily incorporate atomistic/molecular phenomena, which can be capitalized while developing a multiscale modeling tool. Thus, LBM can be considered as a mesoscale model and our approach for multiscale modeling in this thesis can extend towards the top scales by generating continuum results and utilizing molecular information in terms of the interaction forces & parameters in kinetic theory. This methodology can be termed as a middle-out approach to multiscale modeling.

To develop and validate this model, we utilize benchmark case study of the hydrogen fuel cells (HFCs), which are alternative power producing devices for stationary and automotive applications, with advantages of high efficiency, operation on renewable fuels with near-zero green house gas emissions. We begin by focusing on the development and validation of an LBM model for single phase flows in the entire range of Reynolds numbers. The designed LBM is tested with flows in and around microchannels with complex geometries, and our simulation results agree well with literature & CFD studies. LBM code not only can generate CFD results, but also one can re-formulate the physics of turbulence by our unique methodology of inverse approach, given the experimental data.

Once validated, we extended our LBM scheme by incorporating molecular/mesoscale interaction parameters in one of the most challenging components of HFCs to simulate: the porous gas diffusion layers (GDLs), which are critical in uniformly diffusing the reactant gases to the catalyst layers (CLs), and also managing the water vapor & liquid water content. The major bottleneck in durability of current HFC designs is the occurrence of multiphysical phenomena including phase changes of water in vapor and liquid states, which blocks the active reaction sites in the CL as well as decreasing the diffusion of reactant gases, thereby decreasing the overall performances. Continuum analysis of this type of behavior is not sufficient for modern design tools, as the inclusion of the complex microstructure and molecular architecture in the porous media increases the scale of computation time significantly for current methodologies. To resolve this issue, we take advantage of the highly efficient geometry handling techniques, and develop a non-isothermal multiphase LBM scheme descriptive for GDLs and describe how to incorporate molecular architecture as an input parameter. The GDL structure used in our simulation is reconstructed from micro/mesoscale x-ray tomography images via the use of stereolithography files. This approach to complex geometries provides a Boolean identifier tag to each point to separate points in both solid and fluid phases. The solid boundary conditions are straightforward extrapolations of the LBM distribution function values, which require less time to compute compared to partial differential equations.

We generalize the multiphase LBM based on the pseudo potential model, where the non-ideal behavior of fluids arising due the fluid-fluid interactions (occurring because of the difference in interaction strength between molecules in the liquid and the gas phase) is incorporated inside the lattice Boltzmann equation framework via an force term, which then links the multiphase LBM to a non-ideal equation of state (EOS), thereby preserving local thermodynamics consistencies. Depending on the sign and magnitude of the force, we can simulate miscible/immiscible phases for single/multi component systems. Solid-fluid interactions can also be incorporated via an adsorption like force term in mesoscale (which is directly based on the idea of molecular adsorption due to atomistic interactions between the fluid/solid) which depends on the number of nearest neighbor points belonging to the solid. Similar to the fluid-fluid force term, the sign and magnitude of the adsorption like force term can change the behavior of the solid between hydrophobic and hydrophilic. LBM treats macroscopic contact angle as mesoscale hydrophobicity/hydrophilicty interaction, where the parameter is from the bottom level molecular information. While developing the multiphase LBM schemes, in this work for the first time, we resolve the limitation of current LBM schemes of low density ratio between the heavier and lighter fluids of 100 inside the multiphase system. Existing commercial LBM codes such as XFlow and very recently multiphase LBM in COMSOL® microfluidics module primarily use Shan-Chen EOS, where the fluid compressibility values (slope of EOS curves) are much less than real world values. Our approach incorporates realistic EOS expressions and can extend to

high density ratios, which is a unique contribution in this thesis. We incorporate various types of cubic EOS including van der Waals, Redlich-Kwong, and Carnahan-Starling by generalizing the fluid-fluid/fluid-solid force terms while maintaining the stability of the simulation. This results in increase of the density ratio to around 2 000, and provides a physics based multiphase simulation methodology to understand the air/water or water vapor/liquid water systems inside HFCs. Our generalization of density ratio given in this thesis can illustrate the potential of LBM to be one of the most promising CFD tools since it incorporates local thermodynamic consistencies in transport phenomena.

We further investigate the effect of temperature changes inside the GDL and in HFC systems on the multiphase condensation and movement & behavior of liquid water. We provide a novel and easy methodology to "mimic" the temperature changes in porous media via temperature dependent fluid-fluid/fluid-solid interaction forces along the system. Our results of temperature mimicking induced condensation of water vapor to liquid water in a microchannel agree very well with phenomenological models and experimental data. For the first time, we were able to physically understand the thermoosmotic/thermocapillary phenomena that occurs in porous media: we found that depending on the hydrophilicity or hydrophobicity of the porous media, the flow of condensed water changes from hot to cold regions or cold to hot regions, respectively. This phenomenon has only been observed recently, and is not numerically resolved yet. We further developed a thermal LBM code and coupled this with the multiphase code mentioned earlier. Using Cahn-Hilliard theory, the additional

forcing term arising from the liquid water surface tension and its gradient depending on the calculated temperature at a local point is implemented. We perform a simple case study of liquid droplet movement on a microchannel substrate induced by temperature changes in the system. Finally, our generalized LBM scheme developed in this thesis becomes a timely one in CFD community since commercial software companies *i.e.*, COMSOL® are beginning to show great interest in LBM as an alternative tool for CFD calculations in microscale systems and also serves as a centerpiece to provide a future roadmap for hybridizing atomistic/molecular input (bottom level) and continuum (top level) to design complex systems via the middle-out approach. This holistic middle-out integration strategy can be more efficient than conventional bottom-to-top or top-to-bottom approaches. This point was addressed in HFC systems and can lead to development of similar middle-out methodologies to be applied in nanotechnology for sustainable systems, including water purification and nano/micro electromechanical systems.

Acknowledgements

I have been extremely fortunate to have worked with Professors Myung S. Jhon and Lorenz T. Biegler as my thesis advisors. I cannot thank them enough for their patience in guiding me from the beginning of my professional career. Their endless enthusiasm towards research, vast knowledge, and complementing expertise, especially for my project have truly made these past six years in graduate school a tremendously enjoyable learning experience for me. I will forever be grateful and looking up to you. Thank you bosses!

I would also like to thank my committee members Prof. Fred Higgs, Prof. Erik Ydstie, and Prof. Michael Domach for taking time off their busy schedules and providing me their valuable feedback and suggestions during the course of my thesis work. I am especially grateful for the generous financial support of my doctoral project provided by Seagate Technology, the Bettis Atomic Power Laboratory, and Hyundai Motors. I would also like to thank my past and present group members, especially Dr. Pil Seung Chung, Dr. Robert Smith, Dr. Dehee Kim, and Wonyup Song for their support and vigorous discussions on various research topics. Finally, I would also like to thank the staff of Chemical Engineering Department at Carnegie Mellon, especially Ms. Janet Latini and Ms. Cynthia Vicker for their support and assistance with a myriad things during the past six years. You made my life much easier at Carnegie Mellon! Thank you!

I cannot express enough my gratitude towards my parents, Prof. V.R.K. Murthy and Mrs. V. Lalitha, for their unconditional love, support, and sacrifices made to shape me as what I am. I will forever be in your debt.

Contents

List of Figures

List of Tables

Chapter 1

Overview

1.1 Introduction

Whether we explicitly recognize it or not, multiscale phenomena are part of our daily lives. For the simplest example, we organize our time in days, months, and years, as a result of the multiscale periodicity of the solar system. Many natural and man-made engineering devices in our society are organized in a hierarchical structure with various time and length scale phenomena in different sub-components in the systems. Such a structure has its origins in historical and evolutionary processes, and is also a reflection of the multiscale geographical structure of the earth, as modularizing various sub-components inside a given system makes it easier for the components to evolve freely, while maintaining the required connections with the rest of the system. Synergistic theory, modeling, and simulation methodologies can be extremely valuable tool to thoroughly understand these systems for (a) mimicking the process that go on in natural systems to man-made systems, and (b) to make man-made systems much more efficient via improved sub-component design criteria or introduction of novel materials. Intensive research efforts by scientists globally to realize the abovementioned two goals via developing individual models suitable to specific

scales have been going on for decades [1], however, their success has been limited mainly due to lack of available computational resources. However, significant advances in the computational power of various devices ranging from personal computers to large scale parallel computing clusters (shown in Fig. 1.1[1]) have taken place in the last decade.

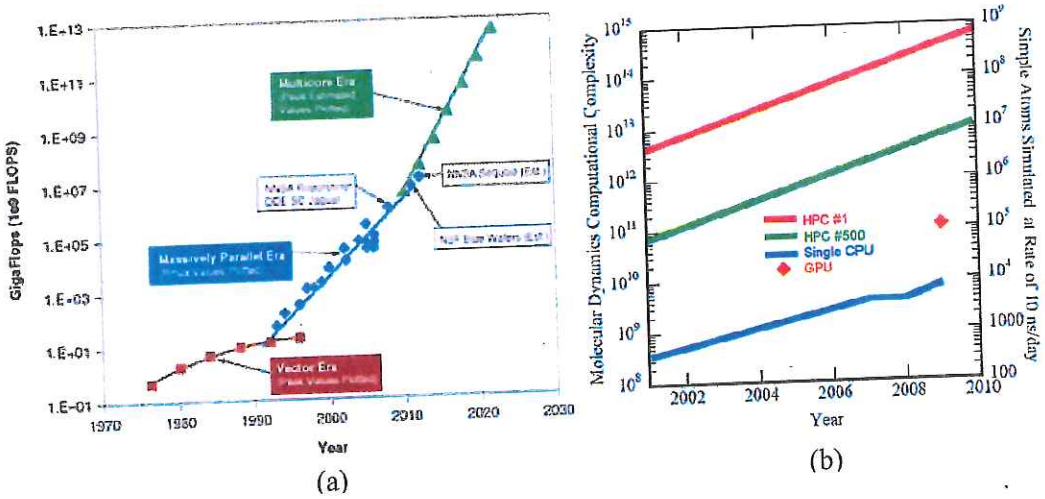

Fig. 1.1: (a) Improvements in computational capability in the past decade & into the future, (b) corresponding improvements in the computational complexity of molecular simulation methodologies [1]

Capitalizing on this opportunity of the millennium, the tools which numerically couple the fundamental phenomena based on first principles theories to the macroscale behavior of materials, known as **multiscale modeling**, have become the latest trend in computational science research. This new modeling framework spans multidisciplinary areas including physics, biology, chemistry, mathematics, statistics, engineering, and manufacturing.

A multiscale description generally has two primary components. The first is establishing models with varying degrees of resolution at each relevant time and length scale. The second component involves integrating each sub models so that information is seamlessly passed between individual scales as shown in Figure 1.2 with the goal of optimizing the overall system performance.

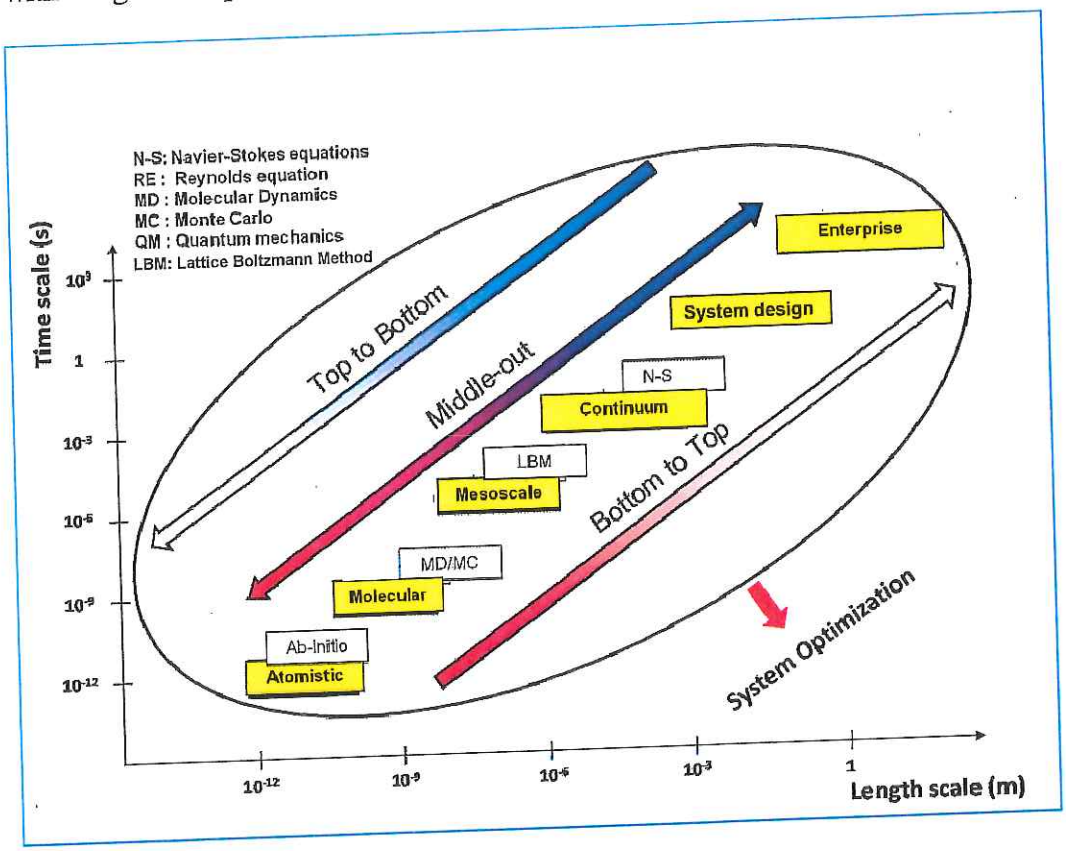

Fig. 1.2: An illustration of three different multiscale modeling methodologies.

The methodologies of achieving the two primary components vary depending on system design criteria required and the scientific approach to modeling. The most common approach for modeling engineering processes at the nanoscale is the "bottom-to-top approach", which relies on many microscale simulations coupled with each other to create a macroscale behavior of the larger system. However,

the problem of refining or coarse-graining the large degrees of freedom that exist at the microscale while maintaining the physical consistency make the application of the bottom-to-top multiscale models highly impractical and computationally intensive for engineering applications [2]. On the other hand, while top-to-bottom approaches eliminate the computational intensity of the bottom-to-top approach, they are very limited due to lack of proper hybridization of continuum theory with molecular information due to the large disparity in the time and length scales. This thesis incorporates these components and can resolve this critical issue in advanced modeling area by introducing a **novel middle-out approach** to multiscale modeling framework, which reduces the computational intensity due to seamless coupling of mesoscale/molecular & mesoscale/continuum scales, with minimal loss of any physical information.

This thesis introduces the development and establishment of a middle-out approach based on robust mesoscale methodologies originating from kinetic equations. The kinetic transport class of models describe the underlying movement of molecules or fundamental particles & their interactions (*i.e.*, collisions) and forces propagation resulting in the macroscopic phenomena. The various approaches include Fokker-Plank equation, Vlasov equation, and Boltzmann transport equation (BTE). The lattice Boltzmann method (LBM) is based on the BTE type of kinetic equation. Due to its particle description of physical phenomena, the discretized BTE, known as the LBM provides an extremely flexible and efficient basis on which the molecular transport processes and the macroscale behavior in complex system can be hybridized beyond the

capability of disparate, disconnected models [3]. In order to demonstrate our middle-out approach, we adopt benchmark case study in sustainable energy area, namely hydrogen fuel cells (HFCs), which are inherently multiscale in nature and reveal the capability of these approaches in making paradigm shifting impacts on the technological performance. We will focus on establishing multiscale models for systems which converge nanotechnology and molecular transport phenomena in complex structures which is the basis for the alternative and promising power generation systems based on electrochemistry, such as HFCs. These multiscale models are versatile enough to be extended to the engineering area of nanotribology, namely in nano/micro electromechanical systmes (N/MEMS). Sustainable energy/nanotribology are excellent examples of a technology which requires a range of model descriptions to achieve the desired performance.

In the following, we present a brief introduction to HFCs as a benchmark case study of developing and validating our middle-out multiscale methodology. We then present our research objectives, followed by an outline of the dissertation. We use engineering case studies of improving thin porous media catalyst layer performance in fuel cells and thin film lubricant performance in data storage systems in our approach.

1.2 Introduction to Hydrogen Fuel Cells

1.2.1 Hydrogen Fuel Cell

In the past decade, research and development activities for commercialization of fuel cell systems as a potential power source for stationary, portable and automotive systems have increased rapidly. Hydrogen fuel cells have especially

received attention owing to their higher power densities over the other types of fuel cells. Compared to conventional battery systems, the advantages of these systems are high operating efficiency, near-zero greenhouse emissions, operation on renewable fuels, reliable operation, and nearly instantaneous recharge capabilities.

An HFC comprises of anode and cathode regions, and a central electrolyte, which is a polymer membrane. A hydrogen fuel cell converts the chemical energy of the cell reaction shown in Fig. 1.3 to electrical energy. The basic mechanism of an hydrogen fuel cell can be explained as following: Humidified hydrogen is fed to the anode, which decomposes to protons and electrons. These protons are transferred from anode to the cathode via the polymer electrolyte membrane (PEM), and electrons via an external circuit. At the cathode protons and electrons react with feed O_2 to form water product.

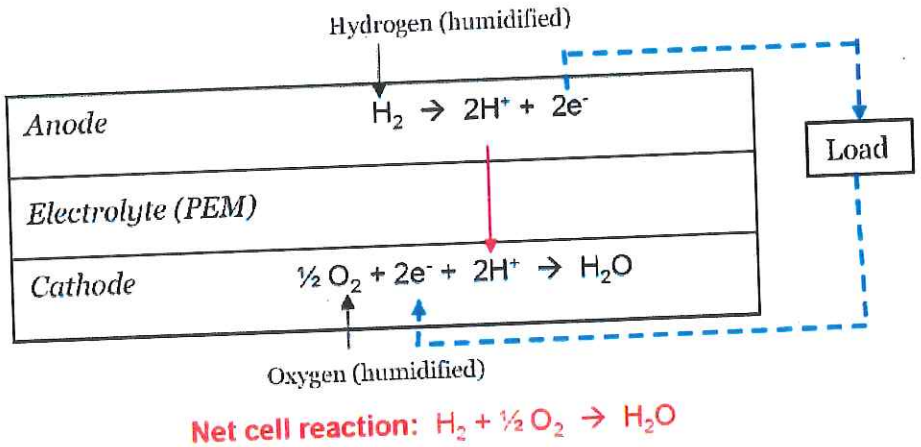

Fig. 1.3: Schematic of basic mechanism of an HFC

In more detail, a single fuel cell assembly comprises of seven key components: two gas channels (GCs), two gas diffusion layers (GDLs), two catalyst layers (CLs), and a PEM, as shown in Fig. 1.4. The GCs are graphite bi-polar plates, which comprise of open channels for inlet and outlet of reactants and products to get in the fuel cell, and escape, respectively. The GDLs are porous carbon paper or interwoven cloth materials. The function of GDLs is to uniformly distribute reactants from GC to the CL, support the CL materials, and act as a passage for water removal. The CL comprises of platinum (Pt) particles supported on carbon, where the electrochemical reactions occur. Finally, the PEM sub-component maintains the potential difference between the anode and cathode regions, as well as conducts protons from anode to cathode. This proton conduction process is critical to HFC performance as it may lead to significant ohmic losses in the cell.

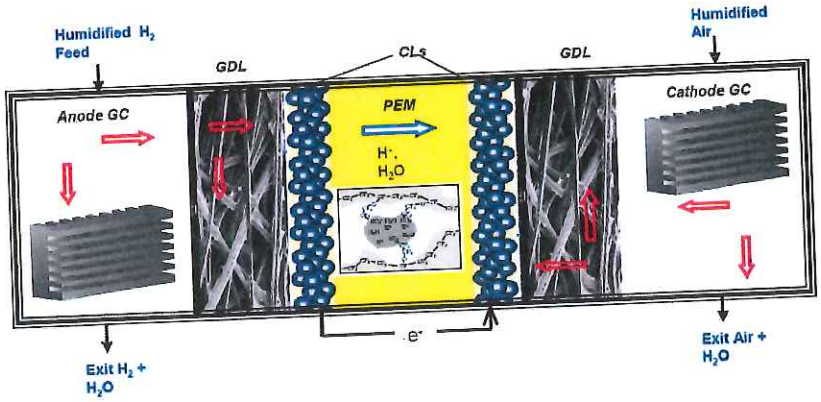

Fig. 1.4: A multi-component schematic of hydrogen fuel cells

1.3 Multiscale Modeling of Fuel Cells Case Study

The main requirement of a hydrogen fuel cell system model is the ability to simulate a wide variety of multiphase transport phenomena that occur in each of the abovementioned components. For example, in the GCs, single phase and multiphase fluid flow phenomena dominates in the anode and cathode side,

respectively. Currently, a traditional computational fluid dynamics (CFD) approach for solving Navier-Stokes equation is popular [4]. However, with the introduction of multiphase phenomena, the CFD models lose their accuracy and computational efficiency. Therefore, alternative simulation tools to CFD are also being used, such as lattice Boltzmann method [4]. The main issue in GC sub-components is to design the flow channels which maximize the cell performance. In the GDLs, One of the key issues with this sub-component is blockage of pores by water due to water vapor condensation, which leads to additional mass transfer resistances to the reactant gases, especially on the cathode side. The problem boils down to designing the GDL structures (porosity and hydrophobicity), which may be addressed via meso-scale descriptions of two phase flows within porous media. The goal in CL sub-component modeling is finding alternative catalyst materials, or CL structures, which lead to higher reaction kinetics, and are less expensive. This issue is being addressed by developing atomistic/molecular models [5]. The PEM model has to take into account the molecular interactions of the proton, water molecules, as well as the polymer molecules [6]. Thus, a multiscale modeling approach is a necessarily to holistically integrate the fuel cell components from all time and length scales and develop a thorough understanding & design criteria for novel material introduction for cheaper and more efficient catalyst films, an alternative PEMs or PEM structures.

1.4 Research Objectives

With the hydrogen fuel cells as the benchmark case study for sustainable energy systems, we aim to construct a novel middle-out model integration strategies based on mesoscale approach such as the LBM as the centerpiece by holistically integrating the following phenomena:

- Mesoscale/continuum based multiphase/multiphysical phenomena comprising mass, momentum & energy transfer, including electrochemical reaction phenomena.
- Multi-component systems, e.g., integrating GC, GDL, CL, and PEM sub-components in hydrogen fuel cells.
- Multiscale phenomena comprising the mesoscopic/continuum level descriptions with further coupling into the fundamental domains including atomistic/molecular level descriptions.

1.5 Outline of the Dissertation

The dissertation is organized into 6 Chapters

In Chapter 2, we introduce our approach to multiscale modeling in HFCs, which is the middle-out approach based on the mesoscale level particle based modeling methodology on Boltzmann transport equation, and its descritized form called lattice Boltzmann method (LBM). We explain the major models used in various time and length scales and in various HFC components. We illustrate the points in

which the atomistic/molecular models can be integrated to mesoscale/continuum models.

In Chapter 3, we provide a detailed introduction to our center piece LBM scheme, which can efficiently incorporate accurate microstructure and interactions as it looks at fluid flow as a set of pseudo particles moving and colliding, which result in rich multiphysical phenomena, and consequently are the most difficult to simulate. We compare LBM with the conventional field theory based approach where transport phenomena and the microstructure are averaged and there by resulting in loss of accuracy. The LBM is developed and validated over a range of examples, including the GCs of HFCs.

In Chapter 4, we further introduce the state-of-the-art multiphase simulation methodologies in LBM, and compare with CFD approaches and models. The extension from single phase to multiphase is straightforward in LBM, with the incorporation of a forcing term that imposes interactions of the pseudo particles to the system boundaries, thereby developing phase change. Firstly, previous efforts of multiphase LBM for low density ratios are introduced, and then our novel approach to improve the limitations is explained. This methodology is especially simulated for multiphase flow analysis in GDLs in fuel cells.

In chapter 5, we introduce our novel methodology to incorporate thermal models into multiphase LBM, done for the first time, to accurately investigate the atomistic/molecular interactions between multicomponents and multiphases inside complex porous structures of GDL in HFCs. Our efforts result in providing

further physical understanding into less known phenomena such as thermoosmotic/thermocapillary flows in microchannels inside porous media.

In chapter 6, we conclude the dissertation and summarize key contributions to the area of middle-out approach in multiscale modeling of nanoscale systems. We also provide a discussion of future directions and extensions to the middle-out model via hybridization of atomistic/molecular models in LBM, as well as incorporation of optimization tools. Further extension of the versatile multiscale models into multiple case studies including water purification technologies based on membrane distillation is also discussed.

Chapter 2

Multiscale Modeling via Middle Out Approach

2.1 Introduction

Multiscale modeling is being acknowledged in all basic and applied science & engineering. It is beyond coincidence that a search on the ISI Web of Knowledge® with the keywords *multiscale modeling* and *engineering* show higher and higher citations in the last five years, as shown in Fig. 2.1 [7].

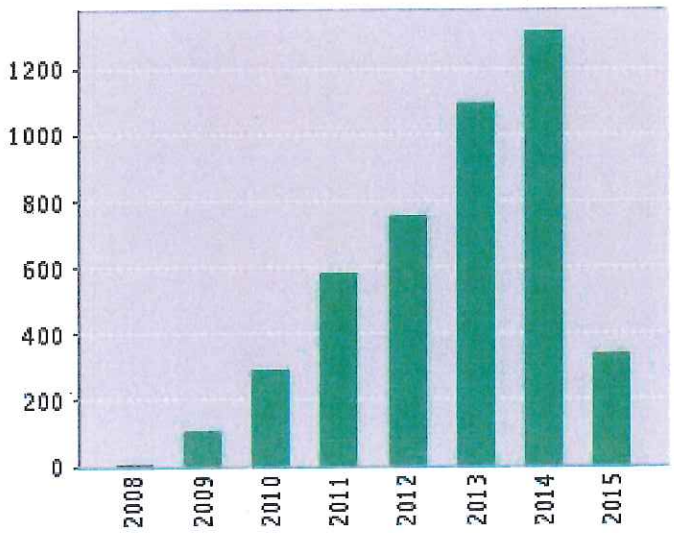

Figure 2.1: Number of citations per year in the ISI Web of Knowledge® with the keywords *multiscale modeling* and *engineering* [7]

In this Chapter, we describe the most promising methodology of developing multiscale modeling framework called *middle-out approach* in chemical engineering areas including alternative energy areas by specifically focusing on hydrogen fuel cells (HFCs) as case study (shown in Fig. 2.2).

This middle-out approach proposed by us selects the most versatile and efficient models based on the mesoscale time and length regimes as the center pieces and develop extended capabilities of atomistic/quantum/molecular and macro/system scales at the same time by marching in the directions, as shown in Fig. 2.2 [9]. This approach will save both time and effort tremendously.

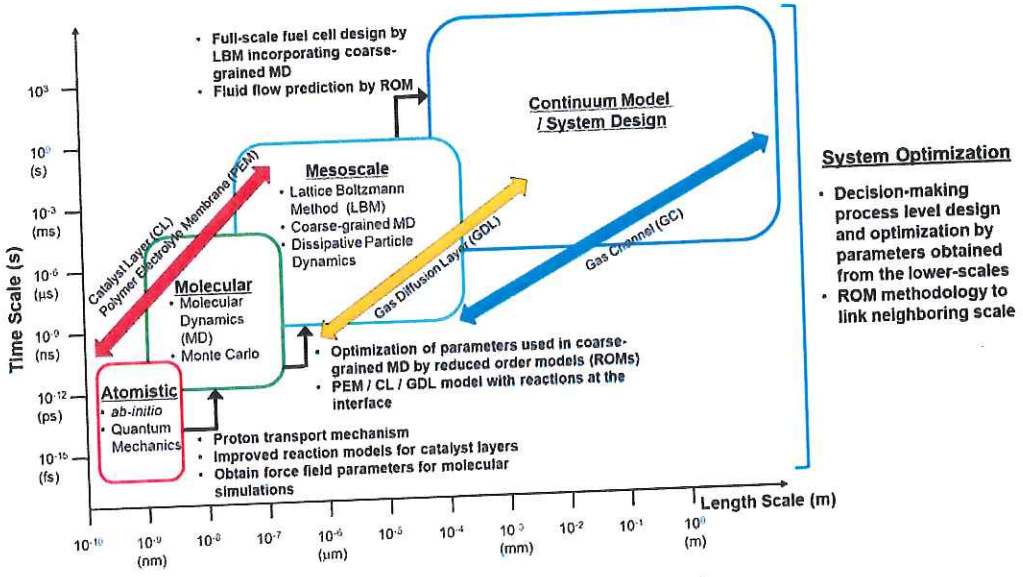

Fig. 2.2: Strategy and framework for middle-out multiscale approach on HFC model with system optimization [8]. Notations: MD: Molecular dynamics, ROM: Reduced order methods

The middle-out multiscale model can be differentiated into three important parts: (i) Macroscale models, (ii) Mesoscale/molecular models, and (iii) Atomistic models. We explain the models in detail and provide our overall approach to couple them in the following section.

2.2 Macroscale Models

A fundamental fuel cell model consists of five principles of conservation: mass, momentum, species, charge, and thermal energy. These transport equations are then coupled with electrochemical processes through source terms to describe reaction kinetics and electro-osmotic drag in the polymer electrolyte. Such convection-diffusion-source equations can be summarized in the following general form [9]

$$\frac{\partial(\rho\Gamma)}{\partial t}+\nabla\cdot(\rho\mathbf{v}\Gamma)=\nabla\cdot(\eta\nabla\Gamma)+\Delta p+S \tag{2.1}$$

Here Γ is a general macroscopic observable of interest, ρ the density, $\mathbf{v}$ the velocity vector, η the diffusion coefficient, p is the normal stress (pressure) and S a phenomenological source term. For example, the flow in GCs can be modeled as a microscale flow using the Eq. (2.1) to solve for velocity, *i.e.*, $\Gamma=\mathbf{v}$. In the diffusion and fluid flow for GDL & the electro-osmotic diffusion of protons through a PEM porous media and the porous electrodes of CLs, Darcy's drag exerted on gas flow is typically accounted for through a source term in the momentum equation. For diffusion, $\Gamma=c$, where c is the concentration of species i, and for fluid flow, $\Gamma=\mathbf{v}$. The source term is one of the most important

parameters that differentiates between the various transport phenomena, while also opening the door towards linkage of molecular/atomistic scale models with the macroscale model. For instance, S=force due to microscale interactions of multiphases (liquid water and water vapor) for GDL, S=consumption via reaction in CLs, and S=drag due to proton interaction with polymer backbones in PEM). More precisely, in the case of CLs, the source term S is linked to the electrochemical reactions that go on at the atomistic sites of the platinum reactive sites in catalyst clusters via [9-12]:

$$S_k = -\frac{s_k j}{nF}, \tag{2.2a}$$

$$\text{With } j = ai_0\left[\exp\left(\frac{\alpha_a F}{RT}\eta\right) - \exp\left(-\frac{\alpha_c F}{RT}\eta\right)\right] \tag{2.2b}$$

Here, s_k is the stoichiometric coefficient of reaction species, j is the volumetric transfer current of the reaction, a is the electrochemically active area per unit of electrode volume, i_o is the exchange current density, α_a and α_c are the anodic and cathodic transfer coefficients, respectively, F is Faraday's constant, R is the universal gas constant, and T is the cell temperature (in absolute scale). The Eqs. (2.2a) and (2.2b) denote a macroscopic approach for reaction rates without considering important parameters including catalyst microstructure, catalyst particle shape/size factor, as well as local catalyst loading changes. Thus, this approach is unable to model subtle changes in microstructure and nanoscale material synthesis parameters and the differences they bring to the macroscale behavior of HFCs [13-16]. Therefore, there is a great need for accurate values for

the source term, especially in GDLs and CLs requires accurate models in the meso/molecular scales as well as atomistic scales.

2.3 Mesoscale/Molecular Models

To capture the complex transport phenomena within nano/microstructural geometry, a recently developed methodology known as lattice Boltzmann method (LBM) was recently introduced as an alternative mesoscale/continuum level modeling tool [17-19], which is the heart of the thesis. LBM has the advantages in capturing clear physics in the system with complex geometry and nanoscale physics, and is the centerpiece of our multiscale modeling framework for HFCs. The basic premise of LBM is that it considers the anode and cathode reactant fluids, namely hydrogen and oxygen, as a set of particles (similar to molecules in atomistic modeling analogy) which collide amongst themselves and to the system boundaries, therefore bringing about the transport phenomena as a result. The movements of the particles (molecules) can be modeled as an evolution of probability distribution function f, which shows the probability of finding a particle of the fluid at a position **x** at time t, as shown below:

$$\frac{\partial f(\mathbf{x},\mathbf{v},t)}{\partial t}+\mathbf{v}\cdot\nabla f(\mathbf{x},\mathbf{v},t)=-\frac{1}{\tau}\left[f(\mathbf{x},\mathbf{v},t)-f^{eq}(\mathbf{x},\mathbf{v},T)\right]+\mathbf{F} \tag{2.3}$$

Here, feq is the equilibrium probability distribution of macroscopic observables (*e.g.*, velocity) in the system: given as a Maxwell-Boltzmann statistics expression, τ is the relaxation time parameter, *i.e.*, average timescales in between collisions of

particles (related to macroscale viscosity as: $\nu = \frac{\tau_h{}^{\alpha} - 1/2}{9}\Delta t$), $\mathbf{v}$ is the velocity of the particles, and $\mathbf{F}$ is the measure of interactions of the particles (molecules) among themselves as well as the system boundaries, and can be accurately modeled to the each point in the grid and its corresponding neighbors. A more detailed explanation would be given in Chapters 3 and 4. LBM covers a broad range of the system scale and is based on the particle assumption, the method is considered as a multi-scale method from mesoscale to continuum scale including buffer region simulation substituting conventional CFD.

2.4 Molecular Methods

The phenomena that arise at the micro/nanoscale interactions with the fluids with complex system boundaries including porous GDL fibers and CL electrodes can mainly be modeled via a molecular level approach. This methodology, known as the united atom molecular dynamics (MD) model simplifies the detailed atomistic structures of molecules (*e.g.*, polymer electrolyte membrane (PEM) in HFC) and surfaces by categorizing groups of atoms within uniform beads, as shown in Fig. 2.3 (a)-(e). These beads can move and interact via equations of motion in 3D expressed in the following Langevin equation form [20-22]:

$$m\frac{d^2\mathbf{r}_{\alpha i}}{dt^2} = -\frac{\partial U}{\partial \mathbf{r}_{\alpha i}} - \zeta \cdot \frac{d\mathbf{r}_{\alpha i}}{dt} + \mathbf{f}_{\alpha i}(t) \tag{2.4}$$

Here, i spans 1, 2, … N and α spans 1, 2, … N_p, where N and N_p imply the number of united atom sites and their constituent atoms respectively (as shown in Fig. 2.3 for polymer exchange membrane molecules), m is the mass of the united

atom sites, and U is the potential energy of the system. It is to be noted that at the molecular scale, we simulate the N particle united systems with complex molecular structures. This can be done by constructing united atomistic sites from all atom models via coarse-graining procedure.

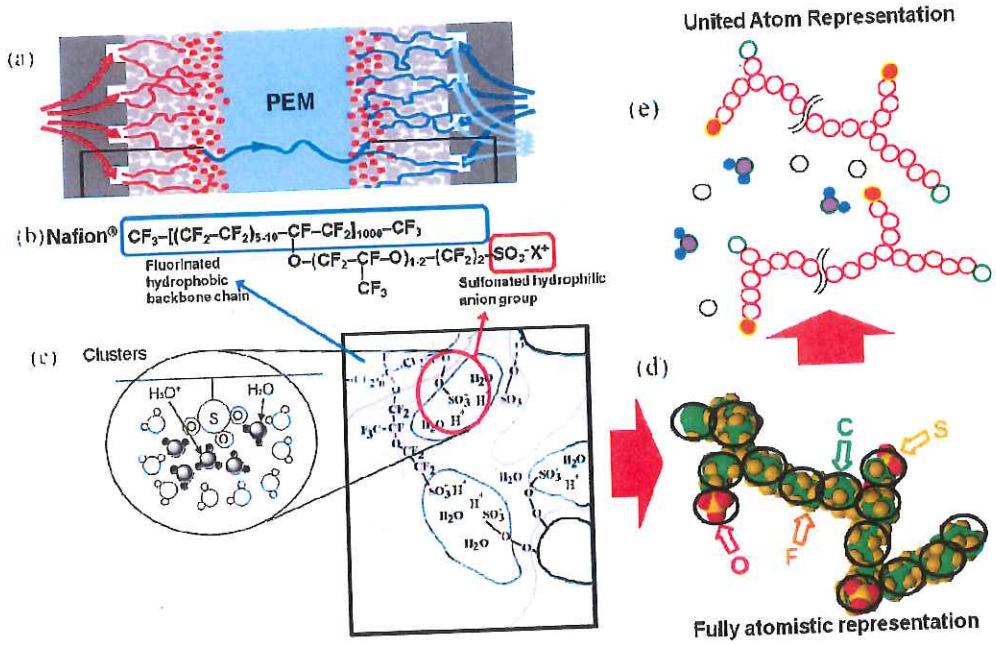

Fig. 2.3: Illustration molecular representation for PEM in HFC (a): PEM System in HFC, (b): Nafion® molecular structure of PEM, (c): atomistic/molecular interactions between Nafion® and water molecules, (d): fully atomistic representation of Nafion®, (e): united atom representation of Nafion® obtained via coarse-graining method and/or ROMs for efficient calculation of PEM properties

The interaction energy term (U), also known as potential, can be expressed as, for example, for a simple system as a truncated Lennard-Jones (LJ) expression:

$$U_{LJ1}(r) = \begin{cases} 4\varepsilon\left[\left(\frac{\sigma}{r}\right)^{12} - \left(\frac{\sigma}{r}\right)^{6}\right] & r \le 2.5\sigma \\ 0 & r \ge 2.5\sigma \end{cases} \qquad (2.5)$$

Here, r is the distance between beads, and ε represents the well depth of LJ interaction, and σ is the bead diameter. There are other empirical expressions of the potential depending on the phenomena to be recovered, as discussed in the reactive force field (ReaxFF), which simultaneously captures reactive and transport processes at the interface between PEM and electrode [23]. The basis of the potential expression forms and the parameters used in Eq. (2.5) is from the atomistic/quantum level models. These models offer the most physically detailed description necessary for linking material behavior (*e.g.*, individual water molecule interactions with GDL fibers and oxygen reduction reaction at CL) with molecular architecture. Figure 2.4 shows some of the potentials used in a united atom system.

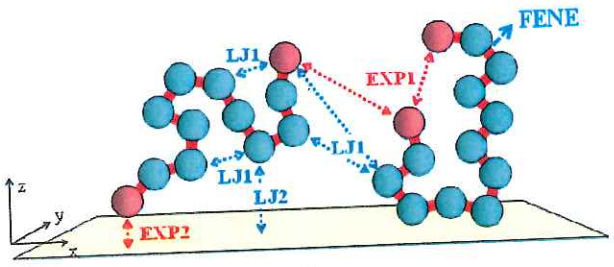

(a)

Backbone – Backbone	$U_b(r) = 4\varepsilon\left[\left(\frac{\sigma}{r}\right)^{12} - \left(\frac{\sigma}{r}\right)^{6}\right]$
Backbone – Surface	$U_w(z) = -\frac{c_w}{z^3}$
Endgroup – Endgroup	$U_t(r) = -\varepsilon_t \exp\left(-\frac{r - r_0}{d}\right)$
Endgroup – Surface	$U_{tw}(z) = -\varepsilon_{tw} \exp\left(-\frac{z - z_t}{d}\right)$
Adjacent bead connection	$U_{FENE}(r) = -\frac{1}{2}kR_0^2 \ln\left[1 - \left(\frac{r}{R_0}\right)^2\right]$

(b)

Fig. 2.4: (a) Various potentials used in the united atom model; (b) Corresponding expressions of the potentials. The blue and the red beads show the united atom sites as represented in Fig. 2.3 (e)

2.5 Atomistic/Quantum Models

Atomistic/quantum intramolecular/intermolecular energy studies are conducted in order to accurately account for the various changes in electrostatic, covalent and intermolecular bonds that occur at nano/pico scales when the individual reactant molecules (hydrogen & oxygen) come together at the PEM/CL/carbon substrate boundary and produce the water molecules. These models describe the conformational and energy changes in the individual molecules when interacting with a substrate, since the strength of the intermolecular interactions influences the dynamic behavior of the molecules, and thereby, the transport phenomena, *i.e.,* kinetics, multiphase flow. The energy changes with the intermolecular distances can then be transferred as potential expressions to be utilized in coarse grained MD calculations. The interaction energies can be distinguished into two categories: (i) intramolecular interaction energies and (ii) intermolecular interaction energies.

The intramolecular potential is related to the forces acting inside a given molecules (bond stretching, bending, and torsion) and is calculated using the method of Seminario [24] which derives the force constants from the *ab initio* Hessian tensor (**H**) via an eigenvalue analysis [25]. The Hessian is calculated via an atomistic/ ab initio energy study, and is the second-derivative tensor of the potential energy at the equilibrium geometry. From the Taylor series expansion of the potential:

$$U - U_0 = \nabla U \cdot d\mathbf{r} + \frac{1}{2}\mathbf{H} : d\mathbf{r}\, d\mathbf{r}, \tag{2.6}$$

$$\text{with } \mathbf{H} \equiv \nabla\nabla U, \tag{2.7}$$

assuming higher order terms to be negligible. The parameters for various potentials can be calculated via assuming a harmonic approximation to the bond stretching and angle bending potential energies:

$$U_r = \frac{1}{2}K_r(r - r_0)^2, \tag{2.8}$$

$$U_\theta = \frac{1}{2}K_\theta(\theta - \theta_0)^2, \tag{2.9}$$

where U_r & U_θ are the bond stretching and angle bending potential energies, respectively, and K_r & K_θ are the bond stretching and angle bending force constants, respectively. The equilibrium bond length and angle are given by r_o and θ_o, respectively. The torsional potential parameters, describing four bonded atoms, are calculated by generating the torsional energy profiles via a series of constrained geometry optimizations. The form of the torsional potential is:

$$U_\phi = \sum_{n=0}^{N-1} A_n \cos^n \phi, \tag{2.10}$$

where U_ϕ is the torsional potential, A_n are the torsional potential coefficients, N is the truncation order, and ϕ is the torsional angle. These potential energy forms are usually selected due to their widespread use in popular molecular dynamics codes.

The intermolecular energies are related to interactions between two molecules: of the same nature or different natures. The uncorrected interaction energy represented by the potential energy of the configuration is calculated as:

$$U_{int} = U_{(A-B)} - U_A - U_B \tag{2.11}$$

where U_{int} is the energy of the dimer and U_A and U_B are the energies of isolated monomers A and B, respectively and are calculated via atomistc/*ab initio* studies. The finite basis sets used in the calculations cause each monomer to share basis functions with other monomers in the dimer calculation, which is known as basis set superstition error (BSSE). As a consequence, the interaction energy is overestimated by Eq. (2.11). Thus, to reduce the BSSE associated with our computational techniques, a counterpoise correction (CP) [26] is utilized below for Eqns. (2.12) – (2.13):

$$U_{int}^{CP} = U_{int} + BSSE \tag{2.12}$$

$$BSSE = U_{(A\text{-}0)} - U_{(A\text{-}X)} + U_{(B\text{-}0)} - U_{(B\text{-}X)}, \tag{2.13}$$

where $U_{(A\text{-}0)}$ is the energy of monomer A at the dimer geometry, $U_{(A\text{-}X)}$ is the energy of monomer A at the dimer geometry with the added basis functions of monomer B, with an analogous treatment for monomer B.

2.6 Multiscale Integration

To complete the disparate models covering a broad range of time and length scales, the focus of multi-scale modeling strategy is on developing bridging methodology connecting quantum–atomistic/molecular–mesoscale–continuum

levels [27-40]. The bridging procedure finds reduced order parameters for upper level scale models. As shown in Fig. 2.3, ROMs are introduced to capture the predictive behavior of the lower-scale model and provide the links to capturing behavioral information from all of the lower scales, while allow the integrated formulation to be tractable.

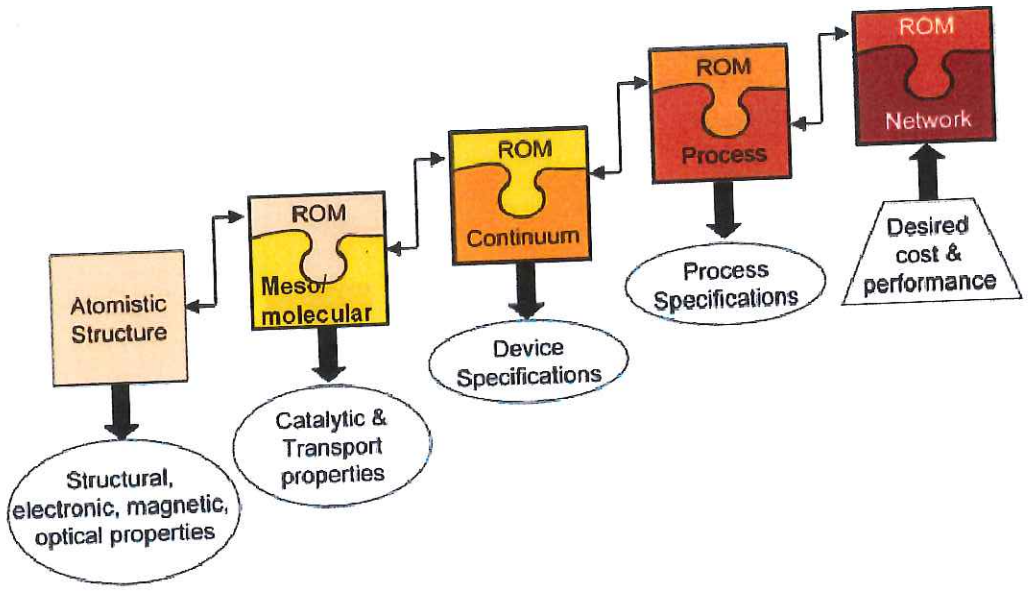

Figure 2.5: Linking models at various scales using ROMs and deriving lower-scale specifications through an inverse optimization formulation.

The major role of multi-scale ROMs is that they allow feasible realizations of complex domain models (consistency) and capture accurate complex model behavior over a wide range of the decision space (performance). One possible methodology of integrating the LBM (center piece of our multiscale model) and MD is given as follows [40]. At atomistic and molecular levels, the task is to infer thermodynamic and kinetic properties and constants that are later used in macroscopic physics-based models. Often these calculations are used directly to

regress to physics based ROMs, such as with cluster expansion and kinetic Monte Carlo modeling.

2.7 Summary

In Chapter 2, we develop a novel middle-out multiscale methodology in which a versatile centerpiece mesoscale level model based on kinetic theory is adopted as the foundation, where the model is hybridized to link information simultaneously from the atomistic/molecular models, as well as the continuum models. Our middle-out approach is favorable to the traditional "top (continuum) to bottom (atomistic)" scale used by process system engineers (without specific knowledge of the molecular architecture) or "bottom to top" scale used by scientists which is extremely time consuming for design purposes. This dissertation develops a highly computationally efficient mesoscale level methodology based on kinetic theory known as lattice Boltzmann method (LBM) as a critical component, which was developed in-house, and can link parameters from bottom as well as top levels. LBM assumes that the transport phenomena in fluids is due to the movement and interactions (collisions) of fluid molecules with themselves as well as the surroundings, which is very similar to the treatment of systems in molecular models, thus providing an efficient coupling. LBM also has an advantage of easily hybridizing with continuum models as an alternative to CFD and ideally suited for incorporating molecular information with computational efficiency and is extremely suitable for parallel computation. To develop and validate this model, we utilize benchmark case study of the hydrogen fuel cell (HFC).

Chapter 3

Lattice Boltzmann Method

3.1 Introduction

Lattice Boltzmann method (LBM) [41-46] is a promising alternative numerical scheme for simulating fluid flows containing complex physics phenomena. LBM, although a relatively young methodology, has already been playing a dominant role in computational fluid dynamics (CFD) community. There are several international conferences which promote LBM [47, 54] on a regular basis. Unlike the conventional numerical methods, this method is based on mesoscopic kinetic equations, *i.e.*, by constructing simple kinetic models, the essential physics can be incorporated at the microscopic level and the averaged properties obey the desired macroscopic behaviors. This simplified version enables us to avoid solving nonlinear, integrodifferential kinetic equations (*e.g.*, Boltzmann transport equation (BTE)) in the study of mesoscale physics. Compared with other continuum approaches, the LBM provides numerous advantages, including a clear physical picture, an inherently transient nature, easy implementation of complex

boundary conditions and physical phenomena, novel treatment of turbulence, and fully parallel algorithms.

The LBM scheme is historically originated from the lattice gas cellular automata (LGCA), utilizing discrete particle kinetics, a lattice, and discretization of time. The original concept of the LBM was steered to capture the merits of LGCA while removing unnecessary constraints and ensuing anomalies. In LBM, the collision operator in BTE is simplified via a discrete scattering form and the multiple-relaxation processes, which can be further simplified using a single relaxation time via the Bhatnagar-Gross-Krook (LBGK) scheme, which is state-of-the-art in its simplicity and effectiveness. The LBM further introduces more flexibility in the simulation by introducing multi-phenomena processes. That is, we could take into account the different time scales for mass, momenta, and energy transfer in contrast to the single relaxation time model used in LBGK. Although the LBM evolved initially from LGCA, it can also be derived directly from the BTE by discretizing velocities via an expansion in Mach number (*Ma*). This approach encapsulates the LBGK formalism within the "big box" of numerical analysis. Systematic analysis and the derivation of LBM schemes from continuum kinetic theory and extension to fluid systems with extreme complexity are worth pursuing.

3.2 Lattice Boltzmann Method

3.2.1 Boltzmann Transport Equation

LBM uses a mesoscopic representation of the fluid dynamics, which has the potential to simulate three dimensional (3D) transient flows in complex

geometries at a more detailed level than conventional grid based CFD approaches. It is noted that LBM is by no means limited to discretization of the isotropic BGK equation that reproduces Navier Stokes equations (N-S) in the continuum hydrodynamic limit [41, 42]. A number of other physical systems have been successfully examined via LBM formulations [45]. Therefore, our finding can also advance the understanding of other physical systems. Below, we outline the main ingredients of the LBM approach.

It is well known in non-equilibrium statistical mechanics that fluid systems can be represented by kinetic equations on the "mesoscopic" level. On this level, fluid properties can be represented by a one particle distribution function defined in a phase space, $f = f(\mathbf{x}, \mathbf{v}, t)$, where $\mathbf{x}$ is the space coordinates and $\mathbf{v}$ is the velocity coordinates. Typical hydrodynamic variables such as mass, momenta, and energy (temperature) are the first five moments of f, whose time derivative obeys the following integro-differential equation [48]:

$$\frac{\partial f(\mathbf{x},\mathbf{v},t)}{\partial t} + \mathbf{v} \cdot \frac{\partial}{\partial \mathbf{x}} f(\mathbf{x},\mathbf{v},t) = C\{f(\mathbf{x},\mathbf{v},t)\}. \tag{3.1}$$

Equation (3.1) is well-known kinetic equation. The terms on the left hand side of Eq. (3.1) are the streaming terms while the term on the right hand side is the collision term C, which acts to restore equilibrium within the system, representing interactions of particles at various positions and velocities. One of the simplest yet physically consistent forms for C is the BGK approximation [49], which is constructed according to the physically simplistic argument that no matter what

the collision details are, the distribution function approaches a well-defined local equilibrium given by $f^{(eq)}(\mathbf{x}, \mathbf{v}, t)$, via collisions [49]:

$$C\{f(\mathbf{x}, \mathbf{v}, t)\} = -\frac{1}{\lambda}[f(\mathbf{x}, \mathbf{v}, t) - f^{(eq)}(\mathbf{x}, \mathbf{v}, t)], \tag{3.2}$$

where the parameter λ represents a characteristic relaxation time to equilibrium via molecular collisions. The details on this type of collision kernel are carefully examined in Jhon *et al.* [50-53] The velocity space $\mathbf{v}$ can be discretized into a finite set of velocities $\{\mathbf{e}_i\}$ which preservs the conservation laws [54-58]. Then, Eq. (3.1) becomes

$$\frac{\partial f_i(\mathbf{x}, t)}{\partial t} + \mathbf{e}_i \cdot \frac{\partial}{\partial x} f_i(\mathbf{x}, t) = -\frac{1}{\lambda}[f_i(\mathbf{x}, t) - f_i^{(eq)}(\mathbf{x}, t)]. \tag{3.3}$$

Taking the stream velocity as $\mathbf{e}_i = \delta\mathbf{x}/\delta t$ and applying upwind differencing, Eq. (3.3) becomes

$$f_i(\mathbf{x} + \mathbf{e}_i\delta t, t + \delta t) - f_i(\mathbf{x}, t) = -\frac{\delta t}{\lambda}[f_i(\mathbf{x}, t) - f_i^{(eq)}(\mathbf{x}, t)] \tag{3.4a}$$

or

$$f_i(\mathbf{x} + \mathbf{e}_i\delta t, t + \delta t) - f_i(\mathbf{x}, t) = -\frac{1}{\tau}[f_i(\mathbf{x}, t) - f_i^{(eq)}(\mathbf{x}, t)], \tag{3.4b}$$

where $\tau = \lambda/\delta t$. By performing Chapman-Enskog multiscale expansion to Eqs. (3.4) and choosing the equilibrium distribution forms properly, it can be shown that the LBM approaches to the asymptotically correct hydrodynamic [41, 42, 59−61] and local thermo-hydrodynamic [62, 63] limits. Then, the parameter τ is given by

$$\tau = 0.5 + \nu/(c_s^2 \delta t), \tag{3.5}$$

where ν is the kinematic viscosity and c_s is the adiabatic speed of sound. Five moments derived from $f_i(\mathbf{x}, t)$ obey the continuum macroscopic limit, and are defined as:

$$\begin{aligned} \rho(\mathbf{x},t) &= \sum_i f_i(\mathbf{x},t), \\ \rho\mathbf{u}(\mathbf{x},t) &= \sum_i \mathbf{e}_i f_i(\mathbf{x},t), \text{ and} \\ \mathrm{DT}(\mathbf{x},t) &= \sum_i (\mathbf{e}_i - \mathbf{u})^2 f_i(\mathbf{x},t). \end{aligned} \tag{3.6}$$

Here, ρ, $\mathbf{u}$, and T are the lattice fluid density, velocities, and temperature (energy), respectively and D is the dimension of the discretized velocity space. It should be noted that these quantities are lattice quantities and are not at all equal to the physical space units. A normalization methodology for converting physical units into lattice units and vice-versa is discussed in the Appendix A.

3.2.2 Lattice Models for Lattice Boltzmann Equation

Several 2D lattice models for the lattice Boltzmann equation (LBE) had been examined. The D2Q7 and the D2Q9 lattices give similar results. The former needs less memory to store its states while the latter allows the use of a Cartesian grid which gives simpler data structure. For 3D simulations, the D3Q15 and the D3Q19 lattices are used. Since the D3Q15 lattice presents a checkerboard invariant, the fluid momentum may form unphysical regular pattern. Therefore,

we need the D3Q19 lattice when performing a 3D simulation. Figure 3.1 shows two lattices for 2D and 3D LBM schemes.

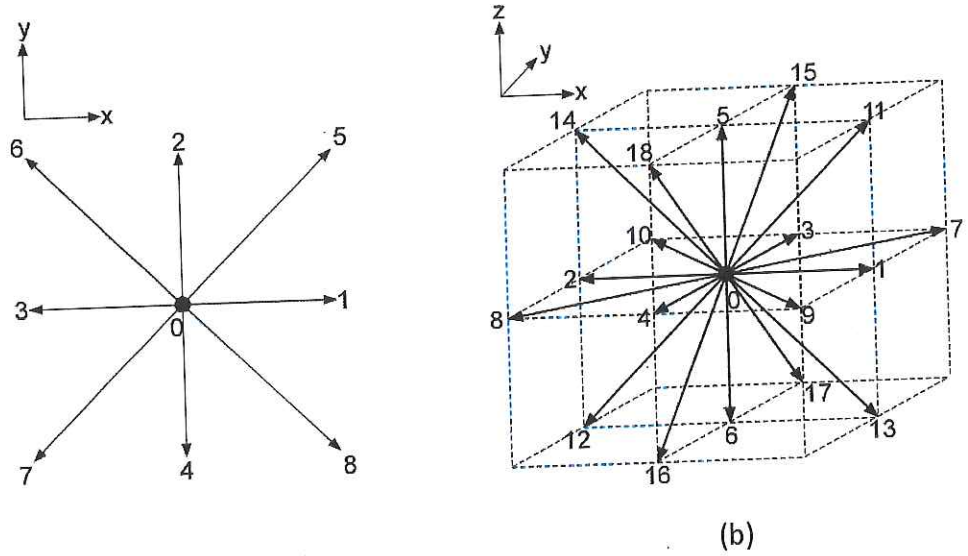

Fig. 3.1 (a) Lattices for D2Q9 and (b) lattices for D3Q19

3.2.3 Boundary Conditions

The dynamics of fluid flow is highly dependent on the surrounding environment. This influence is expressed mathematically via the prescription of boundary conditions, which play a critical role in CFD because they determine the solutions that are compatible with external constraints. The boundary conditions commonly used in LBM are periodic, no-slip, free-slip, and partial slip. For simple boundaries, these conditions can be dealt with by elementary mechanics argument alone.

Boundaries in LBM can be categorized with two classes: the open boundary and solid wall boundary. Most of the previous research efforts have focused on the

treatment of the solid wall boundary. In this report, we give a brief description on our development of solid wall boundary.

The bounce-back condition originated from lattice gas automata (LGA) has been extensively used in LBE simulation [64, 65]. The bounce-back scheme in the LBE method is intuitively derived from LGA. In this scheme, the particle hits the wall and bounces back opposite to its incoming direction. In LBE, the particle number is replaced with a real variable f_i. This scheme is very simple, efficient, and easy to implement. However, it is generally a first order treatment [65]. In simulating suspension flow, nonetheless, Ladd [66] placed the wall halfway between the nodes and made this treatment to be the second order accurate for the straight wall.

The bounce-back scheme has been modified to reduce the wall slip velocity by Nobel *et al.* [67] and Inamuro *et al.* [68], while Maier *et al.* [69] and Zou *et al.* [70] extended the bounce-back condition to non-equilibrium part of distribution function. To improve the numerical accuracy, Skordos [71] suggests adding a first order non-equilibrium distribution to the equilibrium distribution at wall nodes. Chen *et al.* [72] placed the wall at the node and used extrapolation to obtain f_i at boundaries. All the boundary treatments mentioned above model the curved wall as zig-zag steps, which results in geometric discontinuities and negatively affect the computational accuracy. This error is amplified as Reynolds number (*Re*) increases.

More sophisticated boundaries, which model a no-slip at the wall node with the second-order convergent error have been proposed by several investigators [67, 69, 73-75]. For practical purposes, the bounce-back rule is very attractive because it is a physically simple yet computationally efficient method to impose no-slip conditions in irregular geometries. An evaluation of the bounce-back method was performed for flow around octagonal and circular objects [76]. In these analyses, the location of the no-slip boundary was taken to be at the wall node itself and the error in the solution was found to be first-order convergent in space. The behavior of the bounce-back boundary for a staggered geometry was illustrated in Kandhai *et al.* [77] .

It has been observed that the error due to the staircase structure on the average is 50% larger than for flat geometries when compared to curved boundaries [77]. For a specific case (inclination angle of 45 degrees), it has been verified that the bounce-back rule tends to generate an imaginary boundary, which is located between the last fluid node and the solid wall. For the general case, it is expected that the exact location of boundary depends on the τ and the geometry of the system, and is difficult to predict the location of the no-slip wall for arbitrary geometries. For geometries with finite curvatures (*e.g.*, spherical particles), it has been found that the difference between the hydrodynamic radius and the geometric radius is quite small for $0.7<\tau<1.3$, and the particle radius is taken as half lattice spacing. A detailed comparison among the LBM simulation, the finite element method, and experimental data for fluid flow in a complex 3D chemical reactor has been recently reported [78]. The geometry of this reactor consisted of

a number of solid tubes in different orientations and locations to promote the mixing of fluid flow. The results of the LBM simulations were quite satisfactory even with moderate lattices. From these results, we conclude that despite its simplicity the bounce-back boundary is certainly very useful for irregular geometries. In some applications, however, sufficient accuracy may require refined lattices. In such cases, the accuracy can be increased by locally refining the grid in the vicinity of solid walls.

Filippova and Hanel (FH) [79, 80] presented a curved boundary condition using Taylor series expansion in both space and time for f_i near the wall. This boundary condition provides a second-order accurate treatment for a curved solid wall boundary. In addition, two other boundary treatments, investigated by Mei *et al.* [81] and Bouzidi *et al.* [82], have also been presented. The extrapolation scheme by Filippova and Hanel was improved by Mei *et al.* In the following, this scheme will be discussed in detail.

3.2.3.1 Extrapolation Scheme

This scheme is an elegant and simple method to handle boundary conditions in a systematic rather than a heuristic procedure. This method places the wall on boundary nodes and lets them undergo the same collisional step as the fluid nodes with the equilibrium population explicitly tuned to the desired wall speed. In other words, the wall serves only a portion of fluid with a prescribed equilibrium.

The LBGK model [53], given in Eqs. (3.1) & (3.2), consists of two computational steps:

Collision step : $\tilde{f}_i(\mathbf{x},t) - f_i(\mathbf{x},t) = -\frac{1}{\tau}\left[f_i(\mathbf{x},t) - f_i^{(eq)}(\mathbf{x},t)\right]$, and

Streaming step : $f_i(\mathbf{x}+\mathbf{e}_i\delta t, t+\delta t) = \tilde{f}_i(\mathbf{x}, t)$. (3.7)

Unlike solving the N-S equations for which the slip condition for $\mathbf{u}$ (fluid velocity) on a solid wall is satisfied at the macroscopic level, there is no direct, physically realistic boundary condition for f_i on a solid wall at the mesoscopic level. For a lattice node located on the fluid side at $\mathbf{x}_f$, as illustrated in Fig. 3.2, the streaming step clearly indicates a need for the information of $\tilde{f}_i$ at $\mathbf{x}_b$ on the solid side. Therefore, the boundary condition treatment is usually focused on the calculation of $\tilde{f}_i$ moving away from the wall into the fluid region. The most frequently used boundary condition is the so-called bounce-back scheme [64, 65, 63].

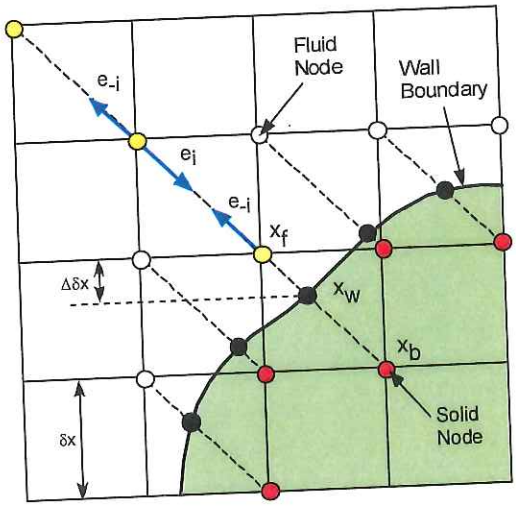

Fig. 3.2 Treatment of a curved boundary.

Here, the particle distribution f_i scatters back to the node $\mathbf{x}_f$ along the direction of $\mathbf{e}_{-i} = -\mathbf{e}_i$ as $\tilde{f}_i$ after a particle distribution f_i streams from a fluid node at $\mathbf{x}_f$ to a boundary node at $\mathbf{x}_b$ along the direction of $\mathbf{e}_i$. Since the wall position $\mathbf{x}_w$ is forced to be located at $\mathbf{x}_b$, this is referred to as bounce-back on the node (BBN) [84]. However, a finite slip velocity at the stationary wall exists [83, 85] and the accuracy for the flow field calculation is thus degraded due to the inaccurate description of the boundary condition [65]. In simulating suspension flows using the LBE, Ladd [66] placed the solid walls in the middle of the lattice nodes. This is referred to as bounce-back on the link (BBL). It has been shown that the BBL scheme gives a second-order accurate result for straight walls [70, 83].

Noble *et al.* [67] developed a second-order accurate boundary condition to compute $\tilde{f}_i$ but it is only applicable to the straight walls in a triangular lattice space. He *et al.* [83] generalized the scheme of Noble *et al.* [67] to arbitrary lattices. Chen *et al.* [72] placed the wall on the lattice node so that $\mathbf{x}_b$ is one lattice inside the wall. They used an extrapolation of f_i on the fluid side (including the wall node) to obtain f_i value at $\mathbf{x}_b$. Zou and He [70] proposed the BBL for the non-equilibrium part of f_i at the wall.

For a curved geometry, the use of BBL requires approximation of the curved boundary by a series of staircases. The geometric integrity cannot be preserved by such an approximation. For high Re flows the integrity of geometry is important since the vorticity generation and stress distributions are sensitive to the

geometrical resolution. To address this issue, He and Luo [86-88] proposed a nonuniform grid with second-order interpolations. He and Doolen [89] further applied the interpolation to the LBM with curvilinear coordinates or body-fitted coordinates. Mei and Shyy [90] solved the discretized BTE in curvilinear coordinates using the finite difference method. While the wall geometry is accurately preserved in body-fitted coordinates, the flexibility to handle complex geometries is maintained via the numerical grid generation techniques typically used in the N-S solvers. It should be noted that the most profound and rigorous theoretical treatment of the wall boundary condition is given by Ginzbourg and d'Humieres [91], which is local and accurate up to second-order in the Chapman–Enskog expansion. However, their scheme did not attract sufficient attention because its implementation is not as easy as the bounce-back scheme.

A robust, second-order accurate treatment for the distribution function f_i near a curved boundary is described based on the method recently proposed by Filippova and Hanel (FH [79, 80, 92]). Their boundary conditions for f_i on the solid side are evaluated via f_i on the fluid side, and the Taylor series expansions in both space and time for f_i near the wall. FH reported numerical results for a uniform flow over a cylinder [92]. However, it is found that there is a strong boundary condition-induced instability (for pressure-driven channel flow) when the distance from the wall to the first lattice on the fluid side is less than half of the lattice size. Using the Taylor series expansion for the velocity $\mathbf{u}$ near the wall, Mei *et al.* [81] proposed a new treatment for f_i near a curved wall. While maintaining a second-order accuracy of the solution in handling curved walls, the computational

stability is improved so that lower kinematic viscosity (or higher Re) can be successfully modeled in the LBM simulations. This boundary condition treatment is tested systematically to assess the temporal and spatial accuracy and robustness in 2D channel flow with constant and oscillating pressure gradients, flow due to an impulsively started wall, lid-driven square cavity flow, as well as flow over a column of circular cylinders. Detailed comparisons for the flow fields are made with either analytic solutions or numerical solutions of the N-S equations.

FH considered a curved boundary lying between the lattice nodes of spacing δx, as illustrated in Fig. 3.2, and briefly presented the derivation of their scheme for the treatment of a curved geometry. In Fig. 3.2, The lattice nodes on the solid and fluid side are denoted as $\mathbf{x}_b$ and $\mathbf{x}_f$, respectively. The filled small circles on the boundary, $\mathbf{x}_w$, denote the intersections of the wall with various lattice links. The boundary velocity at $\mathbf{x}_w$ is $\mathbf{u}_w \equiv \mathbf{u}(\mathbf{x}_w, t)$. The fraction of an intersected link in the fluid region, Δ, is,

$$\Delta = |\mathbf{x}_f - \mathbf{x}_w| / |\mathbf{x}_f - \mathbf{x}_b|. \tag{3.8}$$

Obviously, $0 \le \Delta \le 1$ and the horizontal or vertical distance between $\mathbf{x}_f$ and $\mathbf{x}_w$ is $\Delta\delta x$ $(<\delta x)$ on the square lattice. The particle velocity moving from $\mathbf{x}_f$ to $\mathbf{x}_b$ is taken as $\mathbf{e}_i$ and the reversed one from $\mathbf{x}_b$ to $\mathbf{x}_f$ is $\mathbf{e}_{-i} = -\mathbf{e}_i$. After the collision step, $\tilde{f}_i$ on the fluid side is known, but not on the solid side. Hereafter, we use $\mathbf{e}_{-i}$ and f_i^- to denote the velocity and the distribution function coming from a solid node to a fluid node. f_i^- is the unknown to be computed from

$$f_i^-(\mathbf{x}_f = \mathbf{x}_b + \mathbf{e}_{-i}\delta t, t+\delta t) = \tilde{f}_i^-(\mathbf{x}_b, t). \tag{3.9}$$

FH proposed the following linear interpolation,

$$\tilde{f}_i^-(\mathbf{x}_b, t) = (1-\chi)\tilde{f}_i(\mathbf{x}_f, t) + \chi f_i^{(*)}(\mathbf{x}_b, t) + 6t_i\rho/c^2(\mathbf{e}_{-i}\cdot\mathbf{u}_w), \tag{3.10}$$

where $\mathbf{u}_w$ is the lattice velocity at the wall and χ is the weighting factor (to be determined) that controls the linear interpolation (or extrapolation) between $\tilde{f}_i(\mathbf{x}_f, t)$ and a fictitious equilibrium distribution function $f_i^{(*)}(\mathbf{x}_b, t)$ given by

$$f_i^{(*)}(\mathbf{x}_b, t) = w_i\rho(\mathbf{x}_f, t)\left[1 + \frac{3(\mathbf{e}_i\cdot\mathbf{u}_{bf})}{c^2} + \frac{9(\mathbf{e}_i\cdot\mathbf{u}_f)^2}{2c^4} - \frac{3(\mathbf{u}_f\cdot\mathbf{u}_f)}{2c^2}\right]. \tag{3.11}$$

Here, $\mathbf{u}_f \equiv \mathbf{u}(\mathbf{x}_f, t)$ is the lattice fluid velocity near the wall and $\mathbf{u}_{bf}$ has to be selected. It is emphasized that χ depends on the choice of $\mathbf{u}_{bf}$, which is not unique. For example, either $\mathbf{u}_{bf} = \mathbf{u}_f$ or a linear extrapolation using $\mathbf{u}_{bf} = (1-\Delta^{-1})\mathbf{u}_f + \Delta^{-1}\mathbf{u}_w$ appears to be a reasonable choice.

To determine χ in Eq. (3.10), FH considered flows under the condition $L/(cT^*) << 1$, *i.e.*, the flow has an intrinsic characteristic time T^* that is much larger than the convection time scale, L/c. This "slow-flow" condition enabled FH to approximate $f_i^-(\mathbf{x}_f, t+\delta t)$ as

$$f_i^-(\mathbf{x}_f = \mathbf{x}_b + \mathbf{e}_{-i}\delta t, t+\delta t) = f_i^-(\mathbf{x}_f, t) + \delta t\frac{\partial f_i^-}{\partial t} + \cdots. \tag{3.12}$$

From the order-of-magnitude analysis, we obtain

$$f_i^-(\mathbf{x}_f, t+\delta t) = f_i^-(\mathbf{x}_f, t)\left[1+O\left(\frac{\delta t}{T}\right)\right] \\ = f_i^-(\mathbf{x}_f, t)\left[1+O\left(\frac{\delta x}{L}\frac{L}{cT}\right)\right] \approx f_i^-(x_f, t) \tag{3.13}$$

Here, we assumed $O(\partial f_i^-/\partial t) = O(f_i^-/T^*)$, and neglected terms of the order of $O\left(\frac{\delta x}{L}\frac{L}{cT^*}\right)$ for $L << cT^*$.

Further, applying the Chapman–Enskog expansion and invoking the "slow-flow" approximation, we obtain

$$f_i^-(\mathbf{x}_f, t) = f_i^{-(eq)}(\mathbf{x}_f, t) - \lambda\left[\frac{\partial f_i^{-(eq)}}{\partial t} + \mathbf{e}_{-i}\cdot\nabla f_i^{-(eq)}\right] + \cdots \\ \approx f_i^{-(eq)}(\mathbf{x}_f, t) - \lambda\mathbf{e}_{-i}\cdot\nabla f_i^{-(eq)} + \cdots. \tag{3.14}$$

The leading order term in $\nabla f_i^{-(eq)}$ is given as $\rho t_i(3/c^2)\mathbf{e}_{-i}\cdot\nabla\mathbf{u}$, since the rest are higher order terms in the incompressible flow limit. Noticing that $\lambda = \tau\delta t$, Eq. (3.14) becomes

$$f_i^-(\mathbf{x}_f, t) \approx f_i^{-(eq)}(\mathbf{x}_f, t) - 3\tau\delta t\rho t_i / c^2\mathbf{e}_{-i}\cdot\nabla\mathbf{u}\cdot\mathbf{e}_{-i} \\ = f_i^{(eq)}(\mathbf{x}_f, t) - 6\rho t_i / c^2\mathbf{u}_f\cdot\mathbf{e}_i - 3\tau\delta t\rho t_i / c^2\mathbf{e}_i\cdot\nabla\mathbf{u}\cdot\mathbf{e}_i, \tag{3.15}$$

which is approximation of the LHS of Eq. (3.9). We will expand the RHS of Eq. (3.9) for $\frac{\delta x}{L} = \frac{c\delta t}{L} << 1$. Notice that $f_i^{(*)}(\mathbf{x}_b, t)$ in Eq. (3.11) can be expressed as

$$f_i^{(*)}(\mathbf{x}_b, t) = f_i^{(eq)}(\mathbf{x}_f, t) + 3t_i\rho / c^2\mathbf{e}_i\cdot(\mathbf{u}_{bf} - \mathbf{u}_f), \tag{3.16}$$

so that the RHS of Eqs. (3.9) or Eq. (3.10), can be rewritten as

$$\tilde{f}_i^-(\mathbf{x}_b, t) \approx f_i^{(eq)}(\mathbf{x}_f, t) + (1-\chi)(1-1/\tau)f_i^{(1)}(\mathbf{x}_f, t) + 3w_i\rho/c^2\mathbf{e}_i\cdot(\chi\mathbf{u}_{bf} - \chi\mathbf{u}_f - 2\mathbf{u}) \\ = f_i^{(eq)}(\mathbf{x}_f, t) - 3(1-\chi)(\tau-1)\delta t_i\rho/c^2\mathbf{e}_i\cdot\nabla\mathbf{u}\cdot\mathbf{e}_i + 3w_i\rho/c^2\mathbf{e}_i\cdot(\chi\mathbf{u}_{bf} - \chi\mathbf{u}_f - 2\mathbf{u}_w). \tag{3.17}$$

Based on linear interpolation for $\mathbf{u}_{bf}$ and by noticing that $\mathbf{x}_b - \mathbf{x}_f = \delta x \mathbf{e}_i$, we obtain $\mathbf{u}_{bf} - \mathbf{u}_f \approx \delta \nabla \mathbf{u} \cdot \mathbf{e}_i$. From Eqs. (3.15) and (3.17) and matching terms linear in δ gives $\chi = (2\Delta - 1)/\tau$. For $\mathbf{u}_{bf} = \mathbf{u}_f$, we obtain $\chi = (2\Delta - 1)/(\tau - 1)$ by matching to $O(\delta)$ in Eqs. (3.15) and (3.17). FH found that $\mathbf{u}_{bf}$ gives computationally stable results only for $\Delta > 1/2$. Hence, they proposed that

$$\mathbf{u}_{bf} = (1 - \Delta^{-1})\mathbf{u}_f + \Delta^{-1}\mathbf{u}_w \;\&\; \chi = (2\Delta - 1)/\tau \text{ for } \Delta \geq 1/2, \tag{3.18a}$$

and

$$\mathbf{u}_{bf} = \mathbf{u}_f \;\&\; \chi = (2\Delta - 1)/(\tau - 1) \text{ for } \Delta < 1/2. \tag{3.18b}$$

To recapitulate, there are three independent assumptions that have been made in the foregoing derivation. These are: (i) the Chapman–Enskog expansion is valid [81]; (ii) the intrinsic time of the unsteady flow must be large compared to the convection time on the lattice scale, and (iii) the lattice space must be small compared to the characteristic length scale of the flow so that the Taylor series expansion for the velocity field near the wall is valid. There have been numerous studies regarding the validity and usefulness of Chapman–Enskog expansion for the solution of the BTE. The "slow-flow" condition is introduced to simplify the derivation of the boundary condition for f_i. The third assumption is a typical computational resolution requirement.

Mei *et al.* [81] realized that the flexibility in the construction of $f_i^{(*)}(\mathbf{x}_b, t)$ is the key to achieving an improved computational stability as well as accuracy. Since $\chi = (2\Delta - 1)/(\tau - 1)$ given in Eq. (3.18b) leads to a larger value of χ when τ is

close to 1, it is desirable to reduce the magnitude of χ by increasing the magnitude of the denominator in the expression for χ. For $\Delta \geq 1/2$, $\mathbf{u}_{bf}$ was chosen by FH to be u_f which is the fluid velocity at x_f and it leads to $(\tau - 1)$ in the denominator for χ. Thus, they proposed to use Eq. (3.18a) for $\Delta \geq 1/2$ and use $\mathbf{u}_{bf} = \mathbf{u}_{ff} = \mathbf{u}_f(\mathbf{x}_f + \mathbf{e}_{-i}\delta t, t)$ for $\Delta < 1/2$, then χ is expressed as $\chi = (2\Delta - 1)/(\tau - 2)$. This modification improved the computational stability of FH's method.

3.2.4 General Geometry Treatment

To take advantage of the complex geometry handling capability of the LBM, the grid points inside solid bodies should be decided. Deciding whether a point is in a solid or not is a basic test in a great number of computer graphics applications. Usually inclusion test algorithms are based on the resolution of the equation system or use of trigonometric functions [93], and most of them deal with a large number of singularities [94]. This leads to robustness problems, apart from inefficiency.

The 2D inclusion algorithm has already been widely studied [93], but the solutions offered in 3D are more complicated. Lane *et al.* [95] proposed a solution based on the use of trigonometric functions. More recently, Horn and Taylor gave a solution based on the computation of the distance between a point and every component of the solid [96].

Feito *et al.* [97] and Feito [98] (hereafter, named as Feito's algorithm) have presented an algorithm to test the inclusion of a point in a 2D polygon and their

work was extended to the 3D case [99]. Their algorithm was proven to be very efficient over other models proposed previously. Here, we summarized the algorithm for 2D and 3D cases for the complex boundary treatment of our LBM tool by introducing the fundamental definitions and describing the implementation of 2D and 3D algorithms.

3.2.4.1 CAD STL Format

A StereoLithography (STL) file is a triangular representation of a 3D surface geometry. The surface is tessellated or broken down logically into a series of small triangles (facets). Each facet is described by a perpendicular direction and three points representing the vertices (corners) of the triangle. For 3D surfaces, this format is very suitable for Feito's algorithm.

A STL file consists of a list of facet data. Each facet is uniquely identified by a unit normal (a line perpendicular to the triangle and with a length of 1.0) and by three vertices (corners). The normal and each vertex are specified by three coordinates each, so there are a total of 12 numbers stored for each facet. The facets define the surface of a 3D object. As such, each facet is part of the boundary between the interior and the exterior of the object. The orientation of the facets (which direction is "out" and which direction is "in") is specified redundantly in two ways which must be consistent. First, the direction of the normal is outward. Second, the vertices are listed in counterclockwise order when looking at the object from the outside (right-hand rule). These rules are illustrated

in Fig. 3.3. Each triangle must share two vertices with each of its adjacent triangles. In other words, a vertex of one triangle cannot lie on the side of the other. This is illustrated in Fig. 3.4.

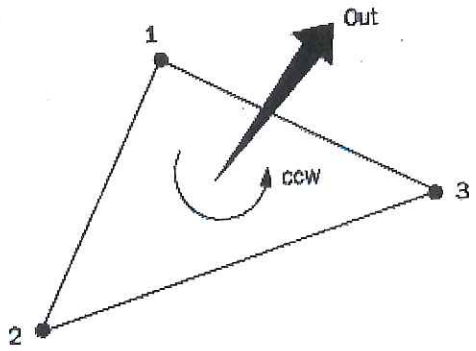

Fig. 3.3 Orientation of a facet is determined by the normal direction and the order in which the vertices are listed.

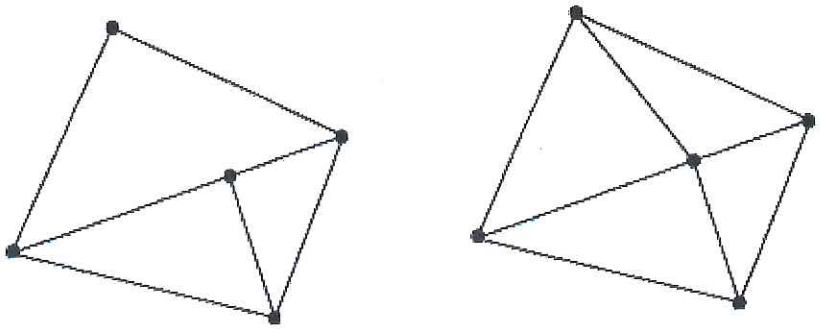

Fig. 3.4 The vertex-to-vertex rule. The left shows a violation of the rule. A correct configuration is shown on the right.

The object represented must be located in the all-positive octant. In other words, all vertex coordinates must be positive-definite (nonnegative and nonzero)

numbers. The STL file does not contain any scale information; the coordinates are in arbitrary units.

The conventional 3D Systems STL specification document states that there is a provision for inclusion of "special attributes for building parameters," but does not give the format for including such attributes. Also, the document specifies data for the "minimum length of triangle side" and "maximum triangle size," but these numbers are dubious in meaning. Sorting the triangles in ascending z-values is recommended, but not required.

The STL standard includes two data formats, ASCII and binary. These are described separately below. The ASCII format is primarily intended for testing new CAD interfaces. The large size of its files makes it impractical for general use. The syntax for an ASCII STL file is as follows:

solid name

$$\left\{\begin{array}{l} \text{facet normal } n_i\ n_j\ n_k \\ \quad \text{outer loop} \\ \quad\quad \text{vertex } v1_x\ v1_y\ v1_z \\ \quad\quad \text{vertex } v2_x\ v2_y\ v2_z \\ \quad\quad \text{vertex } v3_x\ v3_y\ v3_z \\ \quad \text{endloop} \\ \quad \text{endfacet} \end{array}\right\}^{+}$$

endsolid name

Non-italic word indicates a keyword; these must appear in lower case. Note that there is a space in "facet normal" and in "outer loop," while there is no space in any of the keywords beginning with "end." Indentation must be with spaces; tabs are not allowed. The notation, "$\{\ldots\}^{+}$," means that the contents of the brace

brackets can be repeated one or more times. Symbols in italics are variables which are to be replaced with user-specified values. The numerical data in the facet normal and vertex lines are single precision floats, for example, 1.23456E+789. A facet normal coordinate may have a leading minus sign, however a vertex coordinate may not.

The binary format uses the IEEE integer and floating point numerical representation. The syntax for a binary STL file is as follows:

Bytes	Data type	Description	
80	ASCII	Header. No data significance.	
4	unsigned long integer	Number of facets in file	
4	float	*i* for normal	+
4	float	*j*	
4	float	*k*	
4	float	*x* for vertex 1	
4	float	*y*	
4	float	*z*	
4	float	*x* for vertex 2	
4	float	*y*	
4	float	*z*	
4	float	*x* for vertex 3	
4	float	*y*	
4	float	*z*	
4	float		
2	unsigned integer	Attribute byte count	

The attribute syntax is not documented in the formal specification. It is specified that the attribute byte count should be set to zero.

3.2.4.1.1 Implementation of Feito's Algorithm

Feito's inclusion test algorithm of a point is implemented to simple and complex 2D and 3D geometries. For 2D case a closed loop comprising of surface points is given as input data. Figure 3.5 shows a complex obstacle which has several convex and concave corners. Hereafter, the word "hole point" is used to denote

the point that is inside a solid body and excluded for flow computation. In Fig. 3.5, the hole points are decided well by the Feito's algorithm and they are shown as blue open circles.

For the 3D case unstructured triangular surface grids are used to define the solid surface. Therefore, the Feito's algorithm can be applied to any type of 3D complex geometries flexibly because the unstructured surface grids can be generated more easily than the structured grids. Generally, CAD surface data can be exported in the STL format. Thus it is possible to generate field grid points from the primitive CAD data directly and make connection between the hole points and the fluid points automatically. In reality, the load to generate grid points for flow computation reaches up to 70~80% of the total work hours. Systematic and automatic grid generation and boundary treatment for general geometrical shape is the essence of LBM simulation. In this context, the implementation of the Feito's algorithm to the LBM simulation can be considered as a very efficient approach.

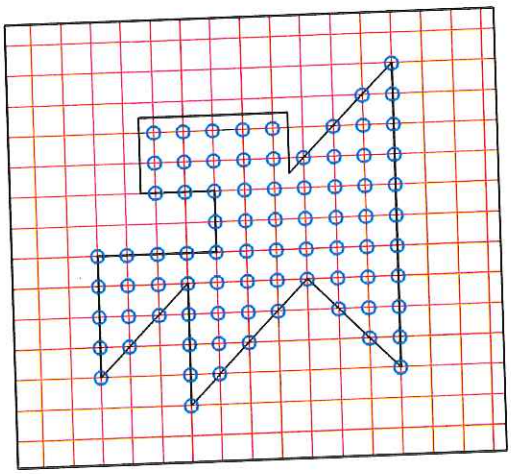

Fig. 3.5 Inclusion test for a point in a polygon using Feito's algorithm. Closed loop of solid line: an obstacle, blue open circle: hole points in a polygon.

Several types of geometries are used to validate the Feito's algorithm. Figure 3.6 shows a sphere with surface points defined by triangular facets. The hole points are decided by the Feito's algorithm.

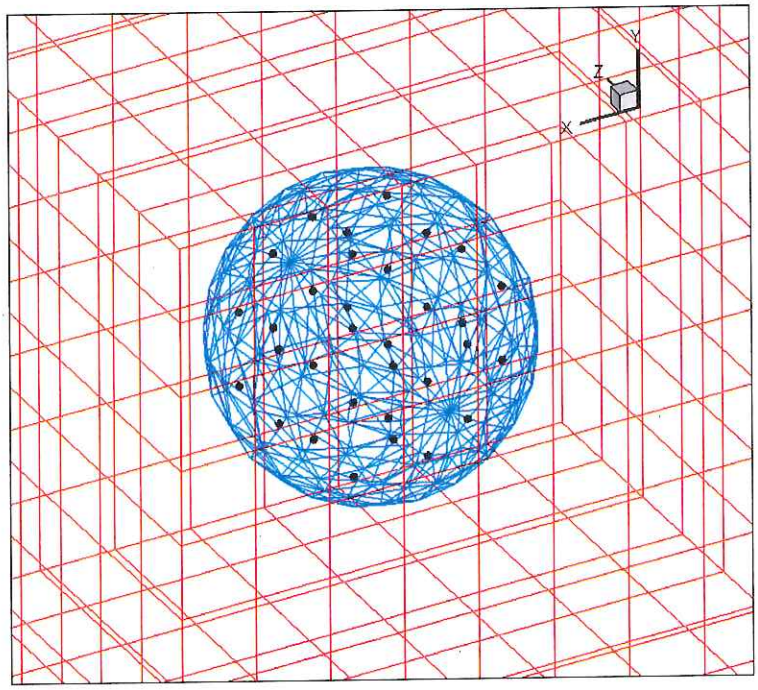

Fig. 3.6 Inclusion test for a point in a polyhedron using Feito's algorithm. Blue line: a sphere, black closed circles: hole points in a polyhedron.

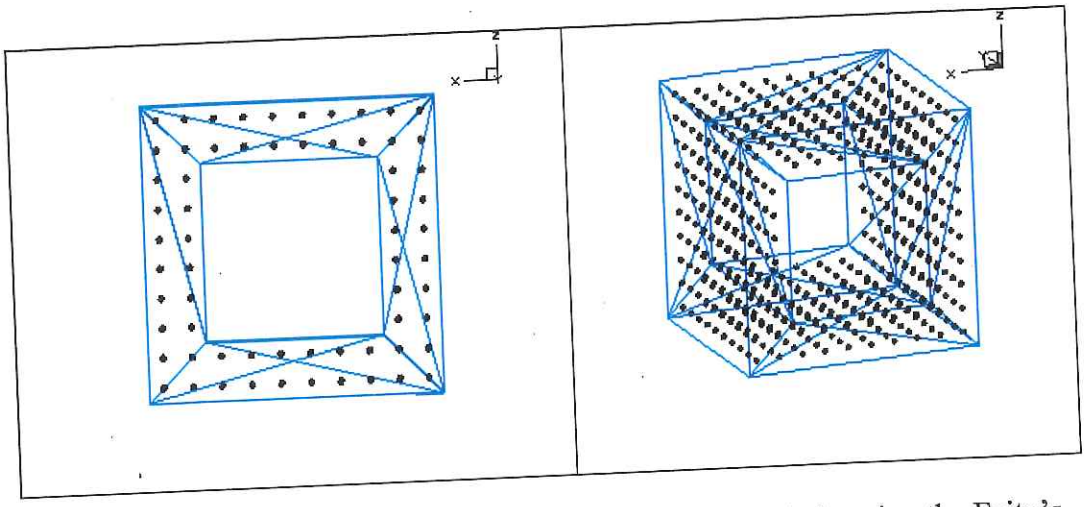

Fig. 3.7 Inclusion test for a point in a polyhedron with a big hole using the Feito's algorithm. Blue line: a given obstacle, black closed circle: points in a polyhedron.

Figure 3.7 shows a geometry having a hole at its center. Here the field grid points are not shown for clear visualization of the obstacle and hole points.

Torsion is a difficult property to observe directly. It has a sign which distinguishes rolling to the left from rolling to the right. We only visualize the unsigned quantity, which we transform using $f(\mathbf{x})=1+R^*|\mathbf{x}|$. The cross-section is an area preserving ellipse with an aspect ratio equal to f (different nomenclature) of the torsion at that point of the curve. The ellipse does not rotate within its frame and the major axis is aligned with the normal vector.

Note that if the number of times the curve winds around the meridian is small but not very small, the torsion gets large when the curve passes the narrow neck of the torus. This is reflected by a skinny ellipse that generats a pronounced ridge on the tube. We chose to use two numbers for naming each object, encoding the number of times the curve winds around the length and around the meridian of the torus.

Figure 3.8 shows a complex geometry which is made of 2 tubes with 10/2 torsions. From the given information of the surface triangle facets (STL format), we can get the hole points of field grid points which are the points inside the geometry. We show the hole points and the scattered surface points in Fig. 3.9. In this case, very coarse Cartesian field grid system is used which has $21\times21\times21$ grid points.

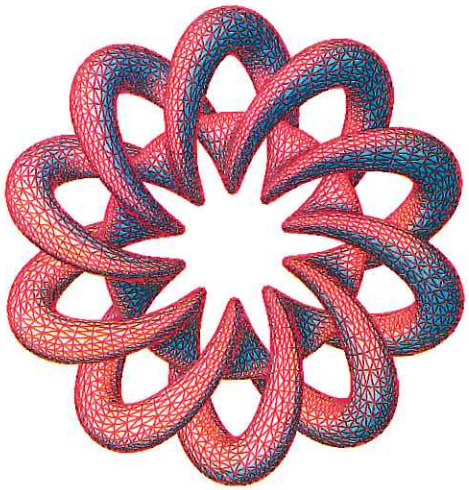

Fig. 3.8 A complex geometry: a torsion with parameter (2 tubes with 10/2 torsions).

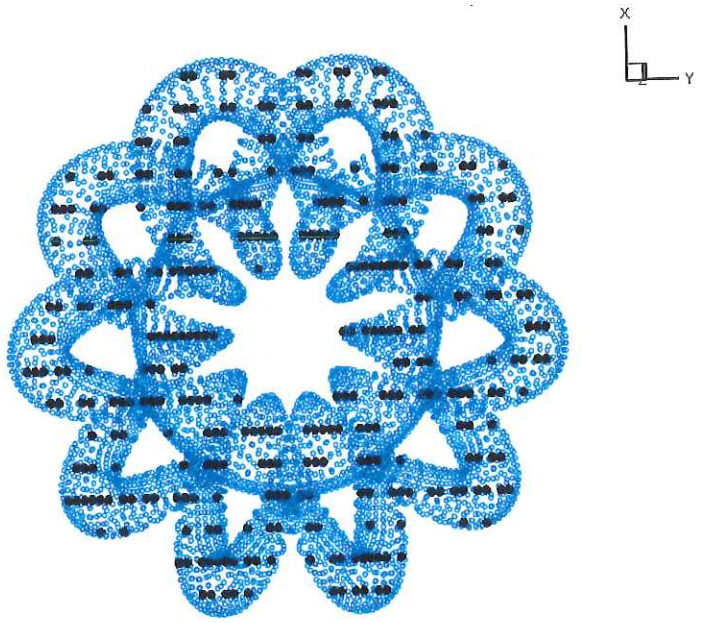

Fig. 3.9 Hole points inside a complex geometry

3.3 Results

The results are collected after the solution has reached a steady state. The steady state condition is checked by calculating the residual at each time step. If the residual is less than 10^{-8} then the solution is expected to reach steady state. The residual is taken on the component of the velocity and is given by the equation below:

$$\text{Residual} = \left[\sum_{j} \sum_{i} \left(\frac{\left| u(i,j)_{t+1} - u(i,j)_{t} \right|}{\left| u(i,j)_{t+1} \right|} \right)^{2} \right]^{1/2} \tag{3.19}$$

Figure 3.10 shows the flow in the channel at a steady state with a grid size of 351x51. The analytical and the numerical results at a downstream location of the channel are compared to see if they are in agreement with each other.

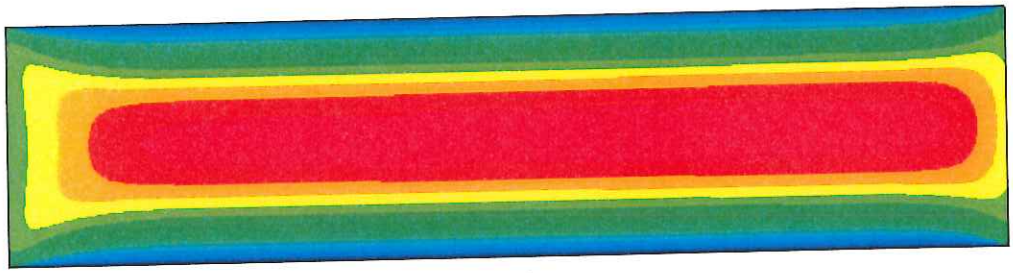

Fig. 3.10 Velocity contours

Figure 3.11 shows the plots of the velocities across the channel at various positions along the channel length. Figure 3.12 shows the comparison between the numerical solution and the analytical solution. It is observed that the numerical results are in good agreement with the analytical solution.

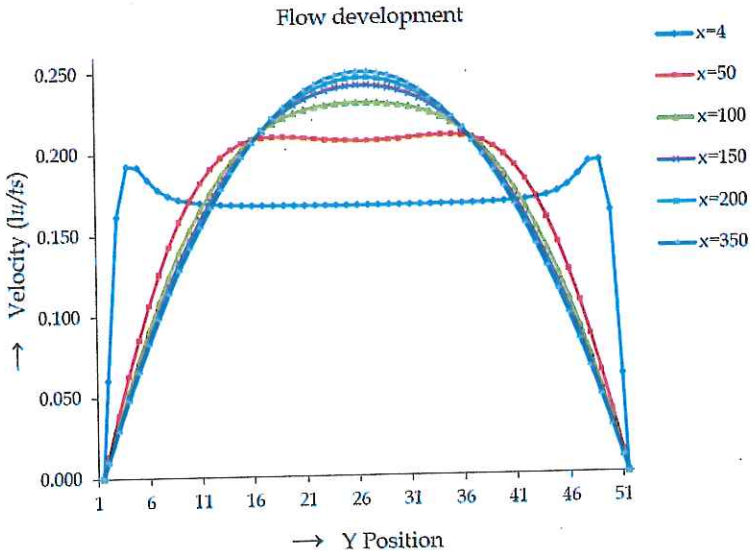

Figure 3.11: Flow development in the channel across various cross section along - direction. The flow is developed towards a complete Poiseulle profile.

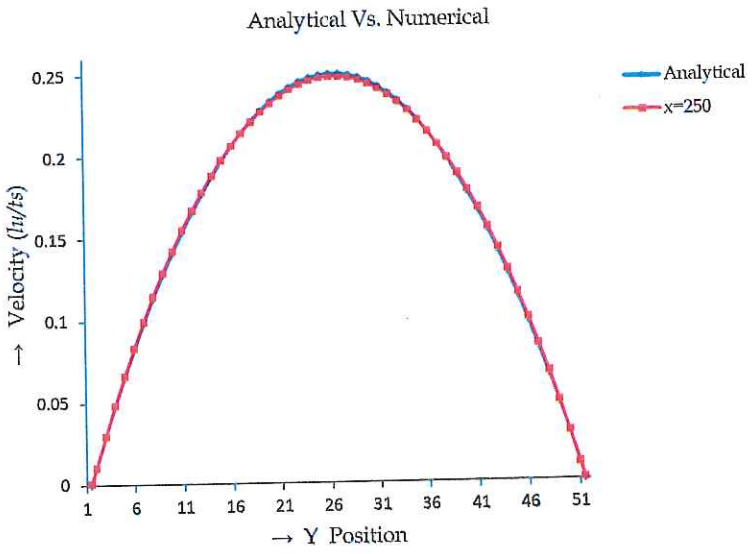

Figure 3.12: Comparison between the analytical and numerical solution. The numerical solution is in complete agreement with the analytical solution.

3.3.1 Flow over a Cylinder

3.3.1.1 Re=100

Flow over a cylinder between two parallel plates was solved using the incompressible D2Q9 LBM. The geometrical specifications of the channel and the cylinder are shown in Figure 3.13. The results were compared with the work of Schafer and Turek [101] who studied the laminar flow over a cylinder for similar kind of geometry. The dimensions are given in terms of the radius of the cylinder. For simplicity, the system of units chosen was lattice units.

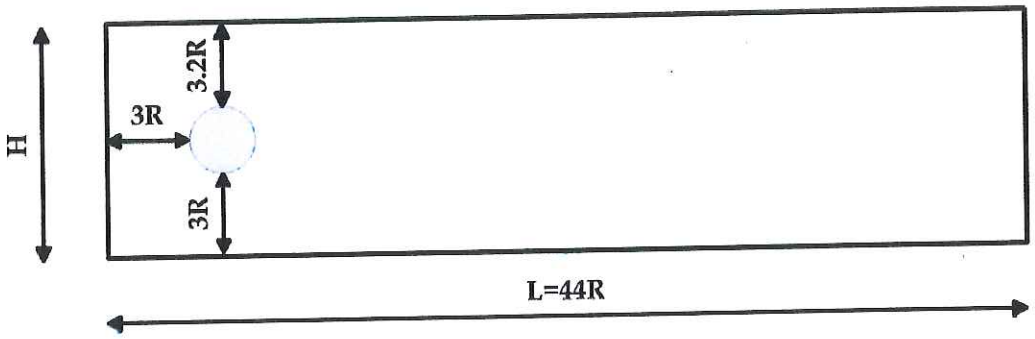

Figure 3.13: Figure showing the geometrical specifications for flow over a cylinder.

Bounce back boundary conditions were used on the channel walls and on the cylinder nodes. Zou-He velocity condition was used to implement the parabolic velocity profile at the inlet. The outlet condition is same as the one implemented for the velocity driven Poiseulle flow.

Figure 3.14 shows the instantaneous velocity contours in the channel. The vortex shedding can be clearly seen downstream of the cylinder.

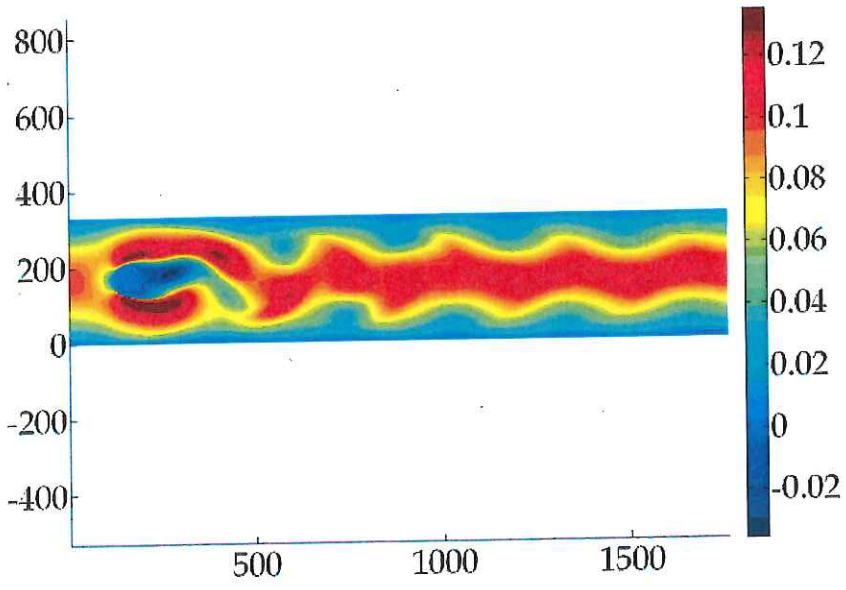

Figure 3.14: Instantaneous velocity contours for flow over a cylinder.

The coefficient of drag is plotted in Figure 3.15. It can be observed that there are two peaks for the drag coefficient here. Similar kind of plot with two peaks can be observed in references [102,103] for flow over a cylinder placed asymmetrically in a channel. The peaks and fall within of the range given by Schaufer and Turek [101].

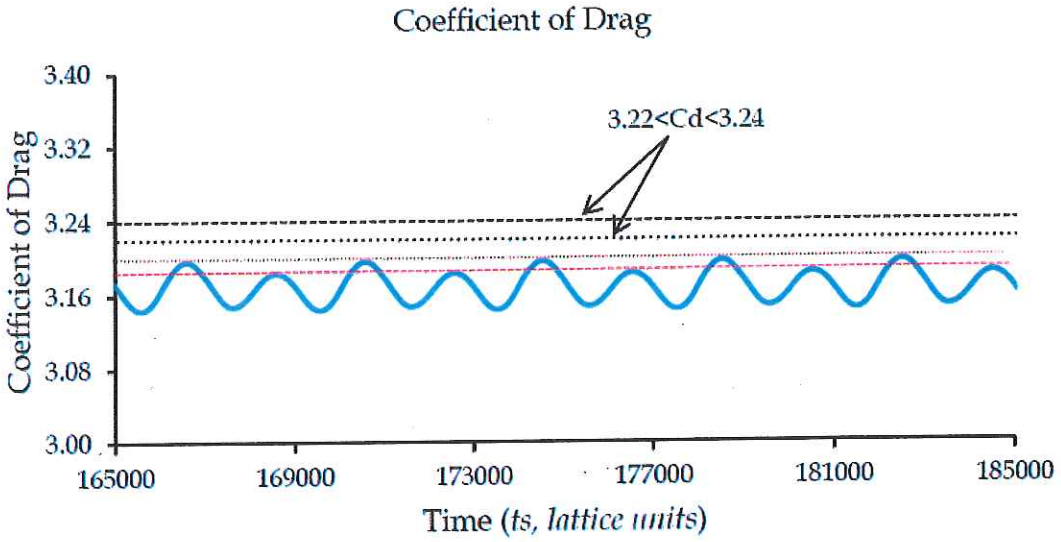

Figure 3.15: Instantaneous coefficient of drag, C_d , for flow over a cylinder (asymmetrically placed in the channel) The dotted lines show the time averaged C_d in [103]

3.3.1.2 Re=21, 400

At higher Re, there is an abundance of flow validations for flow over a square cylinder between two parallel plates. We used this as our second validation study, and this case was solved using the incompressible D3Q19 LBM with a uniform grid of 125×86×26 nodes. Measurements for this case are reported by Lyn and Rodi [104] and Lyn et al. [105] who studied the laminar flow over a cylinder for similar kind of geometry. The Reynolds number was 21,400. The experiment

reported that the separation and the wake were periodic although there was some modulation of the periodicity. The geometry of the flow, including the overall domain size, is given in Fig. 3.16. The dimensions are given in terms of the radius of the cylinder. For simplicity, the system of units chosen was lattice units. The conditions other than the inflow are as follows:

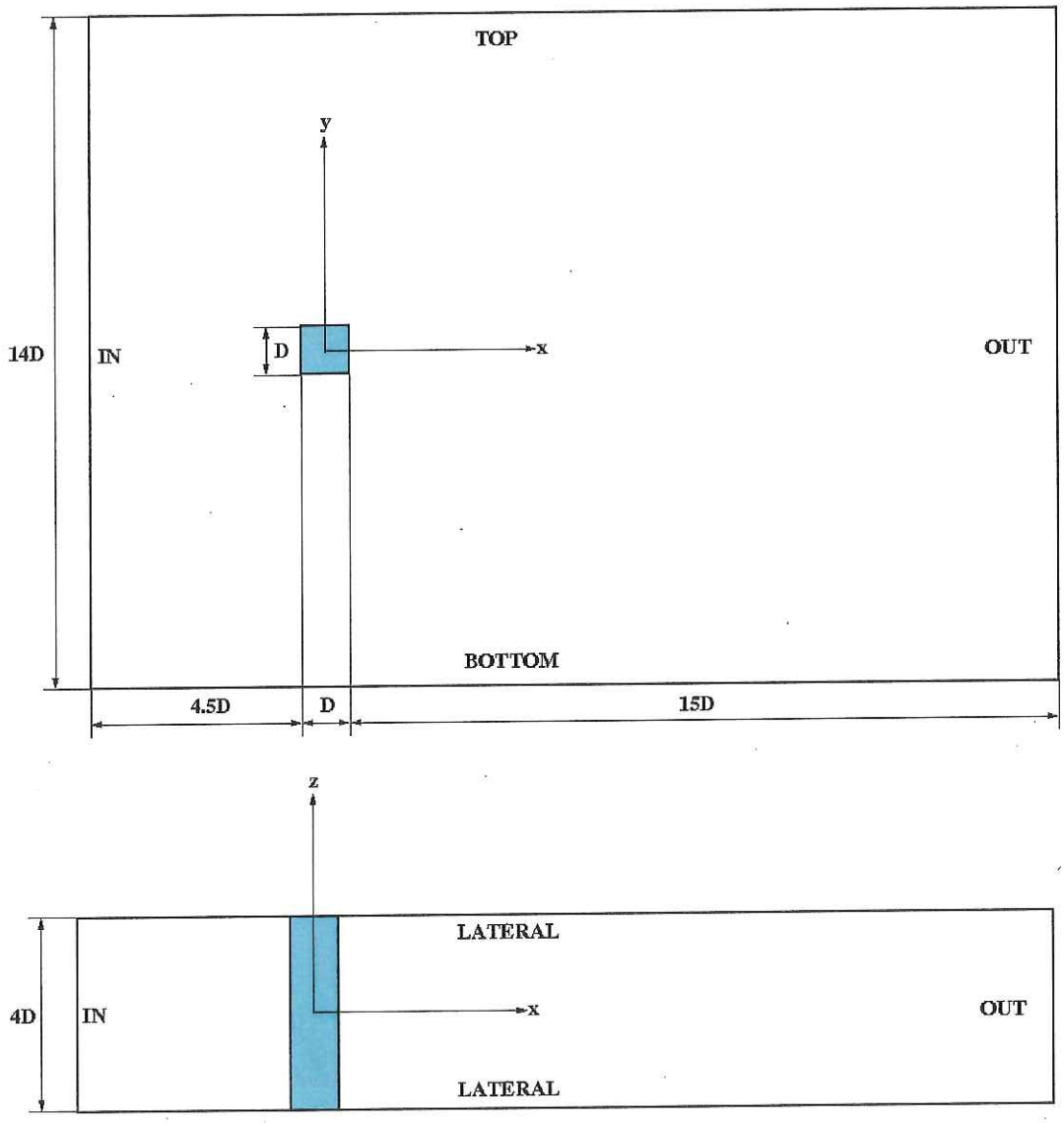

Fig. 3.16 The geometry of the flow around square cylinder showing the geometric dimensions. Shaded region represents the cylinder.

The boundary conditions were applied as follows:

- Slip condition at the lateral boundaries.
- Zero gradient boundary condition at the downstream boundary.
- No-slip boundary condition at the cylinder surface.

Simulations were performed by setting Re = 21,400 and Ma = 0.17 (which results in an inlet velocity of $u_0 = 0.1$) and $\rho_0 = 1$. Our preliminary LBM calculation (using relatively coarse mesh) is compared with numerical results obtained by other authors [106] and with experimental data [107]. Table 3.1 lists the values of the integral parameters for our simulation and other LBM simulations, as well as experimental data of Lyn et al. [107] and other experiments [108]. Our simulation results are similar to those obtained from LBM simulations. The integral parameters shown in Table 3.1 illustrates the close agreement with the literature studies for the time-averaged lift and drag coefficients, C_l and C_d, Strouhal number, St, and recirculation length, l_r.

Data	C_l	C_d	St	l_r
Present work	0.000018	1.80	0.167	1.55
Noble *et al.*[73]	0.002	1.9	0.16	2.7
LES (Others [106, 107])	-0.3~0.03	1.66~2.77	0.066~0.15	0.89~2.96
Exp. (Lyn *et al.* [107])	-	2.1	0.132	-
Exp. (Others [67])	-	1.9~2.1	-	1.38

Table 3.1 Comparison of time-averaged lift and drag coefficients, C_l and C_d, respectively, Strouhal number, St, and recirculation length, l_r

Figures 3.17 & 3.18 show the 2D velocity stream lines for flow around a square cylinder & x-component velocity values at various slices downstream of the flow, respectively at Re=21, 600. The profiles agree well with literature studies [68].

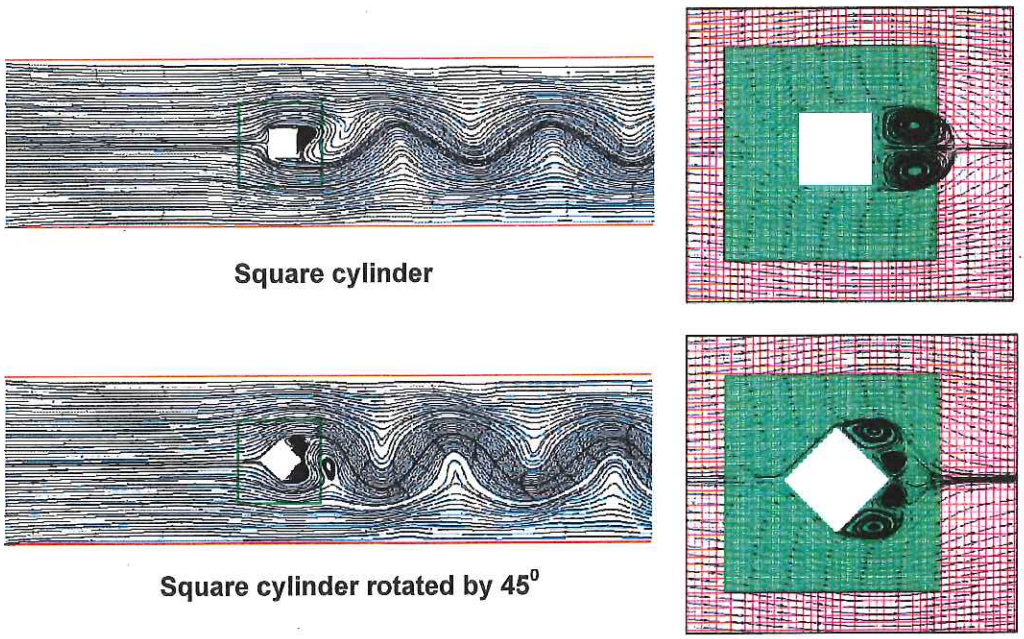

Figure 3.17: Flow streamlines around square cylinder rotated at 0^o and 45^o to the flow at Re=21 400.

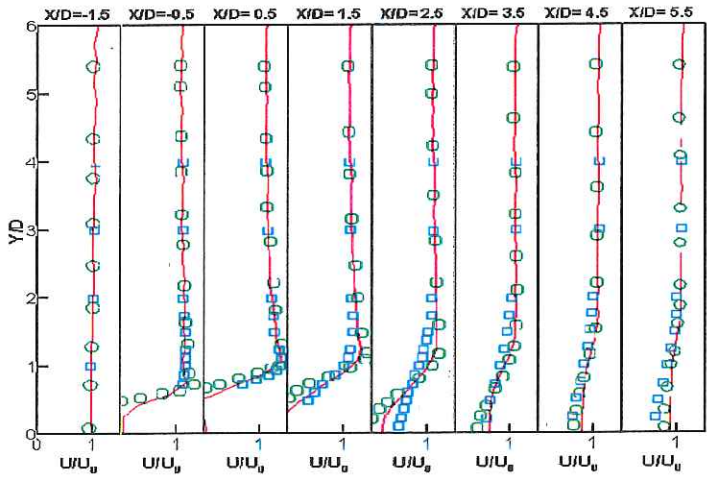

Figure 3.18: Velocity profile along the vertical line (solid line: our results, symbols: literature data [68])

3.4 Summary

In this chapter, we develop and validating an LBM model for single phase flows in full range of Reynolds numbers. The designed LBM is tested with flows in and around microchannels with complex geometries, and our simulation results agree well with literature. After validation, in the next chapter we focus on advanced LBM schemes, which can include molecular information such as the interaction forces between the fluids and porous media system. These interactions result in a host of interesting phenomena including the multiphase flow and thermocapillary flows.

Chapter 4

Multiphase Lattice Boltzmann Method

4.1 Introduction

In this Chapter, we focus on extending the center-piece LBM scheme of our middle-out multiscale model. We preliminarily incorporate the information from atomistic/molecular phenomena in the hydrogen fuel cell (HFC) system via simulating multiphase flows. The term "multiphase" flow can have different definitions depending on the application so the term should be defined to avoid ambiguity. By "multiphase" flow, we mean any flow where the system dynamics cannot be adequately described by the equations of motion corresponding to a single component fluid. One example of such a flow is any particle-laden flow where fluid-particle interactions alter the trajectories of both particles and fluid elements. Other examples include atmospheric transport and clustering of rain droplets in clouds, any interaction at a free surface between two fluids such as that

found between the ocean and the atmosphere, and the boiling of water in a pot. Hence, "multiphase" can refer to any system involving more than one component as long as one of the components is considered a fluid, be it Newtonian or non-Newtonian, in some practical regime. Therefore, the term "phase" has been generalized from the thermodynamic sense. Discounting any interaction with a free surface, the boiling of water in a pot is an example where there exists two thermodynamic phases of the same fluid (water). The free-surface interaction between the ocean and atmosphere is a two-phase system comprised of two Newtonian fluids with no equation of state (EOS) linking the fluids. Particle-laden flows such as those concerning atmospheric interaction with sand dunes involve a Newtonian fluid (air) and a second non-fluid phase (sand particles).

As seen in Table 4.1, the prime difficulty in modeling real life multicomponent/ multiphase fluid-solid is the large separation of scales: The largest flow structures can be of the order of meters, yet these structures can be directly influenced by details of particle-particle collisions and particle-fluid interactions, which take place at and below the mesoscale.

Model Name	Fluid 1 Phase Model	Fluid 2 Phase Model	Fluid-Solid Coupling	Time & Length Scale
CFD Two-fluid model	Eulerian	Eulerian	Bulk flow assumed: no coupling	Engineering (1m, 10^3+ s)
LBM Discreet Particle Model	Eulerian /Lagrangian	Lagrangian	Boundary condition at particle surface: force & velocity exchange	Laboratory (10^{-2} m, 10^2+ s) to Engineering (1m, 10^3+ s)
Molecular	Lagrangian	Lagrangian	Elastic	Mesoscopic

Dynamics			collisions at particle surface	($<10^{-3}$ m, $<10^{-3}$ s)

Table 4.1: Classification of the various models used for simulating dense multicomponent/multiphase fluid-solid flows

The mesoscale methodologies like LBM can easily integrate the Euler-Lagrange class models for multiphase flow from laboratory to industrial scales without much computational requirements for calculation of the forces exchanged between the rigid particles and the fluid. Also, introduction of complex geometries, such as porous media (*e.g.*, multiphase flows in oil reservoirs [109]) also introduces many more challenges to traditional CFD methods. Thus, the approach based on statistical mechanics, *i.e.*, kinetic equation, which can seamlessly incorporate the underlying thermodynamics makes it easy for the LBM to deal with the phase changes and complex surface interactions which otherwise is complicated to model using the traditional CFD techniques.

4.2 Multiphase Models in LBM

We now introduce a few of the most popular and thermodynamically consistent LBM schemes for multiphase/multicomponent fluid-solid lows with parameters that can easily be coupled with molecular methodologies described in Chapter 2. The very physical principle of multiphase refers to phenomenon where a fluid separates into different phases. This phase change might be triggered due to various factors such as change in temperature, pressure, geometry etc. According

to how these factors are treated into the formation of an LBE, there are various multiphase models existing using the LBM, namely

1. Free-Energy (FE), 2. Pseudo-Potential (PP), and 3. Front-Tracking (FT).

Both FE [110-113] and PP [114-117] methods belong to the general class of diffusive interface (DI) methods, whereby the interface between the two phases is not tracked explicitly, but rather defined by the transition region of a given scalar function, typically the fluid density or an equivalent scalar [118]. By definition, this implies that the interface extends over a number of grid sites, whence the denomination diffuse-interface. In the FT method [119-123] the interface is explicitly tracked within the grid. In these methods, the interface is basically a mathematical surface of zero-thickness, hosting a discontinuous jump of the fluid density across the light and dense phases, say vapor and liquid. Since no effort is spent in describing the internal structure of the front, it is clear that FT methods are most naturally addressed to large-scale flows, whereas diffusive interface methods can, in principle, account for the physics of the higher order phase-transition across the interface, so that they are most naturaly targeted to smaller scales.

4.2.1 FE Methods

The model introduced by Swift *et al.* [110] starts with a Cahn-Hilliard formulation for the i-th species the continuity equation of multicomponent fluid, which can be written as:

$$\frac{\partial \rho_i}{\partial t} + \nabla \cdot \rho_i \mathbf{v}_i = 0 \tag{4.1}$$

Here ρ_i and $\mathbf{v}_i$ represent the local density and the velocity of the i^{th} species. The total density of the whole system can be easily recast as $\rho = \sum_i \rho_i$ and it is also conserved. The local velocity is in such a way function of averaged volume velocity $\mathbf{v}$ and of the product between the bulk density ρ_i and the diffusive flow rate $\mathbf{j}_i$ as expressed in the following equation:

$$\rho_i \mathbf{j}_i = \rho_i (\mathbf{v}_i - \mathbf{v}) \tag{4.2}$$

The Eqns. (4.1) & (4.2) can be rewritten for a binary system (where i = 1, 2) and expressed in terms of mass fraction $C = \frac{\rho_i}{\rho}$:

$$\frac{\partial C}{\partial t} + \nabla \cdot (\mathbf{v}C) = -\nabla \cdot \mathbf{j}_i \tag{4.3}$$

Here, $\mathbf{j}_i$ is the diffusive flow rate between two phases. In a two component system (i=2), naming ρ_1 and ρ_2 respectively density for the two components the mean density can be expressed as $\rho = C\rho_1 + (1-C)\rho_2$ .Usually the diffusive flow rate is related to the local composition of two components, thus $\mathbf{j}_1 = -\mathbf{j}_2 = \mathbf{j}$ which leads to the continuity equation:

$$\nabla \cdot \mathbf{v} = 0 \tag{4.4}$$

In terms of the composition C, the mixing energy density for an isothermal system reads as [111]:

$$E_{mix}(C, \nabla C) = E_0(C) + \frac{\kappa}{2}|\nabla C|^2 \tag{4.5}$$

Here C is the mass fraction of one component i and κ is the gradient parameter which is constant. The bulk energy can be rewritten as [111]:

$$E_0(C) = \beta C^2 (C-1)^2 \tag{4.6}$$

Here β is a constant fixing the free-energy barrier between the pure states C = 0 and C = 1. The chemical potential can be expressed as the derivative of E_0 with respect to C:

$$\mu_0 = \frac{\partial E_0}{\partial C} = 2\beta C(C-1)(2C-1) \tag{4.7}$$

The real interaction chemical potential takes into account the contribution of interface curvature which is transported through the Laplacian of concentration:

$$\mu = \mu_0 - \kappa \nabla^2 C \tag{4.8}$$

In Chan-Hilliard theory, the diffusive flow rate is assumed to be proportional to a thermodinamic force, function of chemical potential (μ) gradient:

$$\mathbf{j} = -M \nabla \mu \tag{4.9}$$

Thus, the conservation equation for concentration can be expressed as:

$$\frac{\partial C}{\partial t} + \mathbf{v} \cdot \nabla C = \nabla \cdot (M \nabla \mu) \tag{4.10}$$

This modified continuity equation can be then re-written as a new LBM scheme as follows:

$$g_\alpha^i(\mathbf{x} + \mathbf{e}_\alpha \delta t, t + \delta t) = \frac{g_\alpha^i(\mathbf{x}, t) - g_\alpha^{eq}(\mathbf{x}, t)}{\tau} - \frac{\delta t}{2}(\mathbf{e}_\alpha - \mathbf{u}) \cdot \mathbf{F} \tag{4.11}$$

Where **F** is a forcing term consisting of non-ideal gas effects is expressed as a pressure form:

$$F = \nabla \rho c_s^2 - \nabla p_0 + \rho \kappa \nabla \nabla^2 \rho \tag{4.12}$$

4.2.2 Front Tracking Methods

These class of LBM models use a simplified approach for the study of the interface between two immiscible fluids, based on the similar philosophy of the (Volume of Fluid) VOF technique. The key difference, which also represents the main advantage of the LBM FT approach, is that the single-species transport equation, used in Navier-Stokes/VOF model to determine the relative mass fraction of the two phases, or phase fraction, in each computational cell, is not needed, as the free-surface tracking is automatically performed as shown in Fig. 4.1a, as described in the following.

In the LBM FT model, a single set of LB equations is solved for the heavy fluid, from now on referred to as liquid, while the light fluid (*i.e.,* gas) is neglected in the simulation. The liquid volume fraction is introduced as an additional variable:

$$\varepsilon(x) = \begin{cases} 0, \mathbf{x} \in G \\ 1, \mathbf{x} \in L \end{cases} \tag{4.13}$$

$$0 < \varepsilon(x) < 1, \mathbf{x} \in I$$

in which G represents the gas cells (*i.e.,* empty cells), L the liquid cells and I the interface ones. The domain is then composed of liquid, gas and interface cells, as shown in Fig. 4.1b. The latter contain both liquid and gas and form the closed layer between liquid and gas cells that has to be tracked throughout the computational domain as the free-surface. Only a single layer of interface cells around the fluid cells is used.

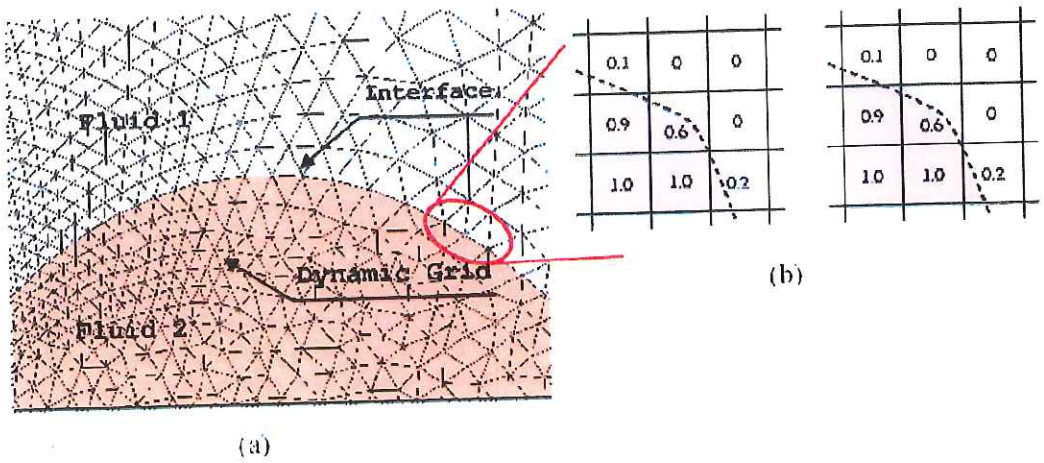

Fig. 4.1: (a) Tracking the interfaces between Fluid 1 & Fluid 2; (b) Mass fractions of Fluid 1 in the cells at the interface

The computation is then subdivided into the following three steps [121,122]:

(a) interface movement: The movement of the fluid interfaced is retrieved by means of the mass contained in the cell, by taking into account both the mass m and the fluid fraction ε of the cell as follows:

$$m(\mathbf{x},t) = \varepsilon(\mathbf{x},t)\rho(\mathbf{x},t) \tag{4.14}$$

Here, ρ can be obtained by an LBE for a specific phase i. Liquid and gas cells are only allowed to transform into interface cells whereas interface cells can be transformed into both gas and liquid cells. Finally, in the interfacial cells, mass and density are completely decoupled, thus the mass evolution does not affect the particle distribution functions.

(b) Free surface boundary conditions: In this step, the empty cells are never accessed during computation. Thus, during the streaming process, only the particle distribution functions coming from liquid or interface cells can be

computed normally, while those coming from the gas phase must be reconstructed from the boundary conditions at the liquid interphase. At the boundary between the phases (*i.e.* interface), the velocity of both is set to be the same and the force performed by the gas is balanced by the one performed by the liquid. The reconstructing procedure [122] provides the missing populations: for an interface cell at site (**x**) with an empty cell at **x** (**x**+cdt), the post-streaming density function f_i is given by

$$f_\alpha(\mathbf{x}, t+\delta t) = f_\alpha^{eq,in}(\rho_{gas}, \mathbf{u}) + f_\alpha^{eq,out}(\rho_{gas}, \mathbf{u}) - f_\alpha^{out}(\mathbf{x}, t) \tag{4.15}$$

where **u** is the lattice fluid velocity at the interface cell.

(c) Cell-type updating: The collision step follows the same rules as in the traditional LBM. Once the streaming and collision steps are completed, the cell type at the interface must be checked: the conversion between gas and liquid must be accomplished by accessing to neighbor cells.

4.2.3 PP Models

This class of LBM schemes allows to account for the interactions between different phases in non-ideal fluids, by means of a generalized force term **F** which accounts for both external fields (such as gravity or electro-magnetic fields) and self-consistent interaction forces associated with intermolecular interactions or any other effective interaction we wish to include.

In this work, we begin by introducing briefly each of the models and specifically focusing on the Shan-Chen class of multiphase LBM models and the results for

commonly encountered multiphase systems. Other models in this class also include Chromodynamic model [123 - 125], modified free energy model[126] and HSD model [127]. Shan-Chen model is based on incorporating the long-range attractive forces between the distribution functions.

4.2.4 Shan-Chen Model

As recalled before in Chapter 3, LBM in single phase is most suited for incompressible flows which do not deviate much from the ideal gas EOS. However, practical considerations and thermodynamic interactions rarely allow for ideal gas assumption to hold true in realistic systems. Thus, LBE has to be modified to incorporate the non-ideal part of the transport phenomena. Shan-Chen models are a class of Euler-Euler models based on calculating multiple LBEs together. A set of n-discretized LBEs one for each of n-fluids present in the system being simulated is solved and then the LBEs are coupled via incorporating the attraction force **F** between the distribution functions. In the original Shan-Chen model the interaction force is approximated using the following equation [114, 128].

The discretized governing equation for the n^{th}-LBE is given in Eqn. (4.16):

$$f_i^n(\mathbf{x}+\mathbf{e}_i\delta t, t+\delta t) = f_i^n(\mathbf{x},t) - \frac{\delta t}{\tau}\left(f_i^n(\mathbf{x},t) - f_i^{eq,n}(\mathbf{x},t)\right) + \mathbf{F} \qquad (4.16)$$

where is the single particle distribution function of the fluid component in the direction. The collision term in the lattice Boltzmann equation is discretized using the BGK- approximation [129], with single relaxation time of each fluid

component given by τ. Assuming low Mach number, the equilibrium distribution function of the fluid component, is given by the Maxwell-Boltzmann distribution as shown in Chapter 3 [130].

In the original Shan-Chen model the interaction force is approximated using the following equation [114,128]:

$$\mathbf{F}(\mathbf{x}) \cong -\frac{d^2 b}{D}\psi(\mathbf{x})g\nabla\psi(\mathbf{x}), \tag{4.17}$$

Where b is the number of nearest sites with equal distance d, D is the dimension of the space (2 or 3) and g is the *temperature like* term. Other neighboring sites (next nearest) can be considered if the term $\nabla\psi(x)$ is evaluated properly [128]. More generally, the equation can be written as [131]:

$$\mathbf{F}(\mathbf{x}) = -c_0\psi(\mathbf{x})g\nabla\psi(\mathbf{x}), \tag{4.18}$$

For a D2Q9 model there are four sites which are at a distance of one lattice unit and other four sites which are at a distance of $\sqrt{2}$ lattice units away from the site where the interaction force needs to be calculated.

Various forms of the interaction force can be developed from formulating the [143]. One widely used formulation with a six point scheme to evaluate the divergence term for the interaction force for a D2Q9 model is given as

$$\mathbf{F} = -G\psi(\mathbf{x})\sum_{i=1}^{8} w_i\psi(\mathbf{x}+\mathbf{e}_i)\mathbf{e}_i \tag{4.19}$$

Here G is the interaction strength, w_i are the weights for LBM model and ψ is the interaction potential which is a function of density. In the summation given by Eqn. (4.19), the values of are considered only if is a fluid node.

For G<0, the force **F** calculated is positive which accounts for an attraction force between the two phases, indicating miscibility. On the contrary, for G>0, **F** is negative indicating immiscibility between the two phases. This attractive force is incorporated [32] into the existing model as an additive term indicating non-ideal behavior as follows:

$$\Delta \mathbf{u} = \frac{\tau \mathbf{F}}{\rho} \tag{4.20}$$

Here $\Delta \mathbf{u}$ is the change in lattice velocity due to the additional force term. The change in velocity is then added to the equilibrium velocity (velocity used in calculating the equilibrium distribution functions) as follows:

$$\mathbf{u}^{eq} = \mathbf{u} + \Delta \mathbf{u} = \mathbf{u} + \frac{\tau \mathbf{F}}{\rho} \tag{4.21}$$

The intermediate velocity is used in calculating the equilibrium distribution functions. The final macroscopic velocity **v** is calculated as:

$$\mathbf{v}(\mathbf{x}, t)\rho = \mathbf{u}(x, t)\rho + \frac{1}{2}\mathbf{F} \tag{4.22}$$

With the incorporation of the additional forcing term the algorithm of the existing LBM model is changed slightly. Additional subroutines are used to calculate the interaction potential and the interaction force **F**. It can be shown that the Equation of State (EOS) of the fluid simulated with the incorporation force as mentioned in Eq. (4.4) is [131]:

$$P=\rho c_s^2+\frac{Gc_s^2}{2}\psi(\rho)^2 \tag{4.23}$$

In lattice units:

$$P=\frac{\rho}{3}+\frac{G}{6}\psi(\rho)^2 \tag{4.24}$$

Equation (4.24) varies for different types of interaction potential functions ψ. One such function proposed by Shan-Chen [114, 128] is:

$$\psi(\rho)=\psi_0\exp\left(-\frac{\rho_0}{\rho}\right) \tag{4.25}$$

where ψ_0 and ρ_0 are arbitrary constants. With this interaction potential the EOS becomes [131]:

$$P=\frac{\rho}{3}+\frac{G}{6}\left[\psi_0\exp\left(-\frac{\rho_0}{\rho}\right)\right]^2 \tag{4.26}$$

The equation of state given above has a non-ideal component. With this equation, for values of pressure below the critical value, two phases (liquid, vapor) can co-exist [128], as shown in Fig. 4.2 below.

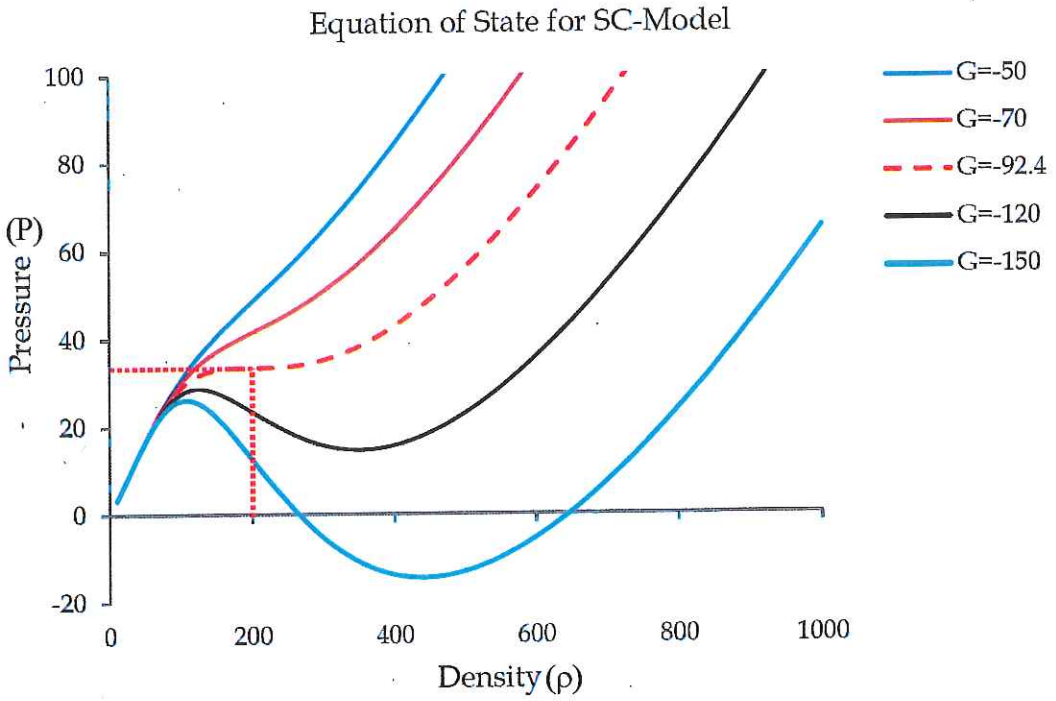

Figure 4.2: The non linear EOS obtained from Shan Chen pseudo potential expression. The critical value of parameter G at which the criticality appears at G=-92.4, as shown by red dotted line

The critical values of the EOS are given by equating the first and second derivatives of pressure with respect to the density equal to zero. From Eqn. (4.24)

$$\frac{\partial}{\partial \rho}\left[\frac{\rho}{3}+\frac{G}{6}\left(\psi_0 \exp\left(-\frac{\rho_0}{\rho}\right)\right)^2\right]=0 \qquad (4.27)$$

$$\frac{\partial^2}{\partial \rho^2}\left[\frac{\rho}{3}+\frac{G}{6}\left(\psi_0 \exp\left(-\frac{\rho_0}{\rho}\right)\right)^2\right]=0 \tag{4.28}$$

By solving the above two equations the critical values are given as:

$$\rho_c=\rho_0 \text{ and } G_c=-\frac{\rho_0}{\psi_0^2}\exp(2).$$

The critical values for the equation of state with are ψ_0=4, ρ_0=200, ρ_c=200, G_c=-92.4. The critical values are marked in dashed lines in Fig. 4.2.

There are two main advantages of the PP LBM models are in simulating multiphase behavior is primarily based on automatically obtaining a non-linear EOS. Taking a one-component system for example, say water, if an appropriate interaction potential was implemented that implied the equation of state of water (as could be determined experimentally), then in principle it would be possible to model the phase change between liquid water and water vapor. In a two component system then, say oil and water, there could be interaction between two fluid components one of which could change its thermodynamics phase. The second purpose is to model a fluid system in which there exists a large difference in the densities of the two fluids.

4.3 Results (I)

To perform a validation check on the code a lattice with periodic boundary conditions on all sides was chosen. The domain is initialized with a density of ρ=200+d, where d is a random number between 0.001 and 0.01. This initial randomization is necessary to create the imbalance between the forces which account for the phase separation [131]. The total number of time steps required for the domain to phase separate into a single liquid droplet surrounded by vapor or vice versa is dependent on the randomization, *i.e.*, for smaller values the number of time steps is larger. The normalized density plots at various time steps were captured. It can be observed that the domain phase separates. These results shown in Fig. 4.3 are in good agreement with the results shown in the reference [131]. The dark portion corresponds to the density of liquid and the white portion corresponds to the density of the vapor.

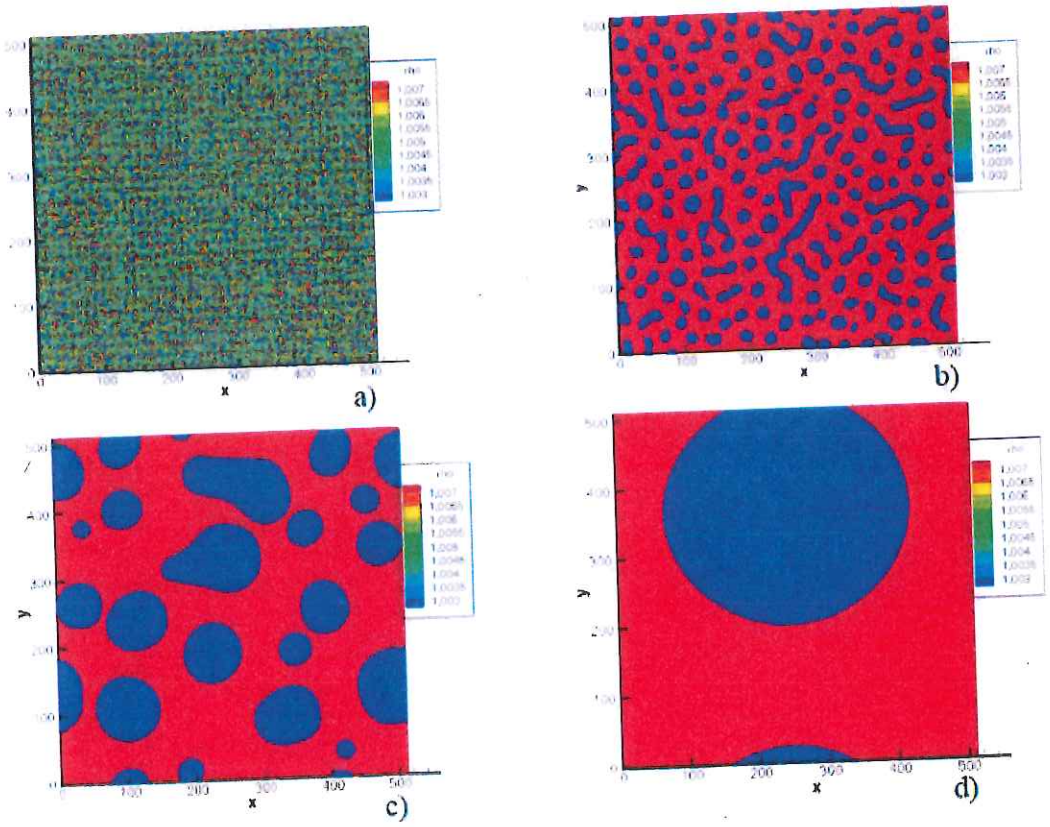

Fig. 4.3: (a)-(d): The segregation and coalescence of a component in the multiphase system. The system is initialized with small perturbation of densities, which allows LBM multiphase models to automatically segregate the densities into various phases.

4.3.1 Incorporating Fluid Wall Interaction

The fluid wall interaction force is given by [128]:

$$\mathbf{F}_{\mathbf{ads}} = -G_{ads}\phi \cdot \psi(\mathbf{x}) \sum_{i=1}^{8} w_i \psi(\mathbf{x} + \mathbf{e}_i)\mathbf{e}_i \; ; \tag{4.29}$$

Here G_{ads} is the adsorption coefficient and ϕ is a function whose value is one if the node is a wall and zero otherwise. Sukop [132] has shown that different contact angles can be achieved between the fluid and the surface by varying the value of G_{ads}. According to Sukop [132], the values of G for different contact angles is given in the Table 4.1. A validation case mentioned in the reference [132] is run to check if the simulation code is working for the contact angles. A similar test case as in section 4.3 was performed except a wall placed in between the domain was run for this purpose. The initial densities (with random variations) chosen in the simulations for contact angles are respectively. Figure 4.4 shows the results obtained.

Contact Angle	G_{ads}
0	-327.79
90	-187.16
180	-46.534

Table 4.1: Values of G_{ads} for various contact angles

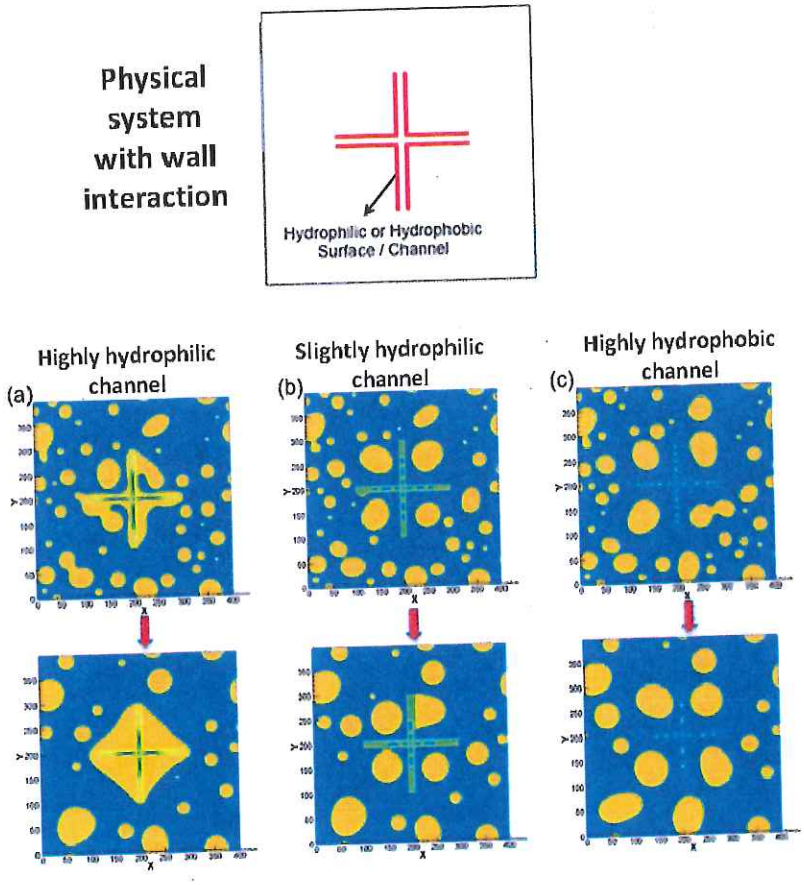

Figure 4.4: (a)-(c): the respective hydrophilic, less hydrophilic, and hydrophobic wall interactions integrated into the system as given in Eq. 4.29.

4.4 Models range of application: Advantages & Disadvantages

It is interesting, from an application-oriented point of view, to compare the capabilities of the above methods for the simulation of a technical problem. The Front-Tracking approach is better oriented towards the simulation of macroscopic phenomena, in which the actions due to the inertia of the fluid are predominant as compared to the other interactions. A typical field of application is that of the free-surface phenomena, like tsunami's, flood waves or tidal waves, characterized by Re numbers higher than 104. The Pseudo-Potential and the Free-

Energy methods, on the other hand, are suited for phenomena from a micro- to a meso-scale. The main problem of the Psudo-Potential methods is related to the presence of the spurious currents, that, however, can be decreased in the 2 – belt model of a factor up to 0.8 [129], while in the Free-Energy approach the lack of some types of boundary conditions at the moment dramatically reduces its applicability to technical problems. In the next Chapter, we introduce a novel methodology of incorporating highly non-linear EOS to obtain high density ratios pertaining to realistic applications, as well as understand the spurious velocity currents production that limits the pseudo-potential models.

4.5 Improving the Density Ratio in Pseudo Potential Models

Equations of state attempt to describe the relationship between temperature, pressure, and volume or density for a given substance or mixture of substances. The beauty of Shan Chen model of incorporating the attraction force but in such a form of the attraction potential that it modifies not only the equation of state but also gives the surface tension through the higher order of Taylor expansion is also one of its disadvantages. the choice of $\psi(\mathbf{x},t)$ is not the best in terms of stability. One can see that if we choose the expression in Eqn. 4.25, $\psi(\mathbf{x},t)$ becomes larger for larger ρ. Thus, the attractive potential contains a "disease" loop, leading to larger external force $\mathbf{F}$ magnitudes and larger velocity values (see Eqn. 4.22) known as *spurious currents,* which lead to instabilities for high density disparities between the lighter fluid (usually gas) and the heavier fluid (usually liquid). Therefore there is a strong demand for developing improvements in Shan Chen

model for increasing the density ratio between the fluids and maintain the numerical stabilities.

In order to improve the density ratios, different equations of state (EOS) including highly non-linear forms should be incorporated. After a thorough review of the literature, it appears that all of the papers using the SC model adopted only the EOS given in SC's original paper and no other EOS have been utilized [132]. There is also a lack of thorough investigations of different EOS for other multiphase LB models. Therefore, it is worthwhile to study the performance of the SC model under different EOS. For the first time, we found that by changing the EOS, one can reach density ratios higher than 1000:1 with the simulation still stable. We will compare the achievable density ratios for different EOS accordingly.

In this chapter, we will compare the following EOS:

I. Shan Chen (SC)

II. Van der Waals (vdW)

III. Redlich Kwong (R-K)

IV. Peng-Robinson (P-R)

V. Carnahan-Starling (C-S)

As shown in the following, except for the SC and C-S EOS, all of the other EOS are cubic in form. The vdW and R-K EOS are two parameter EOS, while the RKS and P-R EOS are three parameter EOS. The vdW EOS is the simplest and yet most famous cubic EOS. Although other modern EOS of only slightly greater

complexity are much more accurate than the vdW EOS, they can be expressed as a general equation:

$$p = \frac{RT}{V-b} - \frac{\theta(V-\eta)}{(V-b)(V^2+\delta V+\varepsilon)} \text{ or} \qquad 4.30$$

$$Z = \frac{p}{\rho RT} = \frac{1}{1-b\rho} - \frac{\theta(1-\eta\rho)\rho/RT}{(1-b\rho)(1+\delta\rho+\varepsilon\rho^2)}. \text{ Here, } V = \frac{1}{\rho}$$

The value for parameters are explained in the following table:

Equation	θ	η	δ	ε
van der Waals (1873)	a	b	0	0
Redlich-Kwong (1949)	$a/T^{1/2}$	b	b	0
Peng-Robinson (1976)	$\theta_{PR}(T)$	b	2b	$-b^2$

Table 4.2: Constants for various EOS

C-S EOS can be given as $p = \rho RT\frac{1+b\rho/4+(b\rho/4)^2-(b\rho/4)^3}{(1-(b\rho/4))^3}$, with a=0.4963 $R^2T_c^2/p_c$, and b=0.187 RT_c/p_c.

Re-arranging Eq. 4.24, we find that for any given EOS, the corresponding expression for pseudo potential can be written as:

$$\psi(\alpha) = \sqrt{\frac{2(p-c_s^2\rho)}{G}} = \sqrt{\frac{2p^*}{G}} \qquad (4.31)$$

For example, vdW EOS can be incorporated into the pseudo potential as:

$$\psi(\alpha) = \sqrt{\frac{2\rho\left(\frac{RT}{1-b\rho} - a\rho - c_s^2\right)}{G}} \qquad (4.32)$$

Where R is the universal gas constant and T is the temperature. At this stage, we develop this novel multiphase LBM scheme for isothermal systems, so we assume RT=1/3.

4.6 Results (II)

To illustrate the outcomes of this model, we now present some results of static bubble coalescence tests for a 3D single-component multiphase system. The 50x50x50 lattice and periodical boundary conditions are used in all of the tests. Initially, two droplets with a radius of r=10 lattice units were placed near the domain with the liquid phase inside the droplets, and vapor phase outside, respectively, as shown in Fig. 4.5(a). The initial densities of liquid and vapor phase were given in the meta-stable region of every EOS, beginning with the values of ρ_{liquid}=500, ρ_{gas}=50. The test was run for 30 000 time steps, and the bubbles were let to coalesce, as shown in Figs. 4.5 (b)-(d). Figure 4.5(e) shows the velocity contour around the final coalesced bubble, with nonzero velocity vectors that are the *spurious currents*, denoted as $\mathbf{u}^s$ hereafter, and indicate the deviation from the real physical situation. This occurs due to the addition of extra force terms in the LBM equation, as shown in Eqn. (4.21). These unphysical spurious currents reach their maximum value at the interface region.

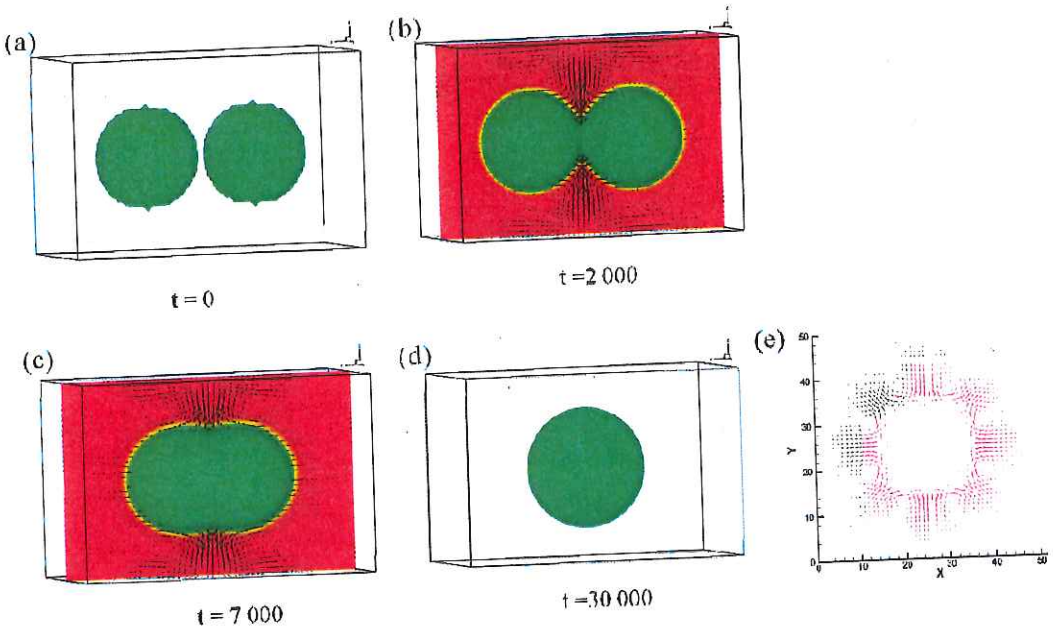

Figure 4.5: Benchmark test case for validating higher non-linear EOS apart from SC EOS: (a)-(d): 3D liquid droplet coalescence, (e): velocity contours around the droplet interface between the liquid and the gas.

Figure 4.6 shows the magnitude of the spurious currents, termed as $|\mathbf{u}_s|_{max}$ changing with the density ratio for the SC and vdW EOS. As can be seen from the figure, for a given density ratio, the vdW EOS generates much smaller spurious currents than the SC EOS. Furthermore, the vdW EOS provides a larger range of density ratios; *e.g.*, when the density ratio equals 103.74, $|\mathbf{u}_s|_{max}$ max for the vdW EOS is only 0.0174, while for the SC EOS, when the density ratio equals 58.497, $|\mathbf{u}_s|_{max}$ max already reaches approximately 0.08.

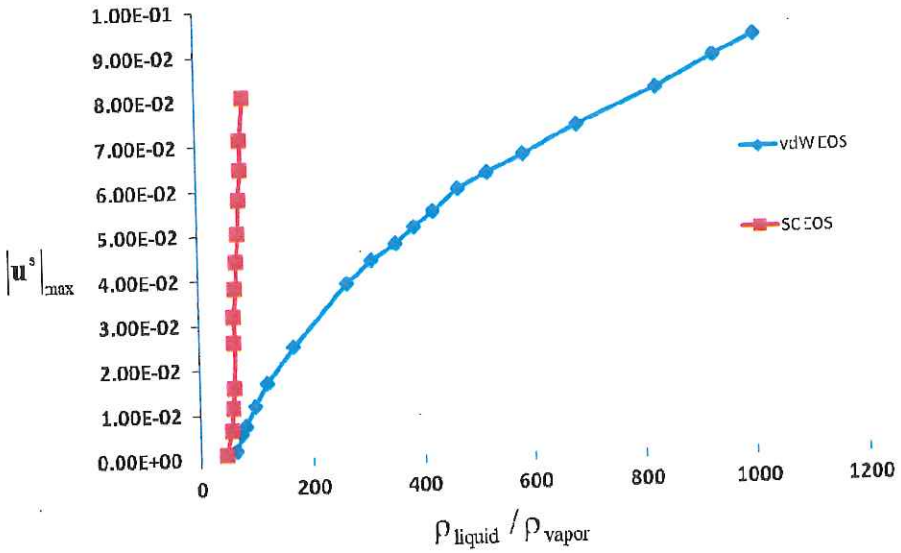

Figure 4.6: Comparison of magnitude of spurious velocity currents in vdw EOS and SC EOS

From Fig. 7 & 8, we can see that at the same density ratio, the higher modified EOS have smaller $|\mathbf{u}_s|_{max}$ max values than the vdW EOS. The $|\mathbf{u}_s|_{max}$ of the R-K EOS is even smaller than that of the vdW EOS. Furthermore, the R-K EOS can also handle a density ratio as high as 1000, with $|\mathbf{u}_s|_{max}$=0.069 when density ratio equals 905.9411. The $|\mathbf{u}_s|_{max}$ for the R-K EOS and vdW EOS are close to each other at lower density ratios. When density ratio is higher than 50, the vdW EOS gives a smaller $|\mathbf{u}_s|_{max}$ max.

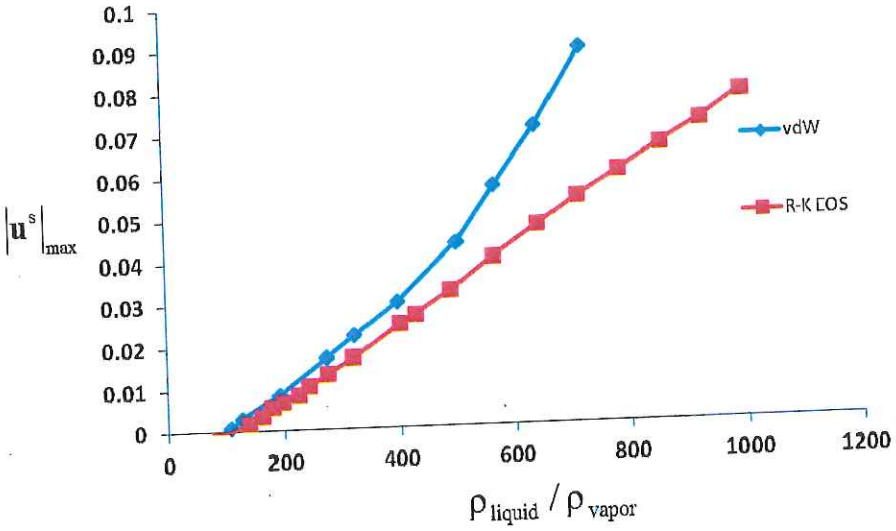

Figure 4.7: Comparison of magnitude of spurious velocity currents in vdw EOS and R-K EOS

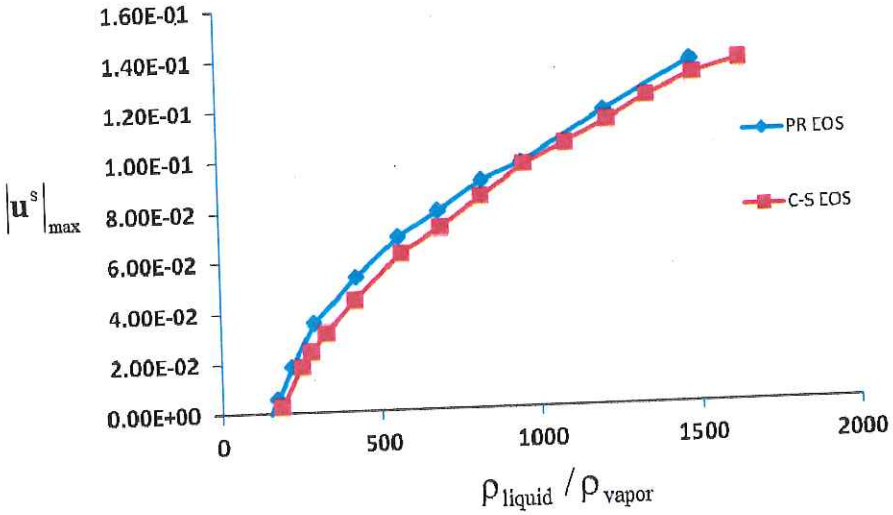

Figure 4.8: Comparison of magnitude of spurious velocity currents in P-R EOS and C-S EOS

We also performed another test, where we simulated the single component multiphase flow of a liquid droplet in a micro channel by using C-S EOS. The

liquid droplet density and the vapor density was initialized in the metastable region of the vdW EOS as 500 and 50 lattice units, respectively and simulated the dynamics of the system. The final result in Fig. 4. 9 shows the movement of the droplet with the liquid to gas density ratio of about 1900.

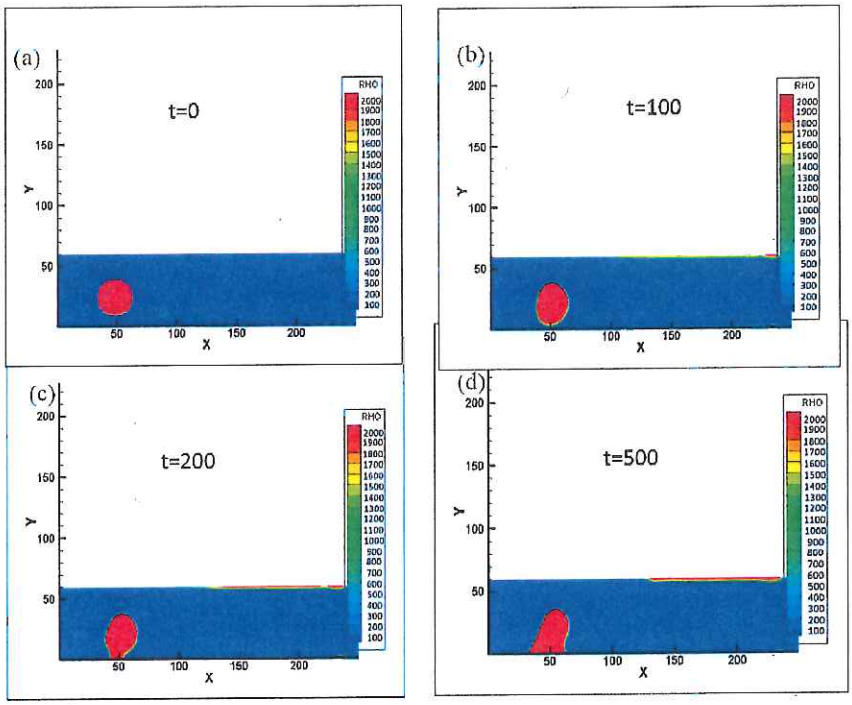

Fig. 4.9 (a)-(d): Water droplet behavior in a microchannel with C-S EOS. The bottom surface of the channel is hydrophilic.

We now utilize our novel realistic EOS incorporation capability of multiphase LBM scheme for single component multiphase simulation of water vapor/liquid water generation & flow in complex porous media. The porous media was generated via obtaining x-ray topology images of the porous media microscopic structure, converting the image into a boolean file containing the details of a point as belonging to the solid (denoted with a value "1") or belonging to the fluid (denoted with a value "0) shown in Fig.10 (a) & (b), and finally incorporating the

structure into the simulation system. Periodic boundary conditions were used in all the faces, and the system was initialized with multiple liquid water droplets in a metastable state in vdW EOS, as stated in the previous result. As shown in Fig. 4. 10, we observed the transient results of the system and observed the interactions of the liquid water droplets with the slightly hydrophobic solid boundaries as well as condensation of water vapor into liquid water droplets in the mesopores of the porous media via capillary action, as shown by the average increase in water saturation percentage in the pores as time increases in Fig.4. 10 (c).

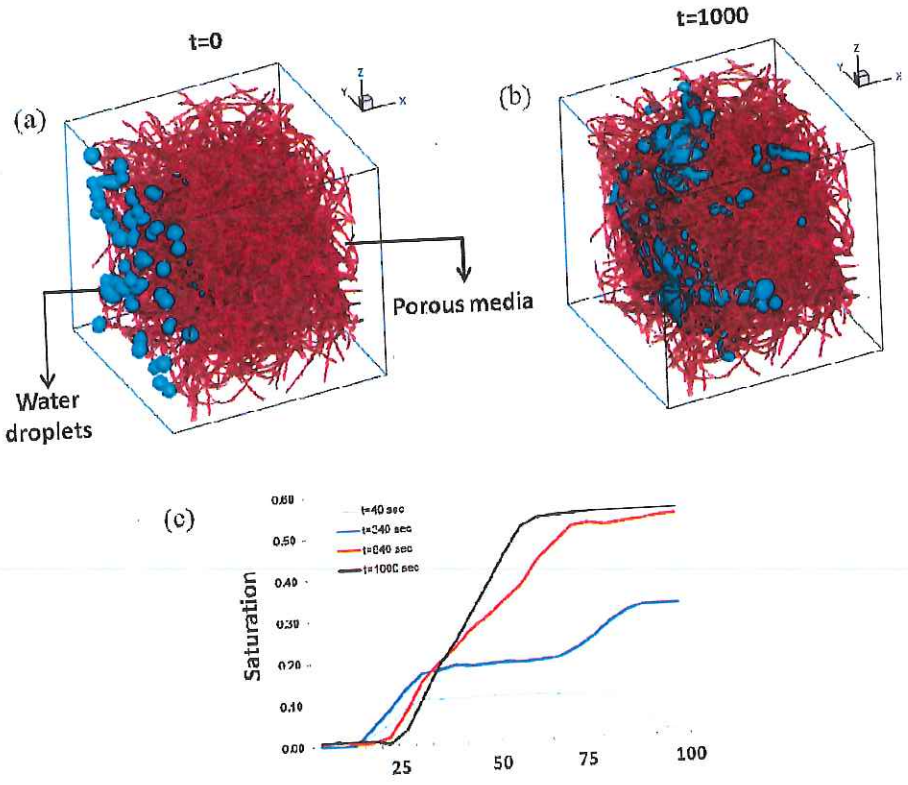

Figure 4.10: (a)-(b): Flow of water droplets in a complex porous media with slightly hydrophobic structures. (c) Saturation curves of % of liquid water increasing inside the porous media as the simulation progresses.

4.7 Summary

In this chapter, we extended our LBM scheme for multiscale modeling in HFCs which tackles one of the most challenging components of HFCs to accurately simulate: the porous gas diffusion layers (GDLs), which are critical in uniformly diffusing the reactant gases to the catalyst layers (CLs). We take advantage of the highly efficient geometry handling techniques in LBM, and develop a non-isothermal multiphase LBM scheme descriptive in GDLs. The GDL structure used in our simulation is reconstructed from x-ray tomography images via the use of stereo-lithography (STL) files. While developing the multiphase LBM schemes, in this work for the first time, we resolve the limitation of low density ratio between the heavier and lighter fluids of 100 inside the multiphase system. We incorporate various types of cubic EOS including van der Waals, Redlich-Kwong, and Carnahan-Starling by generalizing the fluid-fluid/fluid-solid force terms while maintaining the stability of the simulation. This results in increase of the density ratio to around 2 000, and provides a physics based multiphase simulation methodology to understand the air/water or water vapor/liquid water systems inside HFCs. Our generalization of density ratio, given in the thesis now makes LBM to be most promising CFD tools since it incorporates local thermodynamic consistencies in transport phenomena.

Chapter 5

Non-Isothermal Multiphase LBM

5.1 Introduction

Non-isothermal conditions play a critical role in the overall behavior of multiphase flow phenomena and its ability to conduct heat, mass, and momentum transfer in a broad range of applications including energy industries, membrane purification, shale gas exploration, separations *etc.* For example, in the porous gas diffusion layer (GDL) of hydrogen fuel cells (HFCs), since the product is water vapor, there are multiple issues related to the non-isothermal phase changes including (i) production of liquid water and its consequence—blocking the path for reactant gases to diffuse and combine, thereby decreasing the overall efficiency, (ii) liquid water redistribution during operation and shut down, and (iii) the cold start performance[133-136]. An review of the fuel cell literature reveals that studies performed by Mench *et al.* [137-140] have illustrated the important role liquid water plays in degrading the structural integrity of HFCs during freeze damage while operation in cold climates. Furthermore, to restart the fuel cell system, one has to spend precious energy to thaw the frozen water to liquid, and then purge it out via the cathode gas channels before current production. Khandelwal *et al.* [140-141] have shown that if not purged, almost 15–20% of the total energy required to achieve successful cold start can be consumed in melting ice. Thus, a thorough study on the non-isothermal

multiphase phenomena in the complex microstructures of the porous media in GDL is necessary to understand the capillary action of liquid water and its associated vapor-liquid equilibrium properties, thereby further enhancing the durability of HFCs. The findings of such a study can also impact highly on understanding flows in porous media, which are critical in the abovementioned industries.

In this Chapter, we march to complete and extend the LBM multiphase models to simulate real world complex flows by introducing thermal variations inside the systems, and analyzing how the temperature effects the phase change and interfacial dynamics. Chapter 4 focused on the development of state-of-the-art multiphase models in LBM to obtain largest density ratios between the heavy and light fluids, while maintaining numerical stability and the inherent interfacial transport phenomena and physics. Here, we utilize the advantages simple "rule based" incorporation of fluid-fluid and fluid-solid interactions inside the Shan-Chen (SC) multiphase models that *mimic* the temperature variations. Figure 4.6 in Chapter 4 shows the power of SC EOS to predict the change in behavior of the fluid in a system from an ideal gas to real co-existing multiphasic system. The "coupling" parameter G is thought to provide a measure of the microscale interparticle interactions, wherein the increase in the magnitude of G forces the particles inside the LBM system to interact more, thereby spontaneously and physically producing phase change. This is very similar to the role of temperature in a fluid system. Thus, to a certain degree, we can *mimic* temperature changes via changing the parameter G spatially and/or temporally.

We will begin by introducing the methodology developed to model simple thermal flows in a channel via the procedure described above. Further ahead, we will for the first time analyze the multiphase fluid behavior via changing the wettability spatially inside a simple porous media, thereby providing a insight into the complex and less understood thermo capillary system. Once the basics of the system are set up, we will introduce another LBE for accurately simulating the thermal variation, and couple it to the multiphase LBMs and discuss the results.

5.2 Mimicking the Temperature: Case Study

We begin by validating our temperature mimicking approach via comparing our results to the study of Kahndelwal *et al.*[140,141] in the multiphase flow analysis of temperature driven flow in microchannels. Khandelwal *et al.* focused on developing a phenomenological model to understand the temperature driven flow of water vapor produced in the porous media and the related phase change and fluxes of the heavy (liquid water) and light (water vapor) components. The flow phenomena of a condensable vapor induced by temperature variation inside a channel is known as phase change induced (PCI) flow [142]. The system is shown in Fig. 5.1: Due to the temperature gradient present in the channel (the channel is assumed to represent an averaged porous media, with specified parameters porosity ε and hydraulic permeability k), there are density changes in the water vapor that provide the driving force for the vapor flux across the channel to the lower temperature. Here, the water vapor can condense into liquid water

depending on the interactions with the channel boundaries. The vapor flux is related to the temperature gradient via the thermo-osmosis relationship:

$$j_{thermal} = -D_T(T)\nabla T \tag{5.1}$$

Here, D_T is the is the thermo-osmotic coefficient and depends on the hydraulic permeability, mean membrane temperature, and partial molar volume of the solvent, and is the temperature gradient ∇T .

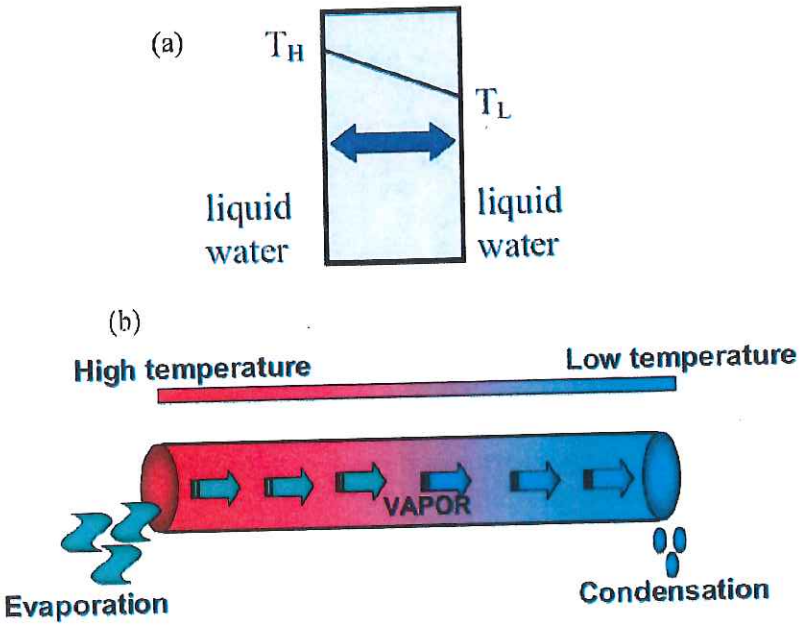

Fig. 5.1 (a) & (b): A sketch of thermally driven phase change induced flow in GDL porous media [143].

The overall mass balance inside the system results in the following equation:

$$\varepsilon\rho_i \frac{\partial s_i}{\partial t} + \nabla\left(D_T^i \nabla T\right) = S_{vap/cond} \tag{5.2}$$

Where s_i is the saturation of one of the phases (water vapor or liquid water), ε is the porosity of the media, D_T^i is the equivalent diffusion coefficient of one of the phases (water vapor or liquid water) in the gas phase and $S_{vap/cond}$ is the vaporization or condensation source term. Eq. (5.2) coupled with the energy equation completes the model, and the result calculated is the change in saturation (liquid water % in the vapor-liquid mixture) across the channel.

We set up our temperature mimicking multiphase LBM scheme in a similar way. To introduce the temperature gradient, we introduce uniform variation of parameter G across the channel as shown in Fig. 5.2. A vdW equation of state is used and the saturated vapor is introduced at the inlet, and the phase change is set to take place automatically where the conditions are suitable.

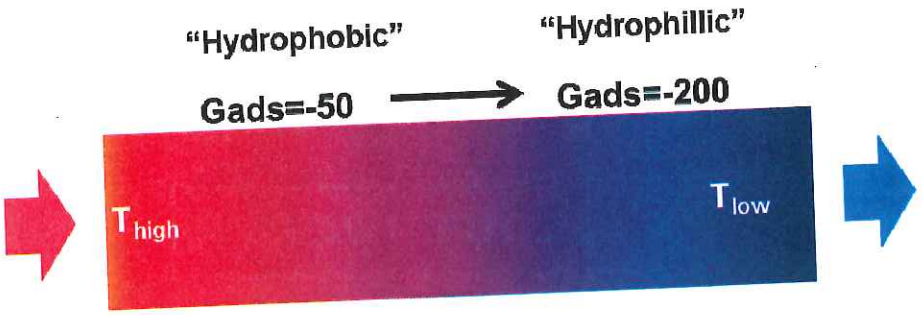

Fig. 5.2: Our LBM system, where parameter G mimics the temperature; it is a simplified illustration of the system in Fig. 5.1 (b)

5.3 Thermocapillary/Thermoosmotic Flow Analysis

Apart from the pressure changes in the capillaries, the introduction temperature in microchannels present in the porous media (*e.g.*, GDL), brings with it very interesting phenomena known as thermocapillary/thermoosmotic flow of the condensed liquids [144]. This has specifically been observed in the case of liquid water condensation and flow inside a saturated porous media. It is expected that the thermocapillary/thermoosmotic phenomena is primarily due to surface tension/contact angle effects on the microscale capillaries present in the porous media [145]. In a recent review Schatz *et al.* [146] focused on the two main contributing factors of magnitude and directions in non-isothermal capillary water flows: the first was described as Marangoni-convection, due to surface tension change perpendicular to the interface. In this configuration the motion ensues with the onset of instability when the surface tension gradient exceeds some threshold value. The second category described is the less known thermocapillary convection, whereby the external imposed temperature gradient is primarily parallel to the interface. In this case liquid motion occurs for any value of the temperature gradient. It is worth noting that in this second case, exerted capillary stress has to overcome viscous resistance in order to have onset of motion. If the porous media is strongly hydrophilic, the liquid water is observed to move from the cold side to the hot side [133,134, & 137]. A thermodynamic explanation offered [147] was the transported entropy of water film in the porous would be smaller than the entropy of water in a free solution, which results in a stable state of the water meniscus. The meniscus then travels from the cold to the hot side

along the hydrophilic channels with strong capillary action. In the case of a hydrophobic membrane, the opposite is observed: when the liquid water forms due to vapor condensation, it travels from the hot side to the cold side, as is expected due to surface tension gradient.

However, accurate measurements and understanding of the thermocapillary phenomena is hampered thus far by the access to local measurements at very small scales. The access to interfacial properties, which are crucial, is limited by the accuracy of the available experimental methodologies including interferometry, holographic interferometry and velocimetry techniques [136]. The physics becomes even more complicated in the presence of liquid evaporation or vapor condensation. Thus, there is an urgent need of accurate and efficient non-isothermal, multiphase simulation techniques, and LBM can provide an accurate physical picture, and tremendously assist researchers in understanding these phenomena.

To simulate and illustrate the effect of thermocapillary flow, we introduce a simple modification in setting up of vdW EOS based high density ratio multiphase SC LBM simulations in a ideal porous media containing a collection of spheres. The ideal system is set up as follows: as shown in Fig. 5.3, a 2D collection of spheres with equal radii is assembled, and the parameter G is spatially varied in Fig. 5.3(a) in the hydrophilic range, while in Fig.5.4b in the hydrophobic range. The inlet and outlet are composed of different values of parameter G that represents a certain temperature gradient. Table 5.1 shows the gradient of parameter G and the corresponding temperature gradient as calculated

from the EOS curves obtained for various G values. At the start of the simulation, saturated vapor is introduced at the inlet, and let to condense and spread via capillary forces for up to 60,000 steps.

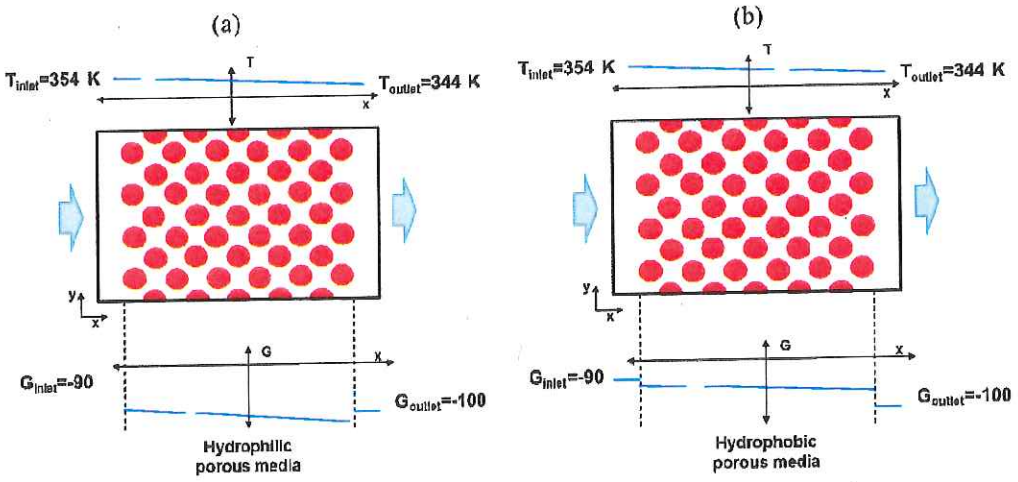

Figure 5.3: Idealized system to investigate the thermocapillary flow: in (a) hydrophilic porous media and (b) hydrophobic porous media

Δ G	Δ T/Δ x (°C/cm)
5.74	5
11.25	10
17.63	15

Table 5.1: A relation of gradient of parameter G and the corresponding temperature gradients in a system

5.4 Results

5.4.1 Mimicking the Temperature

Figure 5.4 shows the transient profiles of liquid-saturation distribution in the porous media with a closed boundary at the outlet for a given temperature gradient of 10°C/cm, as calculated by our LBM scheme and compared to Khandelwal *et al*'s [143] study. This study is done on system shown in Fig. 5.2.

With a closed boundary on the outlet, vapors on the left side diffuse toward the right due to lower temperature, and it can condense anywhere inside the porous media or on the right wall. Shown in Fig. 5.4, our results mimicking the temperature with LBM agree very well with Khandelwal *et al.*'s [143] phenomenological study of the average change in the system saturation (calculated as the spatially averaged % of liquid water). As the configuration marches forward in time, the saturation level at the right side of the channel where the cold region exists increases and advances towards the left side (hotter side). The condensed water on the right side increases the liquid saturation and eventually increases to a value greater than the minimum saturation. As the liquid-saturation value reaches the irreducible saturation value, a dominating backward capillary flow is developed, and eventually, a steady-state condition can be achieved when evaporation and vapor diffusion toward the right are balanced by the backward capillary flux. In addition, our LBM scheme was also able to provide the physical liquid water condensation scenario, which is shown as snapshots of the LBM simulation on the inset of Fig. 5.5 at various stages.

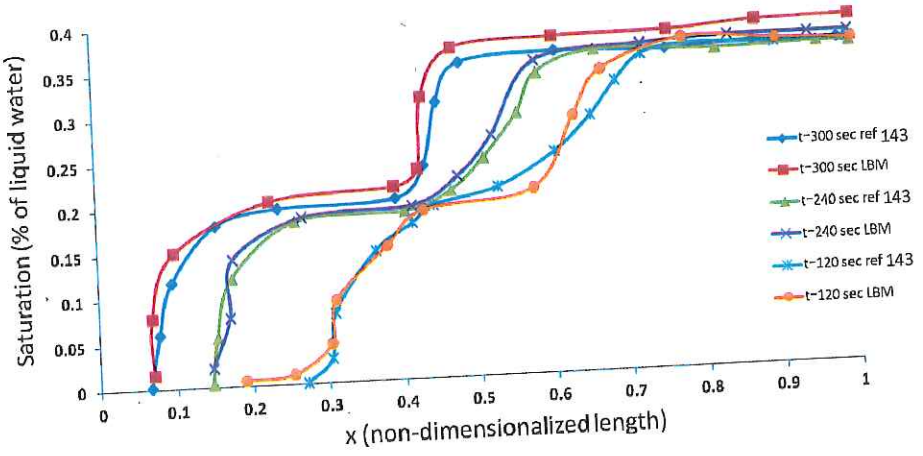

Figure 5.4: Liquid water saturation profiles in a channel predicted by LBM compared to Khandelwal *et al.*'s [143] study

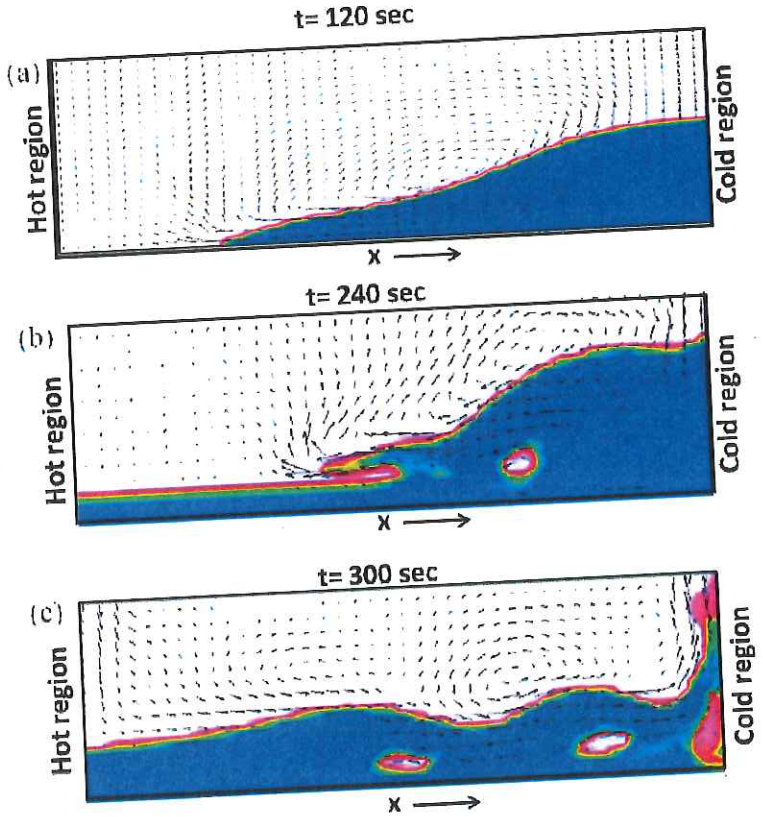

Fig. 5.5: Liquid water condensation at times corresponding to Khandelwal *et al.* [143]

One issue that is of interest is the fact that once liquid water layer is formed via vapor condensation, we observe that the front of the water layer moves from the colder region towards the warmer region in the system. This is not an aberration, but an interesting and less understood phenomenon termed as thermocapillary flow. The following section elaborates more on our investigation into thermocapillary flow in hydrophilic/hydrophobic porous media.

5.4.2 Thermocapillary/Thermoosmotic Flow Analysis in an Idealized Porous Media

In the case of a hydrophobic porous media, as shown in Fig. 5.6 (a)-(d), we see a liquid film forming near the outlet, where the temperature is lower. Once the water layer forms to 20 lattice units thickness in the x direction, the inflow of vapor is stopped and the system is let to proceed with the amount of vapor that is already present inside. The initial formation of this liquid water film then results in higher interaction forces between the vapor present at the nearest neighbors and subsequently leads to condensation and formation of thicker water film. The liquid water film then proceeds to flow from the lower temperature to the higher temperature, which has been observed for the first time in a simulation and is in excellent agreement with previous experimental findings [47]. Water usually flows from the higher temperature to lower temperature regions due to the lower

surface tension in the former do not provide enough resistance to stop the front progressing further. In this case, however, one can clearly see that the hydrophilic nature of the spherical obstacles provides an easy pathway for the water to form long networks with very strong menisci. In our simulation we find that once the water layer reaches near the region with higher temperature, it stops and forms a stable front in our simulation without any movement, as there is no new hydrophilic surface for the water molecules to interact with.

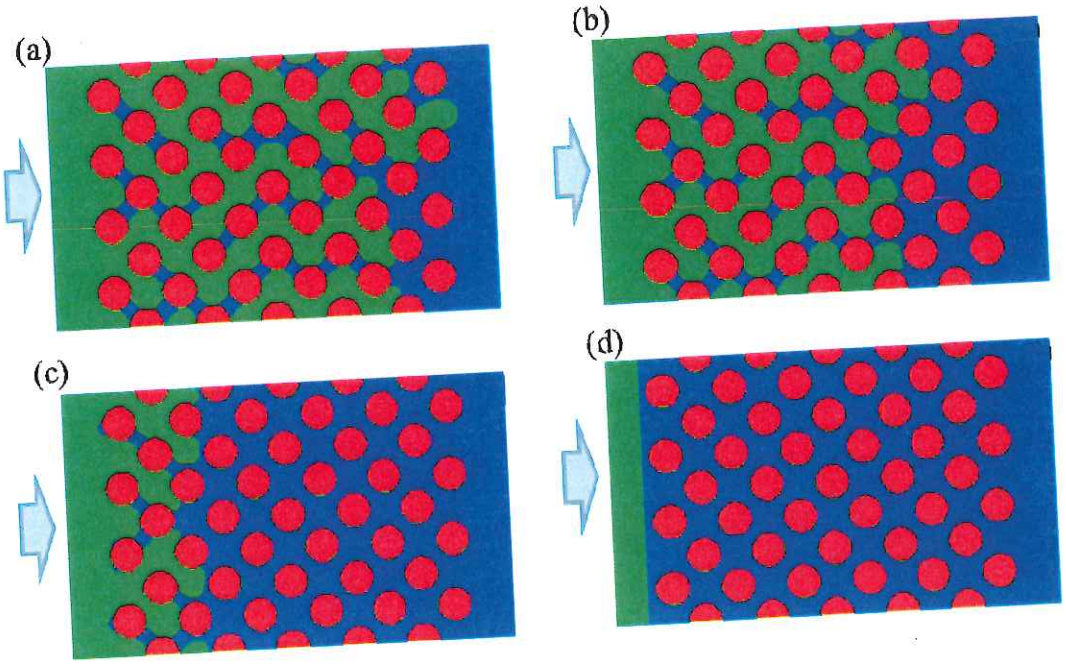

Figure 5.6: Time evolution of thermocapillary flow in hydrophilic porous media, at various reduced times: (a) t*=5, 000, (b) t*=10, 000, (b) t*=40, 000, and (d) t*=60, 000. Arrows indicate vapor inlet. t* is the number of iterations.

The exact opposite movement of liquid water film is observed when the porous media is slightly hydrophobic [148]. As seen in Figs. 5.7 (a)-(d), we observe that the vapor starts condensing into liquid water at the inlet. The liquid water

condensation keeps increasing due to the stronger interaction forces between the vapor molecules and the neighboring liquid molecules in the capillaries, eventually filling the inlet completely, and progresses towards the lower temperature region. The lowering of temperature or increase in the magnitude of parameter G provides suitable conditions of formation of water blobs, which then connect with each other and form a liquid water film.

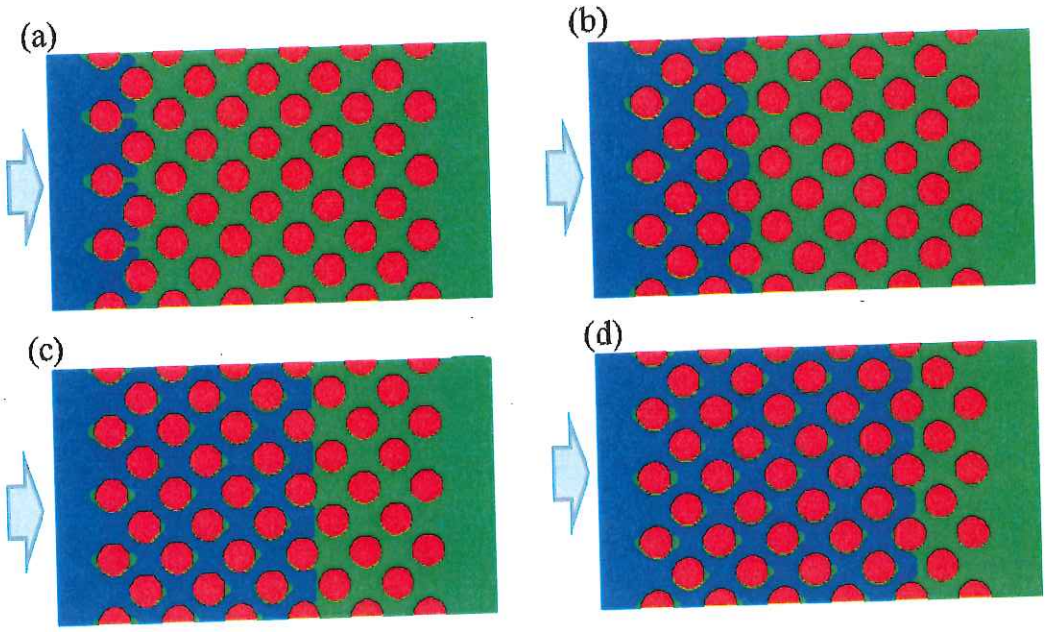

Figure 5.7: Time evolution of thermocapillary flow in hydrophobic porous media, at various reduced times (a) t*=5, 000, (b) t*=10, 000, (b) t*=40, 000, and (d) t*=60, 000. Arrows indicate vapor inlet. t* is the number of iterations.

One solution is instead of *mimicking* temperature effects, one can directly incorporate temperature variations via developing an LBM scheme for solving the energy equation and coupling the heat and momentum transfer together. Another

solution is to couple LBM with more accurate methodologies such as molecular dynamics at specific zones where the molecular/atomistic interactions dominate. In the next section, we will discuss a methodology of developing the former approach of including a thermal LBM scheme with the multiphase LBM scheme.

5.5 Thermal LBM

Although LBM offers an excellent alternative to conventional numerical solving methodologies for isothermal momentum transfer, its application at the energy equation is sometimes results in numerical instabilities. As seen above, in most physical flows, the temperature difference is the driving mechanism for the motion of the fluid. Thus, the need for a stable thermal LBM scheme is desirable. The earliest work was given by Massaioli *et al.* [49] using the idea of the passive scalar for the temperature and this scheme is also used for the highly parallel 3D simulations of Rayleigh–Benard convection [150]. Currently, there are several attempts to construct the thermal models. Luo [151] suggested that the difficulty of solving thermal problems could be overcome by going back to the Boltzmann equation for dense gases and the Chapman-Enskog equation. Alexander *et al.* [152] proposed the multi-speed scheme that expands the equilibrium function to the third-order of the velocity. But the Prandtl number is fixed at the value of 1/2. This limitation has been partially removed by Chen [153] using a two-time relaxation model. He also proposed higher-order parametric equilibrium functions

[153] to satisfy the full set of thermo-hydrodynamic constraints. Nevertheless, the multi-speed scheme suffers from severe numerical instability and the temperature variation is limited to a narrow range. Chen also pointed out that the origin of reducing stability condition is related to the lack of a global H-theorem. Based on this, they stabilized the scheme [154] by identifying a temperature-dependent factor in the equilibrium function that leads directly to the removal of the Galilean invariance artifact, and relaxes the requirement of instantaneous accuracy of this factor. This results in a stable scheme but introduces artificial thermal diffusion, which is strongly dependent on the bulk velocity. The two-distribution functions model, which is called internal energy density distribution function (IEDDF) thermal model by He *et al.* [155], shows great improvement in the stability over the previous LBM thermal models, although a new set of distribution functions is used to describe the temperature dynamics. It is based on the recent discovery that the lattice Boltzmann isothermal models can actually be derived directly by discretizing the continuous Boltzmann equation in temporal, spatial, and velocity spaces. Following the same procedure, the IEDDF thermal model is derived by discretizing the continuous evolution equation for the internal energy distribution. The model has been successfully used to solve some thermal problems in two dimensions [156].

We follow He *et al*'s [155] methodology to develop an LBM scheme that evolves the macroscopic heat transfer described by the energy equation:

$$\frac{\partial T}{\partial t} + \mathbf{v} \cdot \nabla T = \nabla \cdot (k \nabla T) + q_T \tag{5.3}$$

Where T is the temperature, k is the thermal conducitivity, v is the fluid velocity, q_T is the heat source capacity.

In order to simulate the evolution of temperature field, an additional LBM with the distribution function h_i is used:

$$h_i(\mathbf{x}+\mathbf{e}_i\delta t,\, t+\delta t) = h_i(\mathbf{x},\, t) - \frac{\left[h_i(\mathbf{x},\, t) - h_i^{eq}(\mathbf{x},\, t)\right]}{\tau_h} + \delta t w_i q_T \tag{5.4}$$

Where τ_h is the dimensionless relaxation time parameter related to the conductivity as $k = \left(\tau_h - \frac{1}{2}\right)c_s^2\delta t$, $h_i^{eq}(\mathbf{x},\, t)$ is the equilibrium distribution function given as:

$$h_i^{eq} = w_i T\left[1 + \frac{\mathbf{e}_i \cdot \mathbf{u}}{c_s^2} + \frac{\mathbf{uu} : \left(\mathbf{e}_i\mathbf{e}_i - c_s^2\mathbf{I}\right)}{2c_s^4}\right] \tag{5.5}$$

Where the temperature T is calculated by:

$$T(\mathbf{x},t) = \sum_i h_i(\mathbf{x},t)\,. \tag{5.6}$$

5.5.1 Boundary Conditions

The temperature on the wall is imposed by a scheme similar to the bounceback methodology described in Chapter 3. For the Dirichlet condition can be imposed by first calculating the particle distribution function coming from the solid walls as follows:

$$h_i(\mathbf{x}_f, t+\delta t) = -h_{\bar{i}}(\mathbf{x}_f, t) + 2w_i T_w \left[1 + \frac{(\mathbf{e}_i \cdot \mathbf{u}_w)^2}{2c_s^4} - \frac{|\mathbf{u}_w|^2}{2c_s^2} \right] \tag{5.7}$$

Here $\mathbf{x}_f$ is the fluid node, T_w is the wall temperature at boundary node $\mathbf{x}_w$, $\mathbf{u}_w$ is the velocity of the wall node. For adiabatic boundary condition, the boundary temperature T_w can be obtained by solving the equation $\mathbf{n} \cdot \nabla T = 0$ via difference approximation, where $\mathbf{n}$ is the normal to the wall.

5.5.2 Results

To validate the thermal LBM, in the following section we simulate Rayleigh-Bénard convection (RBC). In our simulation, we have two parallel rigid boundaries of infinite length aligned horizontal, as notion think of two plates. The temperature of both boundaries is maintained at two different temperatures, where the bottom boundary is assumed to be the colder one. In between the boundaries a viscous fluid is injected. The problem is stated under consideration of gravity which acts in direction from the upper boundary to the bottom one, compare also with Fig. 5.8.

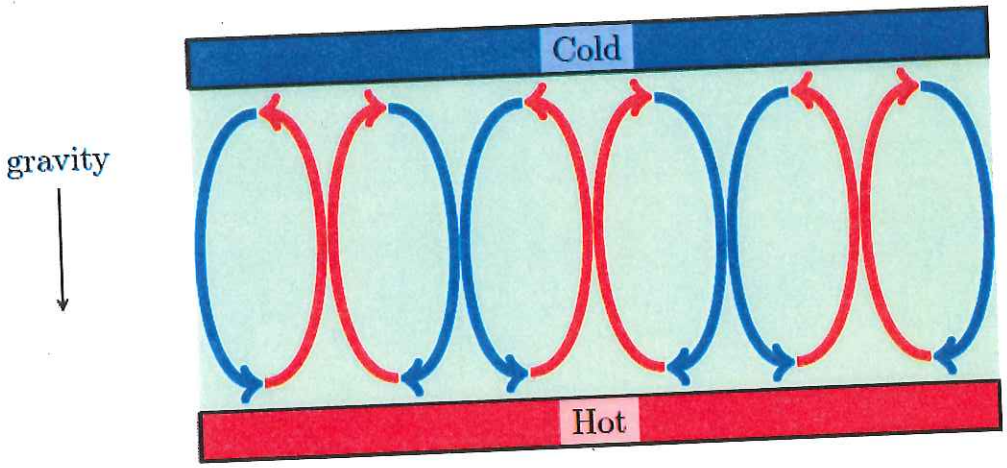

Fig. 5.8: Convection cells displayed at an image section of a two-dimensional Rayleigh-Bénard experiment.

At the beginning the fluid is initialized with a homogeneous density and zero velocity. Except the boundaries, the temperature is initialized constant, in our simulation equal to the colder boundary temperature. When the thermal LBM alone is run until steady state, the temperature distribution would assume a linearly increasing profile due to diffusion from the top to bottom as seen in Fig. 5.9.

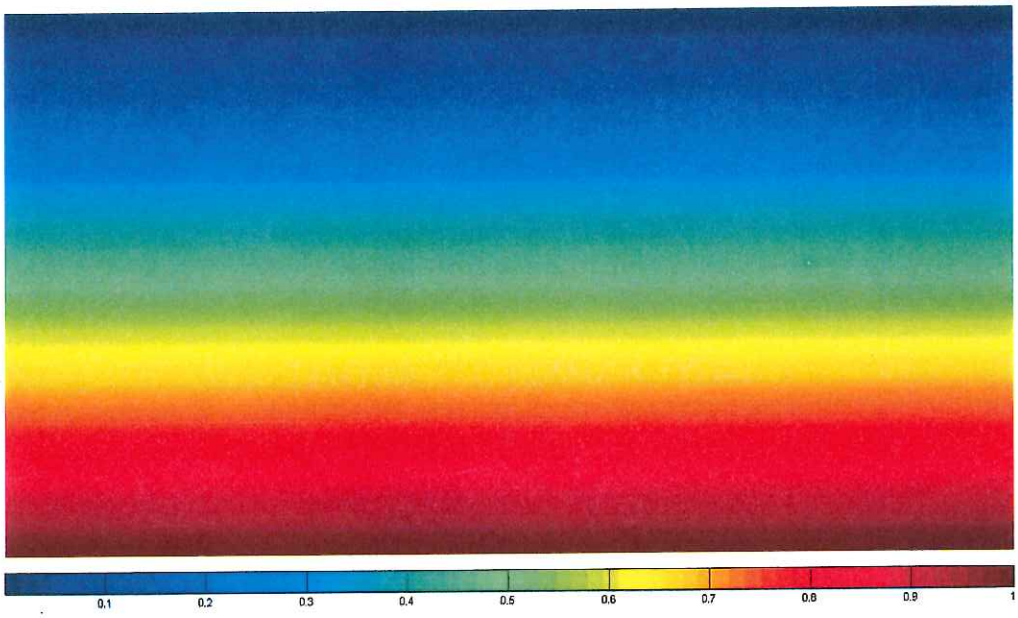

Fig. 5.9: Temperature profile between two boundaries maintained at two different temperatures without considering the influence of gravity. Boundary at the top is colder than the one at the bottom.

Once the thermal and single phase fluid LBMs are coupled and gravity is introduced, we can simulate the RBC. Figure 5.10 shows the motion of the fluid between the two boundaries, where a circular motion is observed, consistent with other benchmark calculations[155].The resulting temperature profile is shown in Fig. 5.11, where we can also observe convection cells.

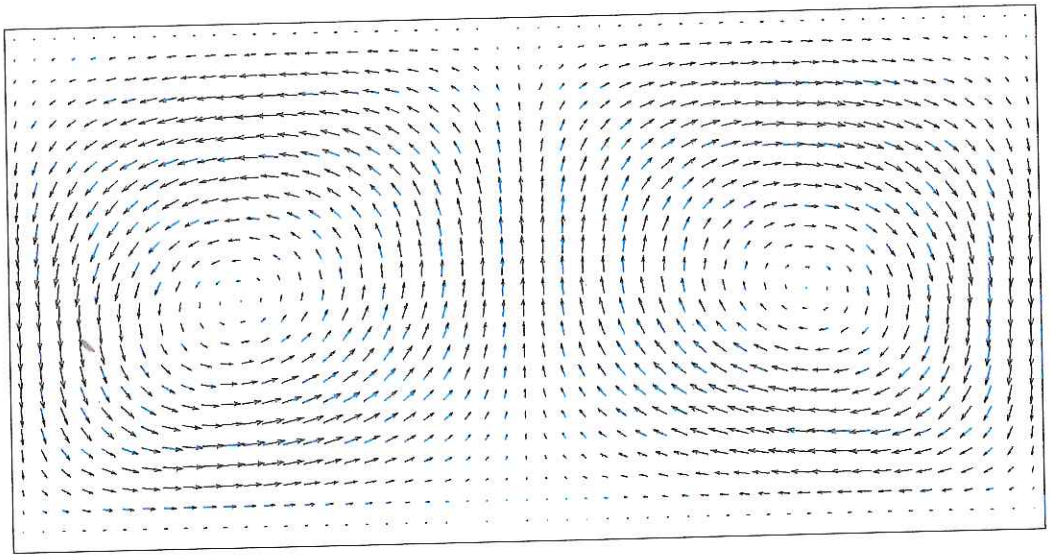

Fig. 5.10: Vector field illustrating the fluid's movement in a simulation of 2D Rayleigh-Bénard convection. The bottom surface is hotter than the top one.

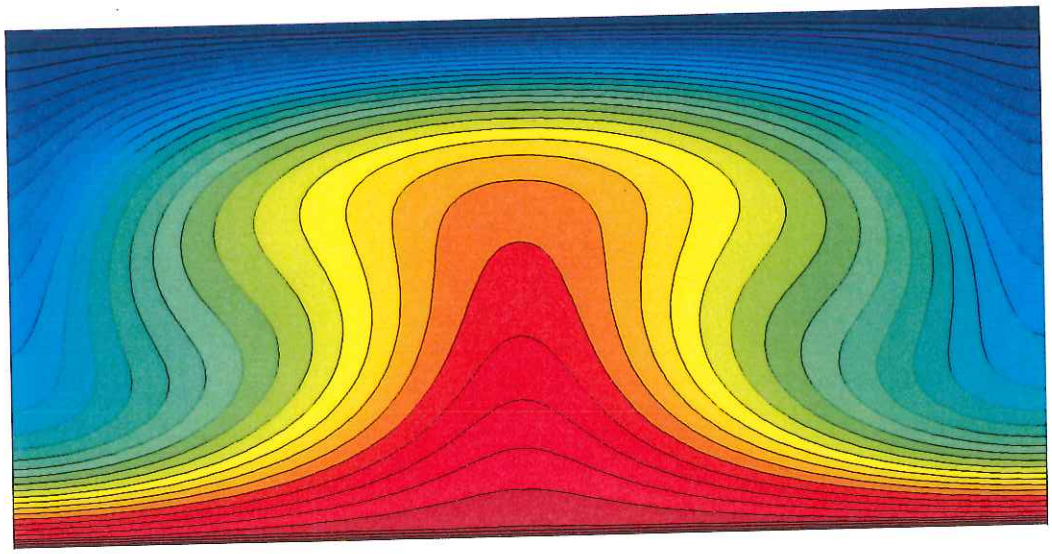

Fig. 5.11: Resulting temperature profile in a simulation of two-dimensional Rayleigh-Bénard convection. Lines are isotherms connecting points that have same temperature.

5.6 Thermocapillary Movement of a Droplet on a Surface

Following the preliminary attempt by Kang *et al.* [157], we now attempt to couple the vdW equation of state multiphase LBM with the thermal LBM to obtain the most accurate attempt to investigate and understand the thermocapillary flow of water droplets surrounded by vapor, on a surface. The temperature boundary conditions are similar to the RBC case study, and for the multiphase LBM, we introduce a water droplet on a slightly hydrophobic surface with contact angle of 95°, along with periodic boundary conditions in the inlet and outlet. The conversion from the contact angle to the parameter G_{ads} is taken from Table 4.1 in Chapter 4. The system is closed, so there is no vapor coming in. The first challenge is to incorporate the surface tension variation with temperature which can be described as follows [157]:

$$\sigma(T) = \sigma(T_{ref}) + \frac{\partial \sigma}{\partial t}(T - T_{ref}) \tag{5.8}$$

Where T_{ref} is the reference temperature chosen as STP conditions, $\sigma(T_{ref})$ is the surface tention at T_{ref}, $\frac{\partial \sigma}{\partial t}$ is the surface tension gradient w.r.t temperature.

Utilizing the external force approach as described in Chapter 4 for Shan Chen models, we introduce an extra force $\mathbf{F}_{ST}$ that introduces the following relation [157]:

$$\mathbf{F}_{ST} = \frac{3\sqrt{2}}{4}\varepsilon_0\left[\frac{1}{2\varepsilon_0^{\,2}}\left(\phi^2 - 1\right)\nabla\sigma - \left(\frac{\phi^2 - 1}{2}\cdot\nabla\sigma\right) + \frac{\sigma}{\varepsilon_0^{\,2}\mu}\right] \tag{5.9}$$

Where ε_0 is a constant, ϕ denotes the interface: ϕ=1 or -1 if the point x lies in any of the two phases, and ϕ=0 if the point x lies at the interface. The force term in Eqn. (5.9) is added to the Shan Chen force term (modified for vdW EOS, as discussed in Chapter 4).

5.6.1 Results

Figure 5.11 gives the time evolution of droplet shape, position, and streamlines patterns around the moving droplet. At t=50, 000 (Fig. 5.12 (b)) we can observe that a clockwise rotating vortex starts to appear at the bottom wall inside the droplet close to the front end. As the droplet moves forward, the internal vortex becomes larger, meanwhile it is elongated backwards due to large flow resistance.

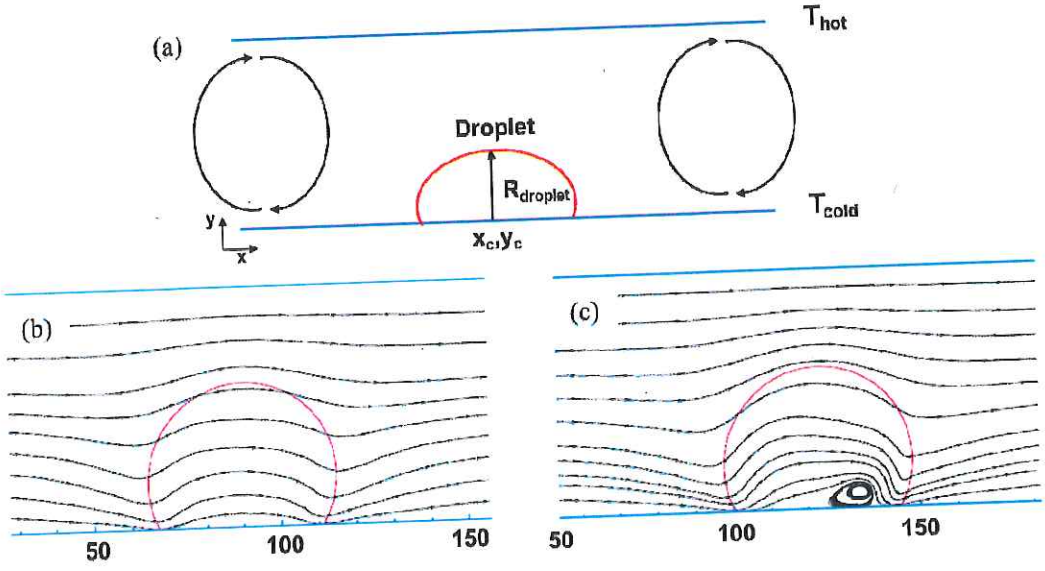

Figure 5.12: (a) System for testing of thermocapillary movement; (b) & (c): droplet movement due to surface tension change via thermal gradient for t*=30, 000 & t*=50, 000, respectively.

This effort proves the capability of LBM in general to simulate complex flows with non-isothermal conditions, as well as incorporate the interfacial effects between two phases and the surrounding surfaces. Future extensions of the above mentioned methodologies could be made to include a porous media to demonstrate the dominance of the microscale capillary effects such as Marangoni flows as well as the thermocapillary flows.

5.7 Summary

In this chapter, we further investigate the effect of temperature changes inside the GDL and in HFC systems on the multiphase condensation and movement & behavior of resultant liquid water. We provide a novel and easy methodology to "mimic" the temperature changes in porous media via temperature dependent fluid-fluid/fluid-solid interaction forces along the system. This results in the system behavior similar to the incorporation of temperature without the additional instabilities. Our results of temperature mimicking induced condensation of water vapor to liquid water in a microchannel agree very well with phenomenological models and experimental data in literature. For the first time, we were able to physically understand the thermoosmotic/thermocapillary phenomena that occurs in porous media: we found that depending on the hydrophilicity or hydrophobicity of the porous media, the flow of condensed water changes from hot to cold regions or cold to hot regions, respectively. This phenomenon has only been observed recently, and is not numerically resolved yet. We also develop a parallel thermal LBM code and couple this with the multiphase LBM mentioned earlier.

Using Cahn-Hilliard theory, the additional forcing term arising from the surface tension gradient of liquid water depending on the calculated temperature at a local point is added. We perform a simple case study of liquid droplet movement on a microchannel substrate induced by temperature changes in the system.

Chapter 6

Conclusions

In this chapter, we present the major findings and contributions of our thesis work and provide recommendations for extending this work in the future.

6.1 Conclusions and Contributions

In this work, we have constructed a novel middle-out multiscale model for a benchmark case study in the alternate energy area— namely, hydrogen fuel cells (HFCs). We organized our work based on the centerpiece of our multiscale model, which is the lattice Boltzmann method (LBM). Our findings are summarized as follows:

- In Chapter 2, we develop a novel middle-out multiscale methodology in which a versatile centerpiece mesoscale level model based on kinetic theory is adopted as the foundation, where the model is hybridized to link information simultaneously from the atomistic/molecular models, as well as the continuum models. Our middle-out approach is favorable to the traditional "top (continuum) to bottom (atomistic)" scale used by process system engineers (without specific knowledge of the molecular architecture) or "bottom to top" scale used by scientists which is extremely time consuming for design purposes. This dissertation develops a highly computationally efficient mesoscale level methodology based on

kinetic theory known as lattice Boltzmann method (LBM) as a critical component, which was developed in-house, and can link parameters from bottom as well as top levels. LBM assumes that the transport phenomena in fluids is due to the movement and interactions (collisions) of fluid molecules with themselves as well as the surroundings, which is very similar to the treatment of systems in molecular models, thus providing an efficient coupling. LBM also has an advantage of easily hybridizing with continuum models as an alternative to CFD and ideally suited for incorporating molecular information with computational efficiency and is extremely suitable for parallel computation. To develop and validate this model, we utilize benchmark case study of the hydrogen fuel cell (HFC).

- In Chapter 3, we develop and validating an LBM model for single phase flows in full range of Reynolds numbers. The designed LBM is tested with flows in and around microchannels with complex geometries, and our simulation results agree well with literature.
- In Chapter 4, We extended our LBM scheme for multiscale modeling in HFCs which tackles one of the most challenging components of HFCs to accurately simulate: the porous gas diffusion layers (GDLs), which are critical in uniformly diffusing the reactant gases to the catalyst layers (CLs), where the reaction of hydrogen and oxygen combining to produce water vapor takes place. The major bottleneck in durability of current HFC designs is the occurrence of multiphysical phenomena including phase changes of water in vapor and liquid states, which blocks the active

reaction sites in the CL, thereby decreasing the overall performances. A thorough analysis of this behavior has proven difficult, as the inclusion of realistic and complex porous media structure increases the scale of computation time for current methodologies. To resolve this issue, we take advantage of the highly efficient geometry handling techniques in LBM, and develop a non-isothermal multiphase LBM scheme descriptive in GDLs. The GDL structure used in our simulation is reconstructed from x-ray tomography images via the use of stereo-lithography (STL) files. This approach to complex geometries provides a Boolean identifier tag to each point to separate points in both solid and fluid phases. The solid boundary conditions are straight forward extrapolations of the LBM distribution function values, which require less time to compute.

- Furthermore, We generalize the multiphase LBM based on the pseudo potential model, where the non-ideal behavior of fluids due the fluid-fluid interactions (occurring because of the difference in interaction strength between molecules in the liquid phase and the gas phase) is incorporated inside the lattice Boltzmann equation framework via an force term, which then links the multiphase LBM to a non-ideal equation of state (EOS), thereby accurately incorporating local thermodynamics. Depending on the sign and magnitude of the force, we can simulate miscible/immiscible phases for single/multi component. Solid-fluid interactions can also be incorporated via an adsorption like force term, which is dependent on the number of nearest neighbor points belonging to the solid. Similar to the

fluid-fluid force term, the sign and magnitude of the adsorption force term can change the behavior of the solid between hydrophobic and hydrophilic. While developing the multiphase LBM schemes, in this work for the first time, we resolve the limitation of low density ratio between the heavier and lighter fluids of 100 inside the multiphase system. We incorporate various types of cubic EOS including van der Waals, Redlich-Kwong, and Carnahan-Starling by generalizing the fluid-fluid/fluid-solid force terms while maintaining the stability of the simulation. This results in increase of the density ratio to around 2 000, and provides a physics based multiphase simulation methodology to understand the air/water or water vapor/liquid water systems inside HFCs. Our generalization of density ratio, given in the thesis now makes LBM to be most promising CFD tools since it incorporates local thermodynamic consistencies in transport phenomena.

- In Chapter 5, we further investigate the effect of temperature changes inside the GDL and in HFC systems on the multiphase condensation and movement & behavior of resultant liquid water. We provide a novel and easy methodology to "mimic" the temperature changes in porous media via temperature dependent fluid-fluid/fluid-solid interaction forces along the system. This results in the system behavior similar to the incorporation of temperature without the additional instabilities. Our results of temperature mimicking induced condensation of water vapor to liquid water in a microchannel agree very well with phenomenological models

and experimental data in literature. For the first time, we were able to physically understand the thermoosmotic/thermocapillary phenomena that occurs in porous media: we found that depending on the hydrophilicity or hydrophobicity of the porous media, the flow of condensed water changes from hot to cold regions or cold to hot regions, respectively. This phenomenon has only been observed recently, and is not numerically resolved yet. We also develop a parallel thermal LBM code and couple this with the multiphase LBM mentioned earlier. Using Cahn-Hilliard theory, the additional forcing term arising from the surface tension gradient of liquid water depending on the calculated temperature at a local point is added. We perform a simple case study of liquid droplet movement on a microchannel substrate induced by temperature changes in the system.

6.2 Recommendations for Future Work

We have demonstrated our generalized LBM scheme that serves as a centerpiece to provide a future roadmap for hybridizing atomistic/molecular input (bottom level) and continuum levels to design complex systems via the middle-out approach in multiscale modeling, which is more efficient holistic integration modeling than conventional bottom-to-top or top-to-bottom approaches. This point was addressed in HFC systems and we are currently exploring this efficient methodologies to be applied in nanotechnology for sustainable systems, including water purification and nano/micro electromechanical systems. In the following

subsections, we describe our recommendations for achieving these objectives and provide a general procedure for multiscale modeling.

6.2.1 Hybridizing Atomistic/Molecular and LBM Schemes

Until now, we have mainly utilized mesoscale level models as the basis in our middle-out multiscale methodology. In the future, the molecular scale united atom model molecular dynamics (MD) structures will be further combined to the mesoscale level modeling of "pseudo particles". Use of the Langevin equation at the molecular scale will serve as the basis for the mesoscopic Boltzmann transport equation that will ultimately lead to a LBM suitable for numerical simulation. With a coupled method, the additionally accuracy of MD can be gained in the near-wall regions, while the LBM schemes allow for larger timesteps to be able to simulate the flow in complex structures involving multiphysical interactions a finite amount of time.

One can begin combining MD with LBM via simulating the most simplest of flow example: Poiseuille flow in a straight channel and can compare the hybdridized solution with to continuum Navier-Stokes (NS). MD can be utilized for better resolution of flow near the walls, while LBM can be used for bulk flow simulation. Simple potential expressions including the Lennard Jones potential ignoring attractive forces can be used for the molecules interactions with the wall, and the interaction strength can be fitted according to the phenomenological boundary conditions such as the no-slip boundary condition. At the interface of the LBM and MD regions, a buffer zone is established where forces and velocity at each time step of LBM. The MD simulation would be performed for multiple

time steps for each LBM time step, and the forces and velocities calculated in MD will be averaged to be exchanged to LBM. LBM will in turn provide the boundary conditions for MD ensembles, which would mean that the pressure at the top LBM/MD boundary will be exchanged. Methods such as ROM could also be advantageous due to its ability to represent a complex subcomponent model in terms of only its boundary information. Thus, integration of various HFC subcomponent models with this methodology will provide a rigorous test of our multiscale modeling framework.

6.2.2 Extended Applications for Multiscale Models

In the future we will extend this general multiscale methodology of the middle-out approach which can be applied to a broad spectrum of engineering systems. The middle-out approach will be used in investigating engineering problems in the areas of nanotechnology convergence in the sustainable energy-water nexus. Water purification via membrane distillation process is chosen as the benchmark example, which has great potential to be used in a broad range of applications including power, petrochemicals, oil & gas, as well as salt water distillation. The membrane distillation performance will be rigorously simulated via seamlessly integrating atomistic/molecular/meso/macro time and length scales and hybridizing with optimization methodologies. Unlike conventional models that simplify the porous structure, leading to overestimates of the performance, our novel contribution based on LBM scheme provides accurate design criteria for MD material selection including porosity, thermal conductivity & diffusivity, pore size, and thickness. Furthermore, by combining optimization tools with a

complete multiscale approach, we can provide molecular design criteria of the key parameters such as the omniphobicity of the membrane distillation material that allows maximum flux in the membrane. In addition, we can use inverse approaches for prediction of new molecularly architectured materials which actively prevent fouling and scaling and can be used in a wide range of water chemistries, as well as temperatures and pressures. The resulting multiscale framework will provide a ground-breaking and versatile design tool that can reduce immense time and monetary resources spent in experimentally identifying the optimal materials at the molecular level.

References

[1] M.C. Roco, C.A. Mirkin, M.C. Hersam, "Nanotechnology research directions for societal needs in 2020," Springer, Berlin (2010)

[2] M. Horstemeyer, "Multiscale modeling: A Review," *Practical Aspects of Computational Chemistry*, **87** (2010)

[3] P.S. Chung, D.S. So, L.T. Biegler, and M.S. Jhon, "Nanotechnology convergence and modeling paradigm of sustainable energy system using polymer electrolyte membrane fuel cell as a benchmark example," *Journal of Nanoparticle Research*, **14,** 853 (2012)

[4] S. Chen and G. Doolen, "Lattice Boltzmann method for fluid flows," *Ann. Rev. Fluid Mech.*, **30**, 329 (1998).

[5] Z. Shi, J. Zhang, Z.S. Liu, H. Wang, and D.P. Wilkinson, "Current status of ab initio quantum chemistry study for oxygen electroreduction on fuel cell catalysts," *Electrochimica Acta*, **51**, 10 (2006)

[6] R. Devanathan, "Recent developments in proton exchange membranes for fuel cells," *Energy and Environmental Science,* **1**, 101 (2008)

[7] Web of Knowledge® Citation Reports http://apps.webofknowledge.com/UA_GeneralSearch_input.do?product=UA&search_mode=GeneralSearch&SID=4D1Hr1gV69AkJY74gUC&preferencesSaved=

[8] P.S. Chung, D.S. So, L.T. Biegler, and M.S. Jhon, "Nanotechnology convergence and modeling paradigm of sustainable energy system using

polymer electrolyte membrane fuel cell as a benchmark example," *Journal of Nanotechnology Research,* **14**, 8 (2012)

[9] C.Y. Wang, "Fundamental models for fuel cell engineering," *Chemical Reviews*, **104**, 10, 4727 (2004)

[10] B. Todd, and J.B. Young, "Thermodynamic and transport properties of gases for use in solid oxide fuel cell modeling," *Journal of Power Sources*, **110**, 186 (2002)

[11] H. Meng, and C.Y. Wang, "Electron transport in PEFCs," *Journal of The Electrochemical Society*, **151**, A358 (2004).

[12] H. Meng, and C.Y. Wang, " Large-scale simulation of polymer electrolyte fuel cells by parallel computing," *Chemical Engineering Sciences*, **59**, 3331 (2004)

[13] A.A. Franco, P. Schott, C. Jallut, and B.M. Maschke, "A multiscale dynamic mechanistic model for transient analysis of electrochemical cells," Presentation in Symposium "T1: Modeling of Electrochemical Systems" *207th Meeting of the Electrochemical Society* (2005)

[14] D. Eberard, L. Lefèvre, and B.M. Maschke, "Multiscale coupling in heterogeneous diffusion processes: a port-based approach," *Proceedings of the International Conference Physics and Control,* (2005)

[15] A.A. Franco, P.Schott, C. Jallut, and B. Maschke, "A dynamic mechanistic model of an electrochemical interface," *Journal of the Electrochemical Society*, **153** (6) A1053 (2006).

[16] A.A. Franco, P.Schott, C. Jallut, and B. Maschke, "A multiscale dynamic model of a PEFC electrode," Presentation in the *Proceedings of the JDMACS* 2005

[17] S. Chen and G. Doolen, "Lattice Boltzmann method for fluid flows," *Annual Reviews of Fluid Mechanics,* **30**, 329 (1998).

[18] U. Frisch, B. Hasslacher, Y. Pomeau, "Lattice-gas automata for the Navier-Stokes equation," *Physical Review Letters,* **56**, 1505 (1986).

[19] H. Chen, S. Chen, and W. Matthaeus, "Recovery of the Navier-Stokes equations using a lattice-gas Boltzmann method," *Physical Review E*, **45**, 5339 (1992).

[20] T. Aoyagi, J. Takimoto, and M. Doi, "Molecular dynamics study of polymer melt confined between walls," *Journal of Chemical Physics,* **115,** 552 (2001).

[21] M.S. Jhon, G. Sekhon, and R. Armstrong, "The response of polymer molecules in a flow," *Advances in Chemical Physics*, **66**, 153 (1987).

[22] R.J. Waltman, D.J. Pocker, and G.W. Tyndall, "Studies on the interactions between ZDOL perfluoropolyether lubricant and the carbon overcoat of rigid magnetic media," *Tribology Letters* **4**, 267 (1998)

[23] W. Goddard III, B. Merinov, A van Duin, T. Jacon, M. Blanco, V. Molinero, S.S. Jang, Y.H Jang, "Multi-paradigm multi-scale simulations for fuel cell catalysts and membranes," *Molecular Simulation*, **32**, 251 (2006)

[24] J.M. Seminario, "Calculation of intramolecular force fields from second-derivative tensors," *International Journal of Quantum Chemistry* **60**, 1271 (1996).

[25] E. Anderson, Z. Bai, C. Bischof, S. Blackford, J. Demmel, J. Dongarra, J. Du Croz, A. Greenbaum, S. Hammarling, A. McKenney, and D.Sorensen, *LAPACK Users' Guide*, SIAM, Philadelphia, (1999).

[26] R. M. Balabin, "Is quantum chemical treatment of biopolymers accurate? Intramolecular basis set superposition error (BSSE), " *Journal of Chemical Physics* **132**, 211103 (2010).

[27] Laio, J.V. Vondele , U. Rothlisberger "A Hamiltonian electrostatic coupling scheme for hybrid car-parrinello simulations," *Journal Chemical Physics,* **116**, 6941 (2002)

[28] G. Csanyi, T. Albaret, M.C. Payne MC, and A. De Vita "A ''Learn on the fly'': a hybrid classical and quantum-mechanical molecular dynamics simulation," *Physical Review Letters*, **93** 175503 (2004)

[29] Q. Sun and R. Faller, "Systematic coarse-graining of atomistic models for simulation of polymeric systems," *Computers & Chemical Engineering*, **29**, 2380 (2005)

[30] R. Faller, "Automatic coarse graining of polymers," *Polymer,* **45**, 3869 (2005)

[31] D.-Buscalioni and P.V. Coveney "Continuum-particle hybrid coupling for mass, momentum, and energy transfers in unsteady fluid flow" *Physical Review E* , **67** (2003)

[32] JQ Broughton, F.F Abraham , N. Bernstein, and E. Kaxiras, "Concurrent coupling of length scales: methodology and application" *Physical Review B* **60**, 2391(1999)

[33] H, Rafii-Tabar, L. Hua, and M. Cross "A multi-scale atomistic-continuum modeling of crack propagation in a two-dimensional macroscopic plate," *Journal Physics: Condensed Matter*, **10**, 2375 (1998)

[34] J.A. Smirnova, L.V. Zhigilei, and B.J. Garrison BJ, "A combined molecular dynamics and finite element method technique applied to laser induced pressure wave propagation," *Computer Physics Communications* **118**, 11 (1999)

[35] S.T. O'Connell and P.A. Thompson, "Molecular dynamics– continuum hybrid computations: a tool for studying complex fluid flows" *Physical Review E*, **52**, R5792 (1995)

[36] N.G. Hadjiconstantinou, "Combining atomistic and continuum simulations of contact-line motion," *Physical Review E,* **59**, 2475 (1999)

[37] M. Neri, C. Anselmi, M. Cascella, A. Maritan, and P. Carloni , "Coarse-grained model of proteins incorporating atomistic detail of the active site," *Physical Review Letters,* **95**, 21 (2005)

[38] E. Villa, A. Balaeff, L. Mahadevan, and K. Schulten , "Multiscale method for simulating protein-DNA complexes," *Multiscale Modeling and Simulation,* **2**, 527 (2004)

[39] J. Li, D. Liao, and S. Yip, "Coupling continuum to molecular dynamics simulation: reflecting particle method and the field estimator," *Physical Review E,* **57**, 7259 (1998)

[40] E.G. Flekkoy and G. Wagner, "Feder J Hybrid model for combined particle and continuum dynamics," *Europhysics Letters,* **52**, 271 (2000)

[41] S. Chen, H. Chen, D. Martinez, and W. Matthaeus, "Lattice Boltzmann model for simulation of magnetohydrodynamics," *Physical Review Letters,* **67**, 3776 (1991).

[42] Y. Qian, D. d'Humieres, and P. Lallemand, "Lattice BGK models for Navier-Stokes equation," *Europhysics Letters,* **17**, 479 (1992).

[43] T. Kataoka and M. Tsutahara, "Lattice Boltzmann model for the compressible Navier-Stokes equations with flexible specific-heat ratio," *Physical Review E,* **69**, AR 035701 (2004).

[44] S. Hou and Q. Zou, "Simulation of cavity flow by the lattice Boltzmann method," *Journal of Computational Physics,* **118**, 329 (1995).

[45] S. Chen and G. Doolen, "Lattice Boltzmann method for fluid flows," *Annual Reviews of Fluid Mechanics,* **30**, 329 (1998).

[46] International Conference for Mesoscopic Methods in Engineering and Science (ICMMES), June 16-20, 2008, Amsterdam, Netherlands.

[47] 17th International Conference on the Discrete Simulation of Fluid Dynamics (DSFD), August 4-8, 2008, Florianolis, Brazil.

[48] R. Liboff, Kinetic theory: Classical, quantum, and relativistic descriptions, 2nd edition, John Wiley & Sons, New York, NY (1998).

[49] P. L. Bhatnagar, E. P. Gross, and M. Krook, "A model for collision processes in gases. I. Small amplitude processes in charged and neutral one-component system," *Physical Review A,* **94**, 511 (1954).

[50] M.S. Jhon and D. Forster, "A kinetic theory of classical simple liquids," *Physical Review A,* **12**(1), 254 (1975).

[51] M.S. Jhon, J.S. Dahler, and R.C. Desai, "A theory of the liquid-vapor interface," *Advances in Chemical Physics*, **46**, 279 (1981).

[52] M.S. Jhon, P.R. Peck, R.F. Simmons, and T.J. Janstrom, "Behavior of the head-disk interface in future disk drives," *IEEE Transactions in Magnetics*, **30** (2), p. 410 (1994).

[53] M.S. Jhon and J.S. Dahler, "A kinetic theory of dense fluids: test-particle kinetic equation," *Journal of Chemical Physics*, **74**, 2477 (1981).

[54] U. Frisch, B. Hasslacher, and Y. Pomeau, "Lattice-gas automata for the Navier-Stokes equation," *Physical Review Letters,* **56**, 1505 (1986).

[55] U. Frisch, D. d'Humieres, B. Hasslacher, P. Lallemand, Y. Pomeau, and J.-P. Rivet, "Lattice gas hydrodynamics in two and three dimensions," *Complex Systems,* **1**, 649 (1987).

[56] S. Wolfram, "Cellular automaton fluids .1. basic theory," *Journal of Statistical Phys*ics, **45,** 471 (1986).

[57] H. Grad, "Note on N-dimensional hermite polynomials," *Communications on Pure and Applied Mathematics*, **2**, 325 (1949).

[58] X. Shan and X. He, "Discretiztion of the velocity space in the solution of the Boltzmann equation," *Physical Review Letters*, **80**, 65 (1998).

[59] H. Chen, S. Chen and W. Matthaeus, "Recovery of the Navier-Stokes equations using a lattice-gas Boltzmann method," *Physical Review E*, **45**, 5339 (1992).

[60] L.S. Luo and S.S. Girimaji, "Theory of the lattice Boltzmann method: Two-fluid model for binary mixtures," *Physical Review E*, **67**, (2003).

[61] X.Y. He, G.D. Doolen, and T. Clark, "Comparison of the lattice Boltzmann method and the artificial compressibility method for Navier-Stokes equations," *Journal of Computational Physics*, **179**, 439 (2002).

[62] H. Chen, C. Teixeira, and K. Molvig, "Realization of fluid boundary conditions via discrete Boltzmann dynamics," *Int. J. Mod. Phys.*, **9**(8), 1281 (1998).

[63] H. Chen, S. Kandasamy, S. Orszag, R. Shock, S. Succi, and V. Yahkot, "Extended Boltzmann kinetic equation for turbulent flows," *Science,* **301**, 633 (2003).

[64] D. P. Ziegler, "Boundary conditions for lattice Boltzmann simulations," *Journal of Statistical Physics,* **71**, 1171 (1993).

[65] Ginzbourg and P. M. Alder, "Boundary flow condition analysis for the three-dimensional lattice Boltzmann model," *Journal de Physique II,* **4**, 191 (1994).

[66] J. C. Ladd, "Numerical simulation of particular suspensions via a discretized Boltzmann equation. Part 2. Numerical results," *Journal of Fluid Mechacnics,* **271**, 311 (1994).

[67] D. R. Noble, S. Chen, J. G. Georgiadis, and R. O. Buckius, "A consistent hydrodynamic boundary condition for the lattice Boltzmann method," *Physics of Fluids,* **7**, 203 (1995).

[68] T. Inamuro, M. Yoshino, and F. Ogino, "A non-slip boundary condition for lattice Boltzmann simulations," *Physics of Fluids*, **7**, 2928 (1995).

[69] R. Maier, R. Bernard, and D. Grunau, "Boundary conditions for the lattice Boltzmann method," *Physics of Fluids,* **8**, 1788 (1996).

[70] Q. Zou and X. He, "On pressure and velocity boundary conditions for the lattice Boltzmann BGK model," *Physics of Fluids,* **9**, 1591 (1997).

[71] P. A. Skordos, "Initial and boundary conditions for the lattice Boltzmann method," *Physical Review E.*, **48**, 4823 (1992).

[72] S. Chen, D. Martinez, and R. Mei, "On boundary conditions in lattice Boltzmann methods," *Physics of Fluids,* **8**, 2527 (1996).

[73] D. R. Noble, J. Georgiadis, and R. Buckius, "Direct assessment of lattice Boltzmann hydrodynamics and boundary conditions for recirculating flows," *Journal of Statistical Physics,* **81**, 17 (1995).

[74] D. R. Noble, J. Georgiadis, and R. Buckius, "Comparison of accuracy and performance of lattice Boltzmann and finite difference simulations of steady viscous flow," *International Journal for Numerical Methods in Fluids,* **23**, 1 (1996).

[75] Ginzburg and D. d'Humieres, "Multireflection boundary conditions for lattice Boltzmann models," *Physical Review E*, **68**, (2003).

[76] M. A. Gallivan, D. R. Noble, J. G. Georgiadis, and R. O. Buckius, "An evaluation of the bounce-back boundary condition for lattice Boltzmann simulations," *International Journal for Numerical Methods in Fluids,* **25**, 249 (1997).

[77] D. Kandhai, A. Koponen, A. Hoekstra, M. Kataja, J. Timonen, and P. M. A. Sloot, "Implementation aspects of 3D lattice-BGK: Boundaries, accuracy, and a new fast relaxation method," *Journal of Computational Physics*, **150**, 482 (1999).

[78] D. Kandhai, D. Vidal, A. Hoekstra, H. Hoefsloot, P. Iedema, and P. M. A. Sloot, "Lattice-Boltzmann and finite element simulations of fluid flow in a SMRX mixer," *International Journal for Numerical Methods in Fluids*, **31**, 1019 (1999).

[79] O. Filippova and D. Hanel, "Lattice-BGK model for low Mach number combustion," *International Journal of Modern Physics C*, **9**, 1439 (1998).

[80] O. Filippova and D. Hanel, "A novel lattice-BGK approach for low Mach number combustion," *Journal of Computational Physics*, **158**, 139 (2000).

[81] R. Mei, L.-S. Luo, and W. Shyy, "An accurate curved boundary treatment in the lattice Boltzmann method," *Journal of Computational Physics,* **155**, 307 (1999).

[82] M. Bouzidi, M. dFirdaouss, P. Lallemand, "Momentum transfer of a lattice Boltzmann fluid with boundaries," *Physics of Fluids*, **13**, 3452 (2001).

[83] X. He, Q. Zou, L.-S. Luo, and M. Dembo, "Analytic solutions and analysis on non-slip boundary condition for the lattice Boltzmann BGK model," *Journal of Statistical Physics.*, **87**, 115 (1997).

[84] O. Behrend, "Solid boundaries in particle suspension simulations via lattice Boltzmann method," *Physical Review E,* **52**, 1164 (1995).

[85] L.-S. Luo, "Analytic solutions of linearized lattice Boltzmann equation for simple flows," *Journal of Statistical Physics,* **88**, 913 (1997).

[86] X. He, L.-S. Luo, and M. Dembo, "Some progress in lattice Boltzmann method. Part I. Nonuniform mesh grids," *Journal of Computational Physics,* **129**, 357 (1996).

[87] X. He, L.-S. Luo, and M. Dembo, "Some progress in lattice Boltzmann method: High Reynolds mesh grids," *Journal of Physics A,* **239**, 276 (1997).

[88] X. He and L.-S. Luo, "*A priori* derivation of the lattice Boltzmann equation," *Physical Review E,* **55**, R6333 (1997).

[89] X. He and G. Doolen, "Lattice Boltzmann method on curvilinear coordinates system: Flow around a circular cylinder," *Journal of Computational Physics,* **134**, 306 (1997).

[90] R. Mei and W. Shyy, "On the finite difference-based lattice Boltzmann method in curvilinear coordinates," *Journal of Computational Physics,* **143**, 426 (1998).

[91] Ginzbourg and D. d'Humieres, "Local second-order boundary methods for lattice Boltzmann models," *Journal of Statistical Physics,* **84**, 927 (1996).

[92] O. Filippova and D. Hanel, "Grid refinement for lattice-BGK models," *Journal of Computational Physics,* **147**, 219 (1998).

[93] F. P. Preparata and S. Shamos, "Computational geometry, an introduction," Springer-Verlag (Berlin), 1985.

[94] Y. E. Kalay, "Determining the spatial containment of a point in general polyhedra," *Computer Graphics and Image Processing*, **19**, 203 (1982).

[95] J. Lane, B. Magedson, and M. N. Rarick, "An efficient point in polyhedron algorithm," *Computer Vision, Graphics and Image Processing*, **26**, 118 (1984).

[96] W. Horn and D. L. Taylor, "A theorem to determine the spatial containment of a point in a planar polyhedron," *Computer Vision, Graphics and Image Processing*, **45**, 106 (1989).

[97] F. Feito, J. Torres, and A. Urena, "Orientation, simplicity and inclusion test for planar polygons," *Computers & Graphics*, **19**, 595 (1995).

[98] F. Feito, "Solid modeling and graphics objects algebra," PhD Dissertation, Department of Lenguajey Sistemas Informaticos, University of Granada, 1995.

[99] F. Feito and J. Torres, "Inclusion test for general polyhedra," *Computers & Graphics*, **21**, 23 (1997).

[100] M. Berger, "Geometry I," Springer-Verlag (Berlin), 1987.

[101] M. Schafer and S. Turek, "Benchmark computations of laminar fow over a cylinder", *Notes in Numerical Fluid Mechanics*, **52**, 547 (1996).

[102] D. Yu, R. Mei, and W. Shyy, "A multi-block lattice Boltzmann method for viscous fluid flows", *International Journal for Numerical Methods in Fluids*, **39**, 99 (2002)

[103] O. Filippova and D. Hanel, "Grid refinement for Lattice-BGK Models", *Journal of Computational Physics*, **147**, 219 (1998)

[104] D. A. Lyn, S. Einav, W. Rodi, and J.-H. Park, "A laser-Doppler-velocimetry study of ensemble-averaged characteristics of the turbulent near wake of a square cylinder," *Journal of Fluid Mechanics*, **304**, 285 (1995).

[105] ERCOFTAC. Test case LES2: Flow past a long square cylinder. http://www.ercoftac.org, (1997).

[106] S. Geller, M. Krafczyk, J. Toelke, S. Turek, and J. Hron, "Benchmark computations based on lattice-Boltzmann, finite element and finite volume methods for laminar flows," *Computers & Fluids*, **35**, 888 (2006).

[107] W. Rodi, J. H. Ferziger, M. Breuer, and M. Pourqui´e, "Status of large eddy simulation: Results of a workshop," *Transactions in ASME*, **119**, 248 (1997).

[108] R. Martinuzzi, Ph.D. dissertation, University of Erlangen, Germany (1992).

[109] G. Falcone, G.F. Hewitt , C. Alimonti , and B. Harrison, "Multiphase Flow Metering: Current Trends and Future Developments," *Journal of Petroleum Technology*, **54**, 4 (2013)

[110] M.R. Swift, W.R. Osborn, and J.M. Yeomans, "Lattice Boltzmann simulation of non-ideal fluids," *Physical Review Letters*, **75,** 830 (1995).

[111] M. R. Swift, E. Orlandini, W. R. Osborn, and J. M. Yeomans, "Lattice Boltzmann simulations of liquid-gas and binary fluid systems," *Physical Review E*, **54**, 5041(1996).

[112] N. Takada, M. Misawa, A. Tomiyama, and S. Fujiwara, "Numerical simulation of two- and three-dimensional two-phase fluid motion by lattice Boltzmann method," *Computer Physics Communications.*, **129**, 233 (2000).

[113] P. Raiskinmaki, A. Koponen, J. Merikoski, and J. Timonen, "Spreading dynamics of three-dimensional droplets by the lattice-Boltzmann method," *Computational Material Science,* **18,** 7 (2000).

[114] X. Shan and H. Chen, "Lattice Boltzmann model for simulating flows with multiple phases and components," *Physical Review E*, **47**, 1815 (1993).

[115] X. He, S. Chen, and R. Zhang, "A lattice Boltzmann scheme for incompressible multiphase flow and its application in simulation of Rayleigh–Taylor instability," *Journal of Computational Physics*, **152**, 642 (1999).

[116] X. He and G.D. Doolen, "Thermodynamic foundations of kinetic theory and lattice Boltzmann models for multiphase flows," *Journal of Statistical Physics.*, **107**, 309 (2002).

[117] S. Hou, X. Shan, Q. Zou, G.D. Doolen, and W.E. Soll, "Evaluation of two lattice Boltzmann models for multiphase flows," *Journal of Computational Physics*, **138**, 695 (1997).

[118] D. Grunau, S. Chen, and K. Eggert, "A lattice Boltzmann model for multiphase fluid flows," *Physics of Fluids A*, **5**, 2557 (1993)

[119] J.C. Desplat, I, Pagonabarraga, and P. Bladon, "A parallel lattice-Boltzmann code for complex fluids," *Computer Physics Communications*, **134**, 273 (2001).

[120] J. Briant, P. Papatzacos, and J.M. Yeomans, "Lattice Boltzmann simulations of contact line motion in a liquid-gas system," *Philosophical Transactions of the Royal Society A*, **360**, 485 (2002).

[121] J.W. Cahn, "Critical Point Wetting," *The Journal of Chemical Physics*, **66**, 3667 (1977).

[122] H.W. Zheng, C. Shu, Y.T. Chew, and J.H. Sun, "Three-dimensional lattice Boltzmann interface capturing method for incompressible flows," *International Journal for Numerical Methods in Fluids*, **56**, 1653 (2008).

[123] D. Jacqmin, "Calculation of two-phase Navier–Stokes flows using phase-field modeling," *Journal of Computational Physics*, **155**, 96 (1999)

[124] D.H. Rothman and J.M. Keller, "Immiscible cellular-automaton fluids," *Journal of Statistical Physics*, **52,** 1119 (1988).

[125] M. Sussman, E. Fatemi, P. Smereka, and S. Osher, "An improved level set method for incompressible two-phase flows," *Computers & Fluids*, **27,** 663 (1998).

[126] M. R. Swift, E. Orlandini, W. R. Osborn, and J. M. Yeomans, "Lattice Boltzmann simulations of liquid-gas and binary fluid systems," *Physical Review E*, **54**, 5041(1996).

[127] Q. Kang, D. Zhang, and S. Chen, "Displacement of a two-dimensional immiscible droplet in a channel," *Physics of Fluids*, **14**, 3203 (2002).

[128] X. Shan and H. Chen, "Simulation of non-ideal gases and liquid–gas phase transitions by the lattice Boltzmann equation," *Physical Review E*, **49**, 2941 (1994).

[129] P.L. Bhatnagar, E.P. Gross, M. Krook. "A Model for Collision Processes in Gases. I. Small Amplitude Processes in Charged and Neutral One-Component Systems". *Physical Review,* **94**, 3, 511 (1954)

[130] H. Chen, S. Chen and W. Matthaeus, "Recovery of the Navier-Stokes equations using a lattice-gas Boltzmann method," *Physical Review E*, **45**, 5339 (1992).

[131] X. He and G.D. Doolen, "Thermodynamic foundations of kinetic theory and lattice Boltzmann models for multiphase flows," *Journal of Statistical Physics*, **107**, 309 (2002)

[132] M. Sukop and D. Or, "Lattice Boltzmann method for modeling liquid-vapor interface configurations in porous media," *Water Resource Research*, **40**, W01509 (2004).

[133] R. Mukundan, Y. S. Kim, F. Garzon, and B. Pivovar, *ECS Transactions*, **1**, (2006).

[134] F. Garzon, Y. S. Kim, M. Rangachary, and B. Pivovar, DOE Hydrogen Program Review, Crystal City, VA, May 16–19, 2006,

[135] Y. Wang, "Analysis of the key parameters in the cold start of polymer electrolyte fuel cells," *Journal of the Electrochemical Society*, **154**, B1041 (2007).

[136] S. Kim and M. M. Mench, "Physical degradation of membrane electrode assemblies undergoing freeze/thaw cycling: Micro-structure effects," *Journal of Power Sources*, **174**, 206 (2007)

[137] S. He, S. H. Kim, and M. M. Mench, "Validated Leverett approach for multiphase flow in PEFC diffusion media I. Hydrophobicity effect," *Journal of the Electrochemical Society*, **154**, B1024 (2007)

[138] M. M. Mench, C.Y. Wang, and M. Ishikawa, "In situ current distribution measurements in polymer electrolyte fuel cells," *Journal of the Electrochemical Society*, **154**, B1227 (2007)

[139] S. He and M. M. Mench, "Liquid water storage, distribution, and removal from diffusion media in PEFCS," *J. Electrochem. Soc.*, **153**, A1724 (2006)

[140] M. Khandelwal, S. Lee, and M. M. Mench, "Direct measurement of through-plane thermal conductivity and contact resistance in fuel cell materials," *Journal of Power Sources*, **172**, 816 (2007).

[141] M. Khandelwal, J. J. Ko, and M. M. Mench, "An integrated modeling approach for temperature driven water transport in a polymer electrolyte fuel cell stack after shutdown," *ECS Transactions*, **11**, 553 (2007).

[142] M. Tasaka, T. Suzuki, R. Kiyono, M. Hamada, and K. Yoshie, "Thermoosmosis and transported entropy of water across poly(4-vinylpyridine/styrene) and poly(N-vinyl-2-methylimidazole/styrene) type membranes in electrolyte solutions," *Journal of Physical Chemistry*, **100**, 16361 (1996)

[143] M. Khandelwal, S. Lee, and M.M. Mench, "Model to predict temperature and capillary pressure driven water transport in PEFCs after shutdown," *Journal of The Electrochemical Society,* **156** , 6, (2009)

[144] M. Tasaka, T. Mizuta, and O. Sekiguchi, "Mass transfer through polymer membranes due to a temperature gradient," *Journal of Membrane Science*, **54**, 191 (1990).

[145] J. P. G. Villaluenga, B. Seoane, V. M. Barragan, and C. Ruiz-Bauza, "Thermo-osmosis of mixtures of water and methanol through a Nafion membrane," *Journal of Membrane Science*, **274**, 116 (2006).

[146] M.F. Schatz, and G.P. Neitzel, "Experiments on thermocapillary instabilities," *Annual Review of Fluid Mechanics,* **33**, 93 (2001)

[147] M. Tasaka, T. Hirai, R. Kiyono, and Y. Aki, "Solvent transoport across cation-exchange membranes under a temperature difference and under an osmotic pressure difference," *Journal of Membrane Science*, **71**, 151 (1992).

[148] R. Bradean, H. Haas, K. Eggen, C. Richards, and T. Vrba, "Stack models and designs for improving fuel cell startup from freezing temperatures,," *ECS Transactions*, **3**, 1159 (2006).

[149] F. Massaioli, R. Benzi, and S. Succi, Exponential tails in two-dimensional Rayleigh–Benard convection, *Europhysics Letters,* **21** 305 (1993)

[150] C. Bartoloni, S. Battista, P.S. Cabasino, J. Paolucci, R. Pech, G.M. Todesco, M. Torelli, W. Tross, P. Vicini, R. Benzi, N. Cabibbo, F. Massaioli, and R. Tripiccione, "LBE simulations of Rayleigh–Benard

convection on the APE100 parallel processor," *International Journal of Modern Physics C*, **4**, 993 (1993).

[151] L.S. Luo, "Unified theory of the lattice Boltzmann models for nonideal gases," *Physics Review Letters*, **81**, 1618 (2008)

[152] F. Alexanders, S. Chen, and J. Sterling, "Lattice Boltzmann thermo-hydrodynamics," *Physical Review E*, **47**, R2249 (2003)

[153] Y. Chen, H. Ohashi, and M. Akiyama, Two-parameter thermal lattice BGK model with a controllable Prandtl number, *Journal of Scientific Computing*, **12**, 169 (2007)

[154] C. Teixeira, H. Chen, and D. Freed, "Multi-speed thermal lattice Boltzmann method stabilization via equilibrium under-relaxation," *Computer Physics Communications*, **129**, 207 (2000)

[155] X. He, S. Chen, and G.D. Doolen, "A novel thermal model for the lattice Boltzmann method in incompressible limit," *Journal of Computational Physics*, **146**, 282 (2008)

[156] X. Shan, "Solution of Rayleigh–Benard convection using a lattice Boltzmann method," *Physical Review E*, **55**, 2780 (2007)

[157] H. Liu, A. J. Valocchi, Y. Zhang, and Q. Kang, "Lattice Boltzmann phase-field modeling of thermocapillary flows in a confined microchannel," *Journal of Computational Physics*, **256**, 334 (2014).

Appendix A

IEEE TRANSACTIONS ON MAGNETICS, VOL. 48, NO. 11, NOVEMBER 2012

Perfluoropolyether Lubricant Interactions With Novel Overcoat via Coarse-Grained Molecular Dynamics

Sesha Hari Vemuri[2], Pil Seung Chung[1], Robert Smith[2], Geun-Young Yeom[2], Young In Jhon[2], Nae-Eung Lee[2], Lorenz T. Biegler[1], and Myung S. Jhon[1,2]

[1]Department of Chemical Engineering and Data Storage Systems Centers, Carnegie Mellon University, Pittsburgh, PA 15213 USA

[2]School of Advanced Materials Science and Engineering, Sungkyunkwan University, Suwon, 440-746 Korea

In this paper, we investigated physiochemical properties of new lubricant candidates for head-disk interface through various perfluoropolyether lubricant films on diamond, diamond-like carbon, and graphene overcoat surfaces via large scale coarse-grained bead–spring molecular dynamics stemming from the atomistic theory. Lubricant film conformations were characterized by investigating perpendicular component of molecular conformation, which determines the thickness of monolayer lubricant film. The distribution of functional endgroups and the mobility were analyzed via self-diffusion process. Here, we illustrate the effects of endgroup structure and carbon-surface structure on the film conformation and the mobility by expanding the multiscale simulation methodology and select candidates for future HDI design.

Index Terms—**Graphene, head-disk interface, lubricant film, molecular dynamics, multiscale, perfluoropolyether.**

I. Introduction

INTRODUCING graphene as a novel carbon-overcoat opens a new paradigm for high areal density in hard disk drives (HDDs) by reducing head-media spacing (HMS) to 3.4 nm, which is less than half of the conventional HMS and will provide up to six times the current recording capacity (see Fig. 1) [1]. Along with the development of new lubricant materials, the head-disk interface (HDI) in HDD systems can be achieved via combinations of lubricants and novel architecture of carbon overcoat systems. Hence, we applied a coarse-graining method bridging atomistic and molecular/mesoscale models, which provides the accurate potential energy forms and parameters enabling the novel system designs [2], [3]. By using the force field calculation based on first principles (e.g., ab initio), intramolecular and intermolecular interaction energies of various perfluoropolyethers (PFPEs) were estimated [4], [5] for inputs to molecular dynamics.

In this paper, we investigated and compared physiochemical properties of various perfluoropolyether lubricant films on diamond, diamond-like carbon (DLC), and graphene via large scale coarse-grained, bead-spring molecular dynamics (CGMD) based on the endgroup-surface potential energy parameters determined from atomistic theory. Intermolecular force fields between PFPEs and carbon overcoats were estimated from the equilibrium geometries of truncated PFPEs (endgroup) and the segments of the overcoat materials. By using CGMD, lubricant film conformations were characterized by anisotropic radius of gyration where the perpendicular component determines the thickness of the lubricant film. The mobility of PFPE molecules was investigated via self-diffusion. The focus of this multiscale combinatorial problems is on: 1) observing the effects of endgroup's chemical structure on the film conformation and the mobility; 2) structural effects of carbon surface, which may provide selection criteria for materials in future HDIs; and 3) expanding the feasibility of multiscale simulation methodology, which we have developed thus far. Here, we found the relationships of endgroup-endgroup and endgroup-surface interactions on the agglomeration and the PFPE mobility. By examining the properties as a function of endgroup-surface functionality, one could tailor PFPE film-surface interactions by tuning the overcoat surface.

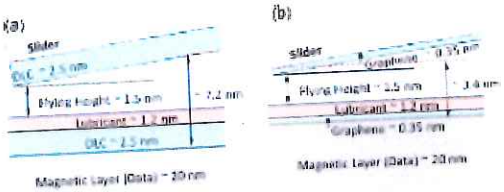

Fig. 1. HMS of head-disk interface with (a) DLC and (b) graphene overcoats.

II. Coarse-Grained Molecular Dynamics

In our previous research [6]–[8], PFPE molecules were characterized via a coarse-grained, bead-spring model, which simplifies the detailed atomistic structures by categorizing groups of atoms with uniform bead size for backbone and endgroup based on the dimension of the oligomer. This approach, nevertheless, retains the essence of molecular structure and chain flexibility. To implement the atomistic level theory in our previous MD models, we applied a coarse-graining procedure linking atomistic potentials and molecular/mesoscale simulations combining the parameters obtained from quantum mechanical calculation, as illustrated in Fig. 2. Our reduced order model (ROM) [9], [10] was introduced to optimize the force field parameters for the coarse-grained level models

Manuscript received March 02, 2012; revised April 17, 2012; accepted April 20, 2012. Date of current version October 19, 2012. Corresponding author: M. S. Jhon (e-mail: mj3a@andrew.cmu.edu)

Color versions of one or more of the figures in this paper are available online at http://ieeexplore.ieee.org

Digital Object Identifier 10.1109/TMAG.2012.2200456

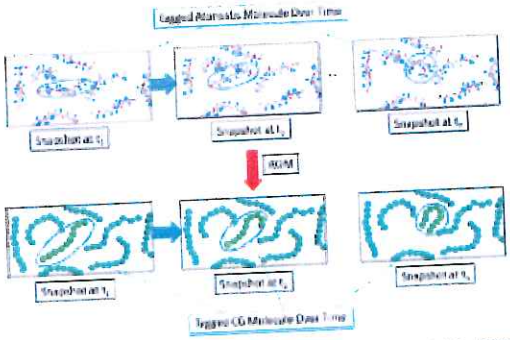

Fig. 2. Illustration of coarse-graining procedure by using ROM for PFPE molecular systems.

TABLE I
BONDING PARAMETERS (FENE) FOR COARSE-GRAINED MD MODEL, WHERE k AND R_0 REPRESENT THE STRETCHING BOND CONSTANT (kcal/(mol · Å²)) AND THE EQUILIBRIUM BOND LENGTH (Å) (BOND1: BACKBONE-BACKBONE AND BOND2: BACKBONE-ENDGROUP)

	k	R_0
Bond1	43.7	2.524
Bond2	58.3	2.332

allowing for lubricant oligomer chain dynamics and flexibility compatible to the fully atomistic simulations.

The method focuses on transferring the distribution of structural parameters from the atomistic to the coarse-grained model. The procedure involves performing an atomistic MD simulation of a bulk PFPE system and calculating the equilibrium probability distributions. A Boltzmann distribution for bond lengths is fit to the distribution determined from the MD simulation by varying the parameters of the bonded potential

$$P(r) \propto \exp\left(-U_b(r)/k_B T\right), \tag{1}$$

Here, P is the probability distribution, U_b is the bond potential, k_B is Boltzmann constant, and T is absolute temperature. Intramolecular (bonding) parameters for coarse-grained model are listed in Table I.

An ideal flat and smooth surface was used to model the carbon overcoat with the dissipative dynamics by Langevin equation. The force field was constructed by the Lennard Jones (LJ) and finitely extensible nonlinear elastic (FENE) model for the intramolecular interaction and connected beads [11]. Short-range exponential potentials (EXP) for the interactions among the functional endgroups and between functional endgroups and carbon surface were introduced as follows [8]:

$$U_{\mathrm{EXP}}(r) = -\varepsilon_p \exp(-r/d) \tag{2}$$

where ε_p is endgroup functionality and d is the equilibrium distance. ε_p characterizes the interactions between PFPE and overcoat (see Table II) and among PFPEs (see Table III). The governing equations in this simulation are represented by a set of Langevin equations [12].

TABLE II
ENDGROUP FUNCTIONALITY (ε_p) OF ZDOL, ZTETRAOL, AND DDPA ON DIAMOND, DLC, AND GRAPHENE (kcal/mol)

Overcoat / PFPE	Diamond	DLC	Graphene
Zdol	−9.05	−24.9	−19.1
Ztetraol	−15.2	−30.1	−20.7
DDPA	−9.5	−18.1	−17.5

TABLE III
ENDGROUP FUNCTIONALITY (ε_{pp}) BETWEEN PFPES, I.E., ZDOL, ZTETRAOL, AND DDPA (kcal/mol)

PFPE / PFPE	Zdol	Ztetraol	DDPA
Zdol	−8.23	−8.51	1.25
Ztetraol	-	−14.1	−1.56
DDPA	-	-	0.95

By varying molecular structures and ε_p, atomistically architectured PFPEs are represented in this simulation. Monolayer films fully covered by PFPE molecules were investigated with the dimensions of simulation box in the x and y directions were $40\sigma \times 40\sigma$, where σ is the diameter of the bead. After the system equilibration, the simulations were performed for 40 000 τ with the time step of 0.005 τ, where τ is $\sigma(m/\varepsilon)^{0.5}$, ε is the well depth of LJ potential energy, and m is the mass of the bead. Periodic boundary conditions were applied in the x and y directions.

III. RESULTS AND DISCUSSION

From the CGMD simulations, we analyzed the molecular conformation and mobility of PFPE lubricants (Zdol, Ztetraol, and Demnum di-propyl amine (DDPA) with 2000 g/mol molecular weight) on the carbon-overcoats (diamond, DLC, and graphene) by estimating anisotropic radii of gyration and self-diffusion coefficients.

A. Molecular Conformation

The thickness of monolayer films fully covered by PFPE molecules is mainly controlled by the molecular conformation on the surface. The conformations of monolayers were investigated by analyzing the anisotropy ratio for radius of gyration decomposing parallel ($R_\parallel^n$) and perpendicular ($R_\perp^n$) components

$$(R^n)^2 = \frac{1}{N_m}\sum_{i=1}^{N_m}\left[(x_i - x_g)^2 + (y_i - y_g)^2 + (z_i - z_g)^2\right] = (R_x^n)^2 + (R_y^n)^2 + (R_z^n)^2 = 2\left(R_\parallel^n\right)^2 + (R_\perp^n)^2 \tag{3}$$

where, x_i, y_i, and z_i are the position of the bead and x_g, y_g, and z_g are the center of the mass of PFPE molecule.

As shown in the Table IV, all PFPEs (Zdol, Ztetraol, and DDPA) show flat conformation ($R_\perp^n/R_\parallel^n < 1$) on all carbon surfaces (diamond, DLC, and graphene). By comparing the endgroup functionalities listed on Tables II and III, Table V illustrates that the strength of interactions among endgroups

TABLE IV
THE RATIO OF PERPENDICULAR TO PARALLEL RADII OF GYRATION ($R_\perp^2/R_\parallel^2$) FOR ZDOL, ZTETRAOL, AND DDPA ON DIAMOND, DLC, AND GRAPHENE OVERCOAT SURFACES, RESPECTIVELY

Overcoat PFPE	Diamond	DLC	Graphene
Zdol	0.4906	0.5012	0.5029
Ztetraol	0.4257	0.4594	0.4629
DDPA	0.5364	0.5421	0.5547

TABLE V
THE PERPENDICULAR COMPONENT OF RADII OF GYRATION ($R_\perp^2$) FOR ZDOL, ZTETRAOL, AND DDPA ON DIAMOND, DLC, AND GRAPHENE SURFACES, RESPECTIVELY

Overcoat PFPE	Diamond	DLC	Graphene
Zdol	0.7026	0.7182	0.7136
Ztetraol	0.6492	0.7024	0.6951
DDPA	0.7415	0.7522	0.7523

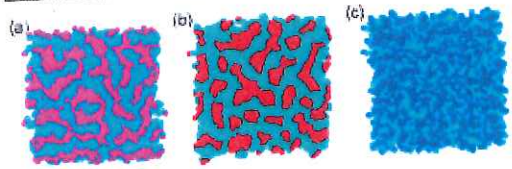

Fig. 3. Bottom view snapshots of (a) Zdol, (b) Ztetraol, and (c) DDPA on diamond overcoat surface. Light blue: backbone, pink: Zdol endgroup, red: Ztetraol endgroup, and blue: DDPA endgroup.

and surface barely affects the perpendicular molecular conformation as long as the total number of beads (i.e., molecular weight) remains constant. Especially, similar $R_\perp^2$ values of all cases, which mainly determines the film thickness in a monolayer lubricant system, indicates that intramolecular factors such as chain flexibility, molecular weight, or molecular structural complexity may affect film thickness and conformation more dominantly than intermolecular factors such as endgroup functionality or carbon-overcoat material.

Although our resulting statistical analysis of the molecular configurations away from the surface were the same for all PFPEs, we observed that the endgroup clusters on the surface varied. Fig. 3 shows the bottom view of Zdol, Ztetraol, and DDPA, where the endgroups are located on the surface. Both Zdol and Ztetraol [see Fig. 3(a) and (b)] exhibit clusters and network structures, and the endgroups of Zdol form less severe clusters, while DDPA lubricant film, which has the lowest endgroup functionality (−0.95 kcal/mol) between endgroups (Table II), does not display any cluster. In addition to the PFPEs on the diamond surface in Fig. 3, we also found that PFPEs on the other surfaces (i.e., DLC and graphene) form similar endgroup distributions as on the diamond surface.

From this result, we observed that the clusters formed in PFPE films depend on the interactions between endgroups (Ztetraol > Zdol ≫ DDPA) while the kind of carbon surfaces and their interactions to endgroup merely affect the forms of clusters by observing the similarity of endgroup distributions for various carbon surfaces.

TABLE VI
PARALLEL COMPONENT OF SELF-DIFFUSION COEFFICIENTS ($D_\parallel \times 10^5$) FOR ZDOL, ZTETRAOL, AND DDPA ON DIAMOND, DLC, AND GRAPHENE, RESPECTIVELY

Overcoat PFPE	Diamond	DLC	Graphene
Zdol	6.467	5.438	5.825
Ztetraol	6.706	3.636	1.984
DDPA	11.139	10.029	11.425

B. Mobility

As previously reported [13], the endgroup functionality dominantly controls the mobility of PFPE films, which is critical for the self-healing ability of lubricant on the depleted part of the disk [14]. Here, we quantified the mobility of PFPE lubricants by comparing the self-diffusion coefficient (D). The self-diffusion coefficient of a tagged molecule using Einstein's relationship is adopted to characterize the mobility of lubricant, and is decomposed to parallel and perpendicular components

$$D = \lim_{t\to\infty} \frac{1}{6t} \left\langle |\mathbf{r}(t) - \mathbf{r}(0)|^2 \right\rangle = \frac{1}{3}(D_x + D_y + D_z) = \frac{1}{3}(2D_\parallel + D_\perp). \quad (4)$$

Here, r is the position of the molecular center of mass; $D_\parallel$ and $D_\perp$ are the components of the diffusion coefficient parallel and perpendicular to the surface, respectively.

Tables VI and VII compare self-diffusion coefficients of each component for Zdol, Ztetraol, and DDPA on the diamond, DLC, and graphene. The comparison between $D_\parallel$ and $D_\perp$ values indicates that $D_\parallel$ is the dominant diffusion process since perpendicular diffusion is confined by the monolayer thickness of PFPE films. The $D_\parallel$ of PFPEs is on the reverse order of the interaction strength between endgroups (Ztetraol < Zdol < DDPA) compared to the cluster formation ability. Also, the self-diffusion is affected by the kind of surfaces examined. Zdol exhibits the similar mobility for all carbon surfaces, while Ztetraol shows minimal mobility, which is sensitive to the carbon surface. DDPA, containing different type of endgroup from Zdol and Ztetraol (hydroxyl endgroups) shows significantly higher self-diffusion coefficients on all carbon-overcoats. By also considering the molecular conformations of PFPEs, this result indicates that Ztetraol may not be the best choice for the carbon-overcoat beyond the conventional materials, since a significant disadvantage on the self-healing ability exists. Zdol especially shows better mobility than Ztetraol on the graphene while the quantitative value is similar on the DLC and diamond overcoats. The mobility of DDPA is slightly increased on the graphene.

Here, we found that the changes in the monolayer film conformation affected by the perpendicular profile of PFPE molecular structures on the surface are insensitive to the kind of the endgroups or carbon surfaces. However, we observed the endgroup distributions on the surface changes depend on the endgroup-endgroup interactions. Also, different chemical types of endgroups on PFPEs vary the mobility of PFPEs with respect to the

TABLE VII
PERPENDICULAR COMPONENT OF SELF-DIFFUSION COEFFICIENTS ($D_\perp \times 10^4$) FOR ZDOL, ZTETRAOL, AND DDPA ON DIAMOND, DLC, AND GRAPHENE, RESPECTIVELY

Overcoat PFPE	Diamond	DLC	Graphene
Zdol	0.6195	0.5321	0.6066
Ztetraol	0.4686	0.2440	0.3922
DDPA	0.9399	0.7867	0.7516

surface characteristics. Due to the advantages of the graphene including the single atomic thickness of graphene and superior mechanical and thermal characteristics, HDI with graphene will provide the significant reduction of HMS along with high reliability if we optimize the lubricant structures beyond DDPA.

IV. CONCLUSION

Physiochemical properties of various PFPE lubricant films including Zdol, Ztetraol, and DDPA on diamond, DLC, and graphene were investigated via large scale CGMD based on the coarse-graining procedures from atomistic level theory. PFPE molecular conformations were characterized by analyzing anisotropic radius of gyration, where perpendicular component determines thickness of monolayer lubricant film, and the distribution of functional endgroups as a function of PFPEs and carbon-overcoat structures.

From this study, we observed that the PFPE endgroup cluster formation on the surface and the mobility depend on the interactions between endgroups while the film thickness barely changes for the PFPEs with the same backbone structure even though the type of surface varies. Also, different chemical structures of endgroups on PFPEs significantly vary the lubricant mobility as a function of the surface characteristics. This study exhibits the rigorous comparisons of the combinatorial possibilities among PFPEs and carbon-overcoats, by presenting the multiscale solutions from the first principle to mesoscale. In order to achieve the advantages of the graphene in future HDI, we will further investigate the critical properties beyond the static and dynamic responses (e.g., surface morphology and rheological responses) with the wide range of combinations for the future HDI candidates. Our study will naturally lead to various novel HDI designs, which hybridize solid/liquid lubricants with different types of carbon overcoats (e.g., graphene/carbon nanotube or fullerene/PFPE) and nano blend of PFPEs by utilizing dimer interaction energies as listed in Table III.

ACKNOWLEDGMENT

This work was supported by Korea Science & Engineering Foundation through the WCU Project.

REFERENCES

[1] S. H. Vemuri, P. S. Chung, R. Smith, and M. S. Jhon, "Novel head-disk interface design in magnetic data storage," *J. Appl. Phys.*, vol. 111, April 2012, to be published.
[2] S. Izvekov and G. A. Voth, "A multiscale coarse-graining method for biomolecular systems," *J. Phys. Chem. B*, vol. 109, p. 2469, 2005.
[3] S. Izvekov and G. A. Voth, "Multiscale coarse-graining of liquid-state systems," *J. Phys. Chem. B*, vol. 123, p. 134105, 2005.
[4] R. Smith, P. S. Chung, J. A. Steckel, M. S. Jhon, and L. T. Biegler, "Force field parameter estimation of functional perfluoropolyether lubricants," *J. Appl. Phys.*, vol. 109, p. 7B728, 2011.
[5] R. Smith, P. S. Chung, S. H. Vemuri, and M. S. Jhon, "Atomistic simulation method in head-disk interface of magnetic data storage system," *J. Appl. Phys.*, vol. 111, April 2012, to be published.
[6] Q. Guo, S. Izumisawa, M. S. Jhon, and Y.-T. Hsia, "Transport properties of nanoscale lubricant films," *IEEE Trans. Magn.*, vol. 40, no. 4, p. 3177, Jul. 2004.
[7] Q. Guo, S. Izumisawa, D. M. Phillips, and M. S. Jhon, "Surface morphology and molecular conformation for ultrathin lubricant films with functional end groups," *J. Appl. Phys.*, vol. 93, p. 8707, 2003.
[8] M. S. Jhon, S. Izumisawa, Q. Guo, D. M. Phillips, and Y. T. Hsia, "Simulation of nanostructured lubricant films," *IEEE Trans. Magn.*, vol. 39, no. 2, p. 754, Mar. 2003.
[9] A. Agarwal, L. T. Biegler, and S. E. Zitney, "Simulation and optimization of pressure swing adsorption systems using reduced-order modeling," *Ind. Eng. Chem. Res.*, vol. 48, p. 2327, 2009.
[10] Y. Lang, S. E. Zitney, and L. T. Biegler, "Optimization of IGCC processes with reduced order CFD models," *Comput. Chem. Eng.*, vol. 35, p. 1705, 2011.
[11] K. Kremer and G. S. Grest, "Dynamics of entangled linear polymer melts—A molecular-dynamics simulation," *J. Chem. Phys.*, vol. 92, p. 5057, 1990.
[12] G. S. Grest, "Grafted polymer brushes in polymeric matrices," *J. Chem. Phys.*, vol. 105, p. 5532, 1996.
[13] Y.-T. Hsia, Q. Guo, S. Izumisawa, and M. S. Jhon, "The dynamic behavior of ultrathin lubricant films," *Microsyst. Technol.*, vol. 11, p. 881, 2005.
[14] T. M. O'Connor, Y. R. Back, M. S. Jhon, B. G. Min, D. Y. Yoon, and T. E. Karis, "Surface diffusion of chiral perfluoropolyalkylether films," *J. Appl. Phys.*, vol. 79, p. 5788, 1996.

Appendix B

Model Sensitivity Analysis of Single Phase in House LBM code

Abstract

Numerical simulation of turbulent flow is a challenging subject with a long history where there are many conceptual and numerical difficulties associated with analyzing various fluid flow characteristics occurring at high Reynolds number. Accurate turbulence modeling and flow simulations are extremely difficult numerical tasks and alternative flexible methodologies such as lattice Boltzmann method (LBM) are increasingly popular to describe experimental findings as well as offer advantages of algorithmic simplicity, transient nature, easiness in the treatment of complex geometrical boundaries and amenability to parallel computing platform. In this paper, we attempt to explore in developing an optimized LBM solver to examine the turbulent flow around bluff bodies using well known turbulence models including large eddy simulation with Smagorinsky sub-grid model and k-ε models and compare our simulation result with experimental data. To improve our numerical result, we introduce a cost function based on the means square difference between the simulation result and experimental data, and adapt control theory to the lattice Boltzmann equation and obtained the model sensitivity, which results into the optimized adjoint lattice Boltzmann equation. To verify our optimized LBM, we consider two scenarios: a simple Poiseuille flow, and a complex turbulence modeling. Our optimized model illustrated robust convergence behavior for both examples and was able to generate accurate relaxation parameter estimates efficiently.

1. Introduction

Lattice Boltzmann method (LBM) [1-7] is a promising alternative numerical scheme for simulating fluid flows containing complex physics phenomena. Unlike the conventional computational fluid dynamics (CFD) methods, LBM is based on mesoscopic kinetic equations, *i.e.*, by constructing simple kinetic models, the essential physics can be incorporated at the microscopic level and the averaged properties obey the desired macroscopic behaviors. The system is perturbed from hydrodynamic equilibrium in LBM and brought back to steady state via relaxation processes. Thereby it is easy to input the equilibrium properties as well as new physical rules descriptive for complex multi-physical systems [5]. The simplified version enables us to avoid solving nonlinear, integrodifferential kinetic equations (*e.g.*, Boltzmann transport equation (BTE)) in the study of mesoscale physics. Compared with standard CFD approaches, the LBM provides numerous advantages, including a clear physical picture, an inherently transient nature, easy implementation of complex boundary conditions and physical phenomena, novel treatment of turbulence as shown in this paper, and fully parallel algorithms.

The promising features of LBM lie on the easiness of programming, geometry handling, transient nature, parallelization, and incorporation of multi-phenomena and multi-physics. The use of regular lattices reduces the burden for generating grids, especially, for complex geometries. In order to maximize the advantages of LBM, automated grid generation and efficient treatment of solid boundaries are required prior to main solving process. The LBM further introduces more flexibility in the simulation by introducing multi-phenomena processes. In other words, we could take into account the different time scales for mass, momenta, and energy transfer in contrast to the single relaxation time model.

We use a single relaxation Bhatnagar-Gross-Krook (BGK) scheme based LBM for incorporating standard turbulence models and device an adjoint based sensitivity scheme to effectively incorporate multiple relaxation processes to

compare the simulation results with experimental data. The objective of utilizing an optimization scheme in LBM is to reduce the physical information within multiple relaxation processes with selected few optimized relaxation time parameters. In this work, we begin by incorporating two relaxation times via large eddy simulation model (LES) with popular Smagorinsky sub-grid model as well as the two-equation turbulence models, as they offer a good compromise between numerical effort and computational accuracy. In addition, for parameter estimation of the turbulence models from the experimental data from Bettis Atomic Power Laboratories, we use control theory to the case of a discrete model in order to get the adjoint lattice Boltzmann model. The layout of the paper is as follows: Section 2 deals with the introduction of the LBM numerical scheme, the turbulence model incorporation, and the sensitivity calculation approach and parameter estimation via adjoint method, respectively and Section 3 deals with the results obtained.

2 Standard Lattice Boltzmann Method

2.1 Boltzmann Transport Equation

LBM uses a mesoscopic representation of the fluid dynamics, which has the potential to simulate three dimensional (3D) transient flows in complex geometries at a more detailed level than conventional grid based CFD approaches. It is noted that LBM is by no means limited to discretization of the isotropic BGK equation that reproduces Navier Stokes equations (N-S) in the continuum hydrodynamic limit [1,2]. A number of other physical systems have been successfully examined via LBM formulations. Therefore, our finding can also advance the understanding of other physical systems. Below, we outline the main ingredients of the LBM approach.

It is well known in non-equilibrium statistical mechanics that fluid systems can be represented by kinetic equations on the "mesoscopic" level. On this level, fluid properties can be represented by a one particle distribution function defined in a phase space, $f = f(\mathbf{x}, \mathbf{v}, t)$, where $\mathbf{x}$ is the space coordinates and $\mathbf{v}$ is the velocity coordinates. Typical hydrodynamic variables such as mass,

momenta, and energy (temperature) are the first five moments of f, whose time derivative obeys the following integro-differential equation [8]:

$$\frac{\partial f(\mathbf{x},\mathbf{v},t)}{\partial t}+\mathbf{v}\cdot\frac{\partial}{\partial \mathbf{x}}f(\mathbf{x},\mathbf{v},t)=C\{f(\mathbf{x},\mathbf{v},t)\}. \tag{1}$$

Equation (2.1) is well-known kinetic equation. The terms on the left hand side of Eq. (1) are the streaming terms while the term on the right hand side is the collision term C, which acts to restore equilibrium within the system, representing interactions of particles at various positions and velocities. One of the simplest yet physically consistent forms for C is the BGK approximation, which is constructed according to the physically simplistic argument that no matter what the collision details are, the distribution function approaches a well-defined local equilibrium given by $f^{(eq)}(\mathbf{x}, \mathbf{v}, t)$, via collisions [9]:

$$C\{f(\mathbf{x},\mathbf{v},t)\}=-\frac{1}{\lambda}[f(\mathbf{x},\mathbf{v},t)-f^{(eq)}(\mathbf{x},\mathbf{v},t)], \tag{2}$$

where the parameter λ represents a characteristic relaxation time to equilibrium via molecular collisions. The details on this type of collision kernel are carefully examined, where the velocity space $\mathbf{v}$ can be discretized into a finite set of velocities $\{\mathbf{e}_i\}$ which preservs the conservation laws. We use the D3Q19 lattice when performing a 3D simulation. Figure 1 shows two lattices for 2D (D2Q9) and 3D LBM schemes.

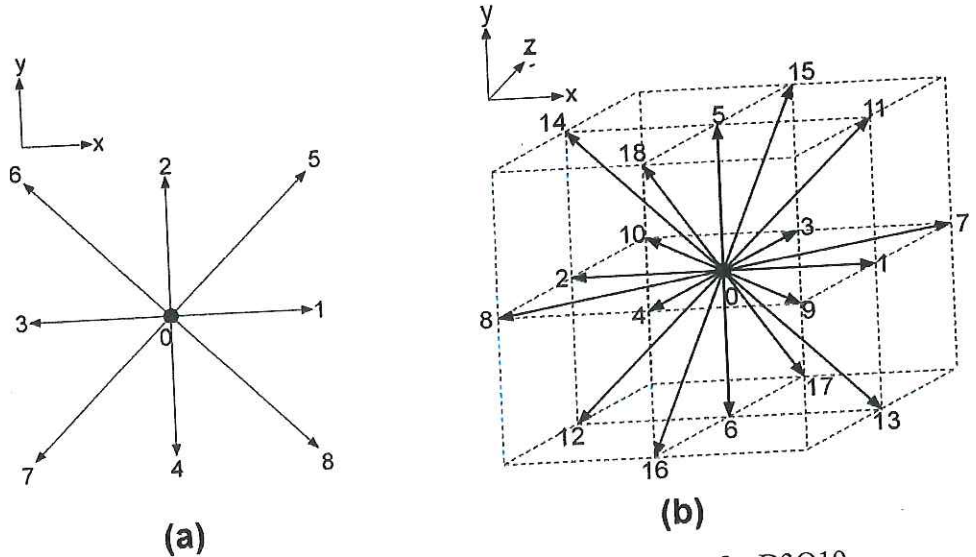

Fig. 1 (a) Lattices for D2Q9 and (b) lattices for D3Q19

From, Eqs. (1) & (2), we obtain

$$\frac{\partial f_i(\mathbf{x},t)}{\partial t} + \mathbf{e}_i \cdot \frac{\partial}{\partial \mathbf{x}} f_i(\mathbf{x},t) = -\frac{1}{\lambda}[f_i(\mathbf{x},t) - f_i^{(eq)}(\mathbf{x},t)]. \tag{3}$$

Taking the stream velocity as $\mathbf{e}_i = \delta\mathbf{x}/\delta t$ and applying upwind differencing, Eq. (3) becomes

$$f_i(\mathbf{x}+\mathbf{e}_i\delta t, t+\delta t) - f_i(\mathbf{x},t) = -\frac{\delta t}{\lambda}[f_i(\mathbf{x},t) - f_i^{(eq)}(\mathbf{x},t)] \tag{4a}$$

or

$$f_i(\mathbf{x}+\mathbf{e}_i\delta t, t+\delta t) - f_i(\mathbf{x},t) = -\frac{1}{\tau}[f_i(\mathbf{x},t) - f_i^{(eq)}(\mathbf{x},t)], \tag{4b}$$

where $\tau = \lambda/\delta t$. By performing Chapman-Enskog multiscale expansion to Eqs. (4) and choosing the equilibrium distribution forms properly, it can be shown that the LBM approaches to the asymptotically correct hydrodynamic and local thermo-hydrodynamic limits. Then, the parameter τ is given by

$$\tau = 0.5 + \nu/(c_s^2 \delta t), \tag{5}$$

where ν is the kinematic viscosity and c_s is the adiabatic speed of sound. Five moments derived from $f_i(\mathbf{x}, t)$ obey the continuum macroscopic limit, and are defined as:

$$\begin{aligned} \rho(\mathbf{x},t) &= \sum_i f_i(\mathbf{x},t), \\ \rho\mathbf{u}(\mathbf{x},t) &= \sum_i \mathbf{e}_i f_i(\mathbf{x},t), \text{ and} \\ \mathrm{DT}(\mathbf{x},t) &= \sum_i (\mathbf{e}_i - \mathbf{u})^2 f_i(\mathbf{x},t). \end{aligned} \tag{6}$$

Here, ρ, $\mathbf{u}$, and T are the fluid density, velocities, and temperature (energy), respectively and D is the dimension of the discretized velocity space. The following section will discuss in detail an examples of the popular turbulence modeling, using two equation & Smagorinsky large eddy simulation models.

2.2 Turbulence Flow Description

The LBM has shown excellent promise for direct simulation and modeling of highly compressible turbulent flows. Furthermore, the intrinsic space-time

locality of the LBM provides a considerable advantage in parallel computing. Thus, LBM can be further enhanced by incorporating various turbulence models available in literature. We briefly introduce and discuss these models and the methodology to integrate them into LBM.

(A) Two Equation Model (k-ε model)

Two equation models remain the most popular as they allow dynamical determination of two independent properties of unsolved turbulence which leads to the specification of characteristic velocity and turbulent length scales [10, 11]. Both the velocity and length scale are solved using separate transport equations (hence the term 'two-equation').

In two-equation models, the turbulence velocity scale is computed from the turbulent kinetic energy, which is provided from the solution of its transport equation. The turbulent length scale is estimated from two properties of the turbulence field, usually the turbulent kinetic energy and its dissipation rate. The dissipation rate of the turbulent kinetic energy is provided from the solution of its transport equation.

k is the turbulence kinetic energy and is defined as the variance of the fluctuations in velocity. It has dimensions of ($L^2\ T^{-2}$); for example, m^2/s^2. ε is the turbulence eddy dissipation (the rate at which the velocity fluctuations dissipate), and has dimensions of k per unit time ($L^2\ T^{-3}$); for example, m^2/s^3.

$$\rho\frac{Dk}{Dt}=\rho\frac{dk}{dt}+\rho u\cdot\nabla k=\frac{\partial}{\partial x_j}\left[\left(\frac{\mu_0}{\sigma_{k0}}+\frac{\mu_T}{\sigma_{kT}}\right)\frac{\partial k}{\partial x_j}\right]+\tau_{ij}S_{ij}-\rho\varepsilon \tag{7}$$

$$\rho\frac{D\varepsilon}{Dt}=\rho\frac{d\varepsilon}{dt}+\rho u\cdot\nabla\varepsilon=\frac{\partial}{\partial x_j}\left[\left(\frac{\mu_0}{\sigma_{\varepsilon 0}}+\frac{\mu_T}{\sigma_{\varepsilon T}}\right)\frac{\partial\varepsilon}{\partial x_j}\right]+C_{\varepsilon 1}\frac{\varepsilon}{k}\tau_{ij}S_{ij} \tag{8}$$
$$-\left[C_{\varepsilon 2}+f_{RNG}C_\mu\frac{\eta^3(1-\eta/\eta_0)}{1+\beta\eta^3}\right]\rho\frac{\varepsilon^2}{k}$$

Here, η is a dimensionless rate, $\eta=|S|k/\varepsilon$. The value of the closure coefficients are obtained empirically for specific flow situations. For the Standard model: C_μ=0.09, $C_{\varepsilon 1}$= 1.44, $C_{\varepsilon 2}$= 1.92, σ_{k0}= $\sigma_{\varepsilon 0}$= σ_{kT}=1.0, $\sigma_{\varepsilon T}$= 1.68, f_{RNG} =0.0, and finally η_0= 0.438, β= 0.012.

The turbulent kinematic viscosity is given by the relation:

$$\nu_t = C_\mu \frac{k^2}{\varepsilon}, \tag{9}$$

which is connected back to LBM as $\nu_t = \frac{1}{3}\tau_t c\delta x$, and

$$\nu_{total} = \nu_0 + \nu_t = \frac{2\tau_0 - 1}{6} c\delta x + \frac{1}{3}\tau_t c\delta x$$

values of k and ε come directly from the differential transport equations for the turbulence kinetic energy and turbulence dissipation rate.

(B) LES Turbulence Model

The simplest and most popular subgrid model is the standard Smagorinsky model [12], which employs a positive eddy viscosity for representing small scale energy damping. A simple approach for extending the LBM to include small scale dynamics for high Reynolds number flows is to combine it with the traditional subgrid model.

To apply the subgrid scale idea in the LBM framework, a filtered particle distribution, $\bar{f}_i$, is introduced via a spatial filter function, $G(\mathbf{x},\mathbf{x}')$,

$$\bar{f}_i(\mathbf{x}) \equiv \int G(\mathbf{x},\mathbf{x}') f_i(\mathbf{x}') d\mathbf{x}' \tag{10}$$

where, $\bar{f}_i$ satisfies the following modified kinetic equation,

$$\frac{\partial \bar{f}_i}{\partial t} + \mathbf{e}_i \cdot \nabla \bar{f}_i = \overline{\Omega}_i . \tag{11}$$

Discretizing Eq. (11) by the finite-difference scheme results in the same equation as the standard LBE for $\bar{f}_i$.

One possible approach is to apply the G-filter on the collision term or the equilibrium distribution function. Due to the nonlinearity of velocity in the equilibrium distribution function, several correlation terms are obtained. The closure problem is encountered like in the time-averaging approach. It may be argued that these correlation functions may be easier to model using physical arguments based on microscopic simplicity. The final results of modeling these

terms should be equivalent to the Reynolds stress at the macroscopic level. A more direct approach to generate a subgrid model is to link the collision steps with local information and abandon the single-relaxation time approximation. To do this, it is assumed that the filtered particle distribution will approach a local filtered equilibrium distribution, which can be chosen to be dependent only on mean local filtered quantities. Furthermore, it is assumed that the effect of the subgrid introduces an eddy viscosity only locally and allows the value of the relaxation time τ , to be locally adjusted so that the kinematic viscosity is equal to the sum of the molecular and the turbulent eddy viscosities.

It can be easily proved that neither the Chapman-Enskog expansion procedure nor the derivation of N-S equations is affected by the spatial dependence of τ if the filtered density and velocity are defined as $\bar{\rho} = \sum_i \bar{f}_i$ and $\overline{\rho u} = \sum_i e_i \bar{f}_i$, respectively. The filtered velocity $\bar{\mathbf{u}}$ defined in this way implies that the density fluctuation is small (proportional to the square of the Ma). Hence, quantities on the order u^3 (where $u = |\mathbf{u}|$) are neglected. The same form of continuity and momenta equations for the filtered quantities are derived, in which the total kinematic viscosity is related to the space-dependent relaxation time τ_{total}, with the similar functional form as given in Eq. (5),

$$\nu_{total} = \frac{2\tau_{total} - 1}{6} c\delta x . \tag{12}$$

The total kinematic viscosity ν_{total}, can be decomposed into the molecular kinematic viscosity ν_0, and the eddy kinematic viscosity ν_t, i.e.,

$$\nu_{total} = \nu_0 + \nu_t = \frac{2\tau_0 - 1}{6} c\delta x + \frac{1}{3}\tau_t c\delta x . \tag{13}$$

Here, τ_0 originates from the molecular relaxation and τ_t originates from the turbulent contribution. τ_{total} is sum of τ_0 and τ_t. The new additional term ν_t is called as turbulent kinematic viscosity resulting from the filtered scales. In the Smagorinsky model, ν_t is expressed as

$$\nu_t = (C_{Smagoinsky}\Delta)^2 |S| . \tag{14}$$

where $C_{Smagorinsky}$ and Δ are the Smagorinsky constant and the filter width, respectively. Δ usually depends on δx and $|S| = \sqrt{2\sum_{\alpha}\sum_{\beta} S_{\alpha\beta}S_{\alpha\beta}}$, which is the magnitude of the rate of strain tensor $S_{\alpha\beta} = (\partial u_{\alpha}/\partial x_{\beta} + \partial u_{\beta}/\partial x_{\alpha})/2$.

Thus, ν_t increases with $|S|$, so that ν_{total} becomes larger in regions close to obstacles.

In the LB scheme, the quantity $S_{\alpha\beta}$ can be computed locally, without taking extra derivatives, by formulating the non-equilibrium momentum flux tensor as

$$S_{\alpha\beta} = -\frac{3}{2\rho\tau_{total}\delta t}\sum_{i} e_{i\alpha}e_{i\beta}(f_i - f_i^{(eq)}) \equiv -\frac{3}{2\rho\tau_{total}\delta t}\Pi_{\alpha\beta}^{(1)}. \quad (15)$$

The quantity $\Pi_{\alpha\beta}^{(1)}$ is not explicitly dependent on τ_{total}. From this assumption, we can explicitly obtain τ_{total} as a function of Q (turbulence depending quantity). We first simplify ν_t from Eqs. (14) and (15) as

$$\nu_t = \frac{3}{\sqrt{2}\rho\tau_{total}\delta t}(C_{smagorinsky}\Delta)^2\sqrt{Q}. \quad (16)$$

with $Q = \sum_{\alpha,\beta}\Pi_{\alpha\beta}^{(1)}\Pi_{\alpha\beta}^{(1)}$. Later, recognizing

$$\tau_{total} = \frac{3\delta t}{(\delta x)^2}(\nu_0 + \nu_t) + \frac{1}{2}, \text{ and } \tau_0 = \frac{3\delta t}{\delta x^2}\nu_0 + \frac{1}{2}, \quad (17)$$

we obtain a quadratic equation in τ_{total}, the solution of which yields the local relaxation time ($\tau_{total} > 0$) as

$$\tau_{total} = \frac{1}{2}\left(\sqrt{\tau_0^2 + \frac{9}{(\delta x)^2}(C_{smagorinsky}\Delta)^2\frac{\sqrt{8Q}}{\rho}} + \tau_0\right)$$

(18)

The filter size Δ is usually set to one lattice spacing. The quantity $C_{Smagorinsky}$ is typically smaller than 0.5. $C_{Smagorinsky}$ tunes the effect of the subgrid model and should be adjusted empirically depending on the desired flow pattern. Note that $C_{Smagorinsky}$ may become space dependent, and that Q contains most of the turbulent flow information.

2.3 Boundary condition & Geometry Treatment

In our previous work [13], we adopted a novel non-reflecting boundary treatment method which is well-established in computational aero-acoustics [14,15] and direct numerical simulation to LBM for the first time. After updating the macroscopic variables using the nonreflecting boundary conditions, the unknown distribution functions were constructed. The component of a reflecting wave normal to the computational boundary significantly affects the numerical stability in contrast to the transverse one. Hence, we can implement the local equations in 1D normal coordinates for the non-reflecting boundary treatment.

Furthermore, the usual time consuming part of CFD simulation is the searching the hole points inside solids, especially, in the case of large scale problems with large number of grid points and facets which compose a solid object. Instead of testing all the points in computational domain, our LBM code can minimize the number of testee points which need to be tested whether it is inside solids or not by employing a point inclusion test algorithm. To narrow down the area encompassing the testee points, we utilize the methodologies generally used in overset (or overlapped/chimera) grid systems, i.e., zones of interference and hole-map algorithms. Finally, the testee points are sorted to the hole (which are the points inside solids and thus excluded in problem solving process) and fluid points by utilizing a sophisticated point inclusion test algorithm [16, 17]. We illustrate the effectiveness of the algorithm by recording the cpu time for testing the hole or fluid points in various geometries including a complex helical a torsion with parameter (3, 12/3) (Fig. 2)

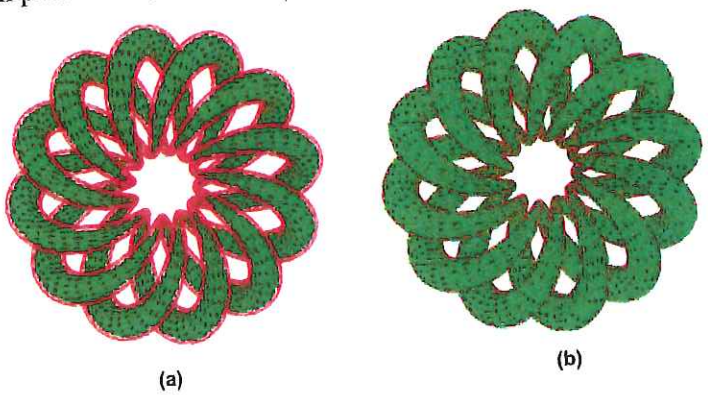

Fig. 2: Pure hole points (top) and hole points including solid points for boundary condition (bottom) inside a torsional geometry

2.4. Parameter estimation in Optimized LBM Using Adjoint sensitivity analysis

In this section we are interested in identifying some parameters of the lattice Boltzmann scheme, for instance the turbulence model closure parameters by comparing the predictions of the direct model to those derived from some other technique (analytic or numerical solution to the Navier–Stokes equations or from experiments). So, we will use inverse modeling to estimate these parameters. This will be done using the adjoint method, which is directly derived from the optimal control theory [18].

We consider the following cost-function J(k), which deals with a vision of the error at the final time :

$$J(\lambda)=\sum_{i=1}^{Nx}\sum_{j=1}^{Ny}\left|u\left(\lambda,x_{i,j},N\right)-u\left(x_{i,j},N\right)^{2}\right|,$$

$N=N\delta t$ is the time when the steady state is reached and $\lambda=[C_{\mu}, C_{\varepsilon 1}, C_{\varepsilon 2}, \sigma_{k0}, \sigma_{\varepsilon 0}, \sigma_{kT}, \sigma_{\varepsilon T}, \eta_0, \beta, C_{Smagorinsky}]^T$. So for the first case of the pressure driven flow, it is obvious that the exact solution is stationary (i.e., u(xi,j,k) = u(xi,j)). Now the assimilation process consists in minimizing the cost-function J. We use a gradient method:

$\lambda^{n+1}=\lambda^{n}+\omega\nabla_{\lambda}J^{n}(\lambda)$. So we need to estimate the gradient of the cost-function $\nabla_{\lambda}J$ by the following equation:

$$\nabla_{\lambda}J=-\sum_{k=0}^{N-1}P^{k+1}\frac{df}{d\lambda},$$

Where where P^k are a set of dual parameters, which are naturally line vectors and f is the particle distribution function obtained from LBM. The parameters $[P^k]^T$ belong to the solution space of the LBM scheme and are determined by the following backward lattice Boltzmann equation called adjoint lattice Boltzmann equation (ALBE):

$$2\cdot P^{N}=-\frac{\partial J}{\partial f},$$

$$2\cdot P^{k+1}=2\cdot P^{k}+\frac{\partial J}{\partial f}, \text{ for k=N-1,N-2,....,1.}$$

Our first simple case consists in identifying a single parameter, i.e., the relaxation time τ. So the unknown parameter k is equal to τ. The computation of $J(\tau)$ requires one integration of the direct model and one integration of the adjoint model. Thus, we may try and apply a descent method in order to find the solution to the minimization problem. In this methodology, we use the analytical form of Poiseuille flow velocity given as: $\mathbf{U} = \frac{L\Delta p}{2\nu} y\left(1 - \frac{y}{L}\right)$ and change the relaxation time parameter to obtain similar profile with LBM simulation (Fig. 3). Fig. 4 shows the convergence of algorithm to the optimal parameter τ. Fig. 5 illustrates the comparison between the velocity profiles between the analytical expression, standard LBM with arbitrary relaxation time, and optimized LBM with $\tau = 0.2$ and the optimal one $\tau = 0.8$, respectively.

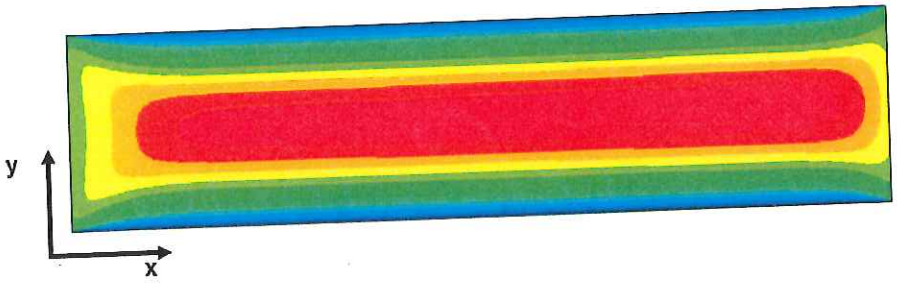

Fig. 3 Velocity contours of pressure driven flow using LBM

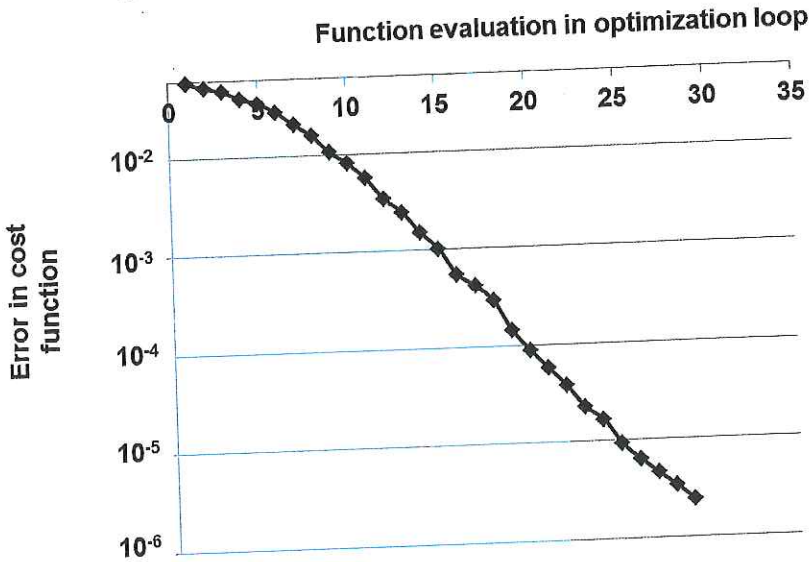

Fig. 4: Log of $J(\tau)$ the vs. iteration n, where the optimal parameter value of 0.8 is obtained

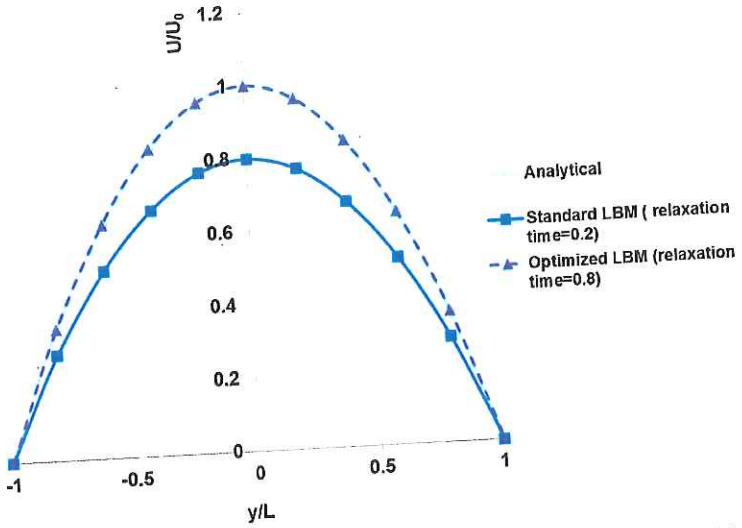

Fig. 5: Comparison of the velocity profiles between analytical, standard LBM with arbitrary relaxation time=0.2, and optimized LBM with relaxation time=0.8

4. Turbulent flow simulation and experimental verification

Experimental methodology

The experimental velocity values were provided from the Bettis Atomic Power Laboratory via Laser Doppler velocimetry (LDV), which is the technique of using the Doppler shift in a laser beam to measure the velocity in transparent or semi-transparent fluid flows. Here, LDV crosses two beams of collimated, monochromatic, and coherent laser light in the flow of the fluid being measured. The reflected light fluctuates in intensity, the frequency of which is equivalent to the Doppler shift between the incident and scattered light, and is thus proportional to the component of particle velocity which lies in the plane of two laser beams. The wind tunnel system that was used in the experiment is given in Fig. 6 below. A collection of bluff body geometries (square, rounded, and chaffed cornered cylinders) were tested and the x, y, and z velocity components were obtained.

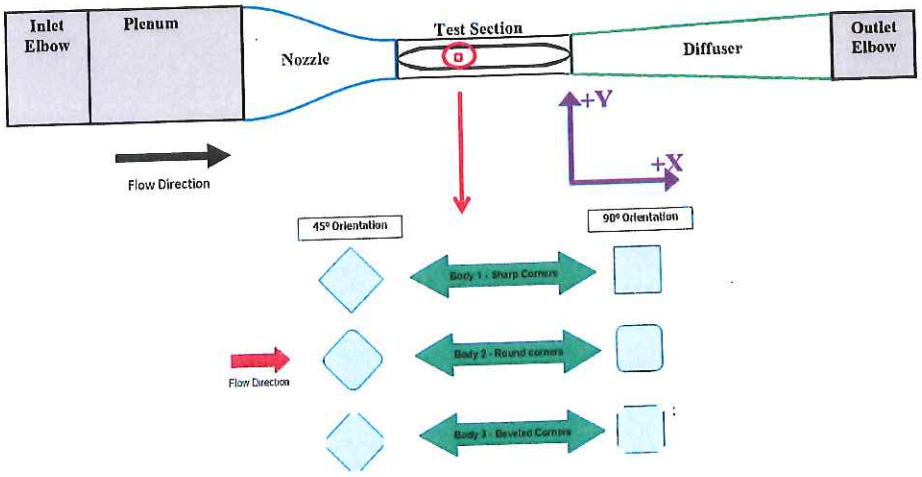

Fig. 6: Experimental setup of various bluff bodies oriented in two directions to the flow

As an example, fig. 7 shows the experimental x-velocity component profile of a square cornered cylinder. As the experimental velocity profiles are given individually, as component-wise, we simulated a 2-D system and estimated the turbulence parameter based on the x-component.

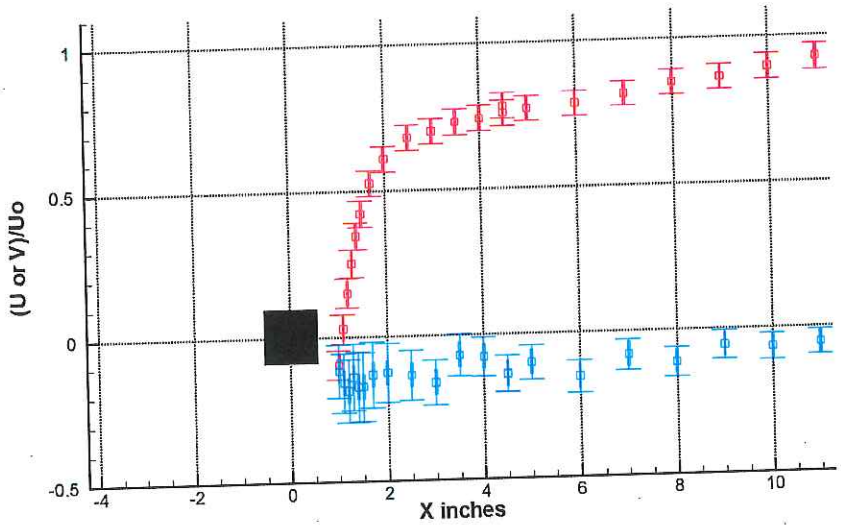

Fig. 7: Experimental velocity component values of flow around a square cylinder (red denotes x-component values, blue denotes y-component values)

We now simulate the is the flow over a bluff bodies 1 & 3 at Re=250 000, in this case a square and chaffed cornered cylinders with various orientations to

the incoming flow for which experimental measurements are made available by Bettis Atomic Power Laboratory. The geometry of the flow, including the overall domain size, is given in Fig. 8. The conditions other than the inflow are as follows: Slip condition at the lateral boundaries, zero gradient boundary condition at the downstream boundary, no-slip boundary condition at the cylinder surface.

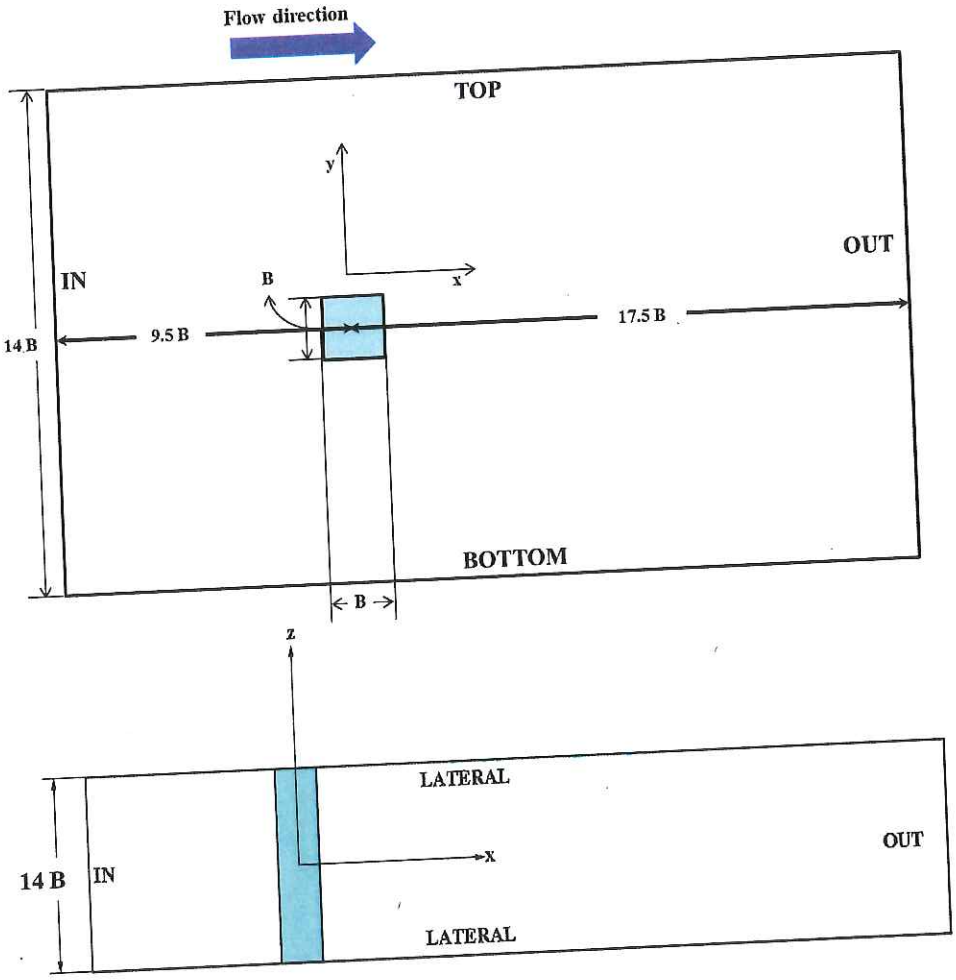

Fig. 8 The geometry of the flow around square cylinder showing the geometric dimensions. Shaded region represents the cylinder.

Fig. 9 shows the flow streamlines with two-equation and Smagorinsky subgrid models for each case with square cylinders oriented perpendicular and 45° to the flow. However, for the purpose of parameter estimation, we calculate the sensitivities and estimate the parameters of only the Smagorinsky case with the

square cylinder aligned perpendicular to the flow (Fig. 6(a)). Please refer Appendix A for the input code (source code is included in Appendix B).

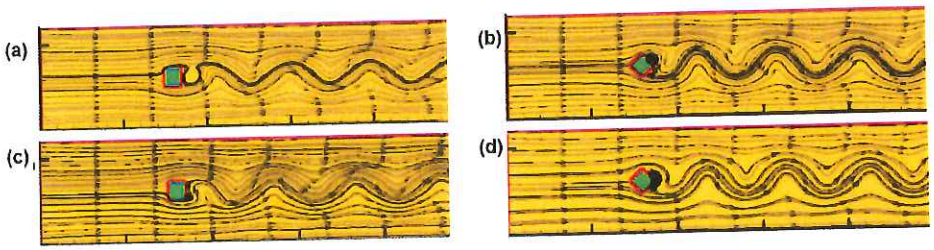

Fig. 9 Flow streamlines around a square cylinder and 45° rotated cylinder predicted by (a) & (b) LES model, (c) & (d) two equation model

In this case, the unknown parameter is the Smagorinsky constant ($C \equiv C_{Smagorinsky}$), and the computation of J(C) requires one integration of the direct model and one integration of the adjoint model. We apply the trust-region based approach for obtaining a descent direction for the descent method in order to find the solution to the minimization problem. Fig. 10 illustrates the result of the convergence of algorithm to the optimal parameter by showing the decrease in the mean square error between the simulation result and the experimental data; we begin with C=0.1 and end up with an optimal value of C=0.34. Figs. 11 & 12 show the final result agrees very well with the experimental data for the optimal value for both square and chaffed cornered cylinders (the Smagorinsky constant reached the same final value in both bluff bodies due to the similarities in the flow pattern).

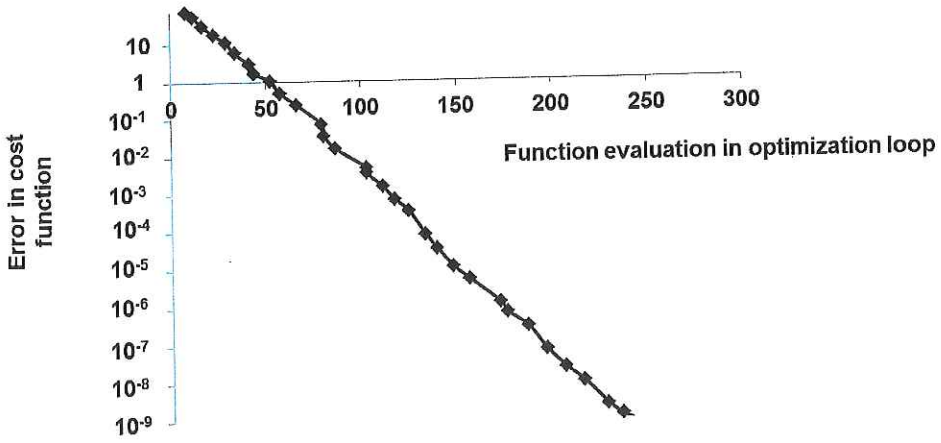

Fig. 10: Log of the cost-function J(C) vs. iteration, where the optimal value of C is obtained as 0.34.

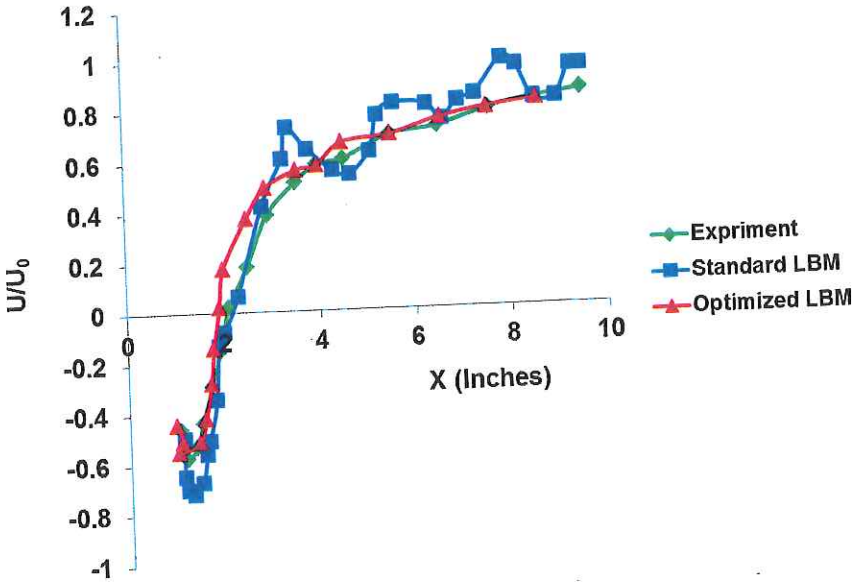

Fig. 11: Comparison of the x-component velocity profiles between experimental data and result obtained from LBM simulation using optimized parameter

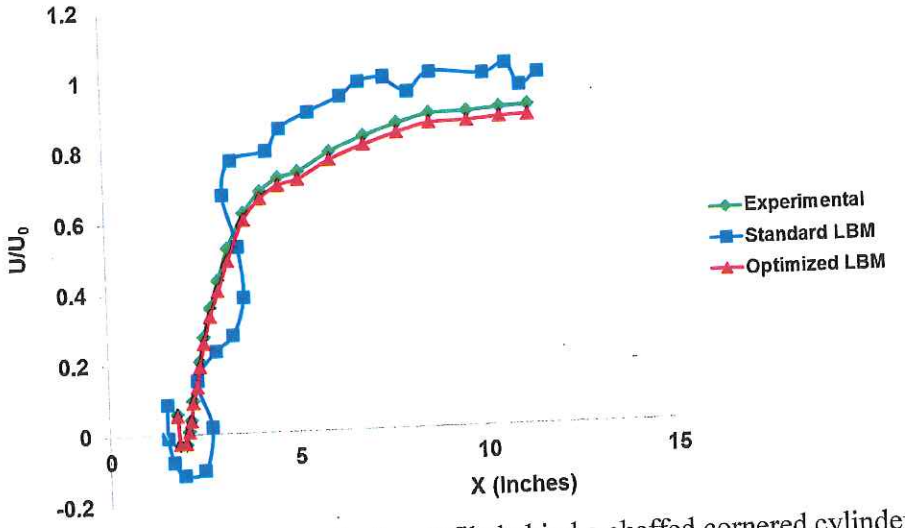

Fig.12: X-component velocity profile behind a chaffed cornered cylinder (bluff body 3) comparison between experimental, standard LBM and optimized LBM.

5. Conclusions

In this work, we developed standard turbulent models including the RANS model with Smargorinsky large eddy simulation (LES) model which are employed into standard LBM to examine fluid flow at high Reynolds number. Although standard LBM describes flow patterns qualitatively, we introduce

optimized LBM methodology using adjoint sensitivity analysis to find improved turbulence modeling. The optimized LBM provides accurate flow results which agree very well with experimental data. We demonstrated the parameter estimation method using simplest Poissuelle flow by comparing the analytical velocity profile and obtaining optimal relaxation time parameter from an arbitrary value to exactly fit the LBM result. We then simulated turbulent flow around a pair of bluff bodies (square and chaffed cornered cylinders) and obtained optimized sub-grid model parameter which lead to very good agreement of the velocity profile with experimental data. The optimization will help us to understand numerous relaxation processes that go on in turbulence and other multi-physical phenomena. The ultimate aim in coupling optimization with LBM is to reduce the number of relaxation time parameters into an optimal set which can still predict all the essential phenomena in the system via a Kolrauchy expression. Furthermore, via sensitivity analysis, we can asses the robustness of each relaxation model, and can lead to deeper insight into the use of LBM.

1. S. Chen, H. Chen, D. Martinez, and W. Matthaeus, "Lattice Boltzmann model for simulation of magnetohydrodynamics," *Phys. Rev. Lett.*, **67**(27), 3776 (1991).
2. S. Chen and G.D. Doolen, "Lattice Boltzmann method for fluid flows," *Ann. Rev. Fluid Mech.*, **30**, 329 (1998).
3. T. Kataoka and M. Tsutahara, "Lattice Boltzmann model for the compressible Navier-Stokes equations with flexible specific-heat ratio," *Phys. Rev. E,* **69**(3), Part 2, AR 035701 (2004).
4. S. Hou and Q. Zou, "Simulation of cavity flow by the lattice Boltzmann method," *J. Comput. Phys.*, **118**, 329 (1995).
5. X. He, S. Chen, G. D. Doolen, "A Novel Thermal Model for the Lattice Boltzmann Method in Incompressible Limit," *Ann. Rev. Fluid Mech.*, **146**, 282 (1998).
6. X. He and G. D. Doolen "Lattice Boltzmann method on curvilinear coordinates system: flow around a circular cylinder" *J. Comput. Phys.*, **134**, 306 (1997).

7. H. Chen, S. Kandasamy, S. Orszag, R. Shock, S. Succi, V. Yakhot, "Extended Boltzmann kinetic equation for turbulent flows," *Science*, **301**, 633 (2003)
8. R. Liboff, *Kinetic theory: Classical, quantum, and relativistic descriptions*, 2nd edition, John Wiley & Sons, New York, NY (1998).
9. P. L. Bhatnagar, E. P. Gross, and M. Krook, "A model for collision processes in gases. I. Small amplitude processes in charged and neutral one-component system," *Phys. Rev. A,* **94**, 511 (1954).
10. SE Elghobashi, TW Abou-Arab, "A two-equation turbulence model for two-phase flows," *Phys. Fluids*, **26**, 931 (1983)
11. D.A. Wilcox, "Simulation of transition with a two-equation turbulence model," *AIAA*, **32**, 247 (1994)
12. J. Smagorinsky, "General circulation experiments with the primitive equations I. The basic experiment," Mon. Weather Rev., **91**, 99 (1963).
13. D. Kim, H.M. Kim, M.S. Jhon, S.J. Vinay III, J. Buchanan, "Characteristic non-reflecting Boundary treatment in lattice Boltzmann method," Chin. Phys. Lett., **25**, 1964 (2008).
14. K.W. Thompson, *J. Comput. Phys.*, **68,** 1 (1987).
15. K.W. Thompson, *J. Comput. Phys.*, **89**, 439 (1990).
16. F. Feito, J. C. Torres, A. Urena, "Orientation, simplicity, and inclusion test for
planar polygons," *Comput. Graphics,* **19** 595 (1995).
17. F. Feito, J. C. Torres, "Inclusion test for general polyhedral", *Comput. Graphics*
21 23-30 (1997).
18. M.M. Tekitek , M. Bouzidi , F. Dubois , P. Lallemand, "Adjoint lattice Boltzmann equation for parameter identification", *Comput. Fluids* **35** 805 (2006).